# Large Scale Structure: Dynamics and Statistics

Yuyu Wang

Submitted to the graduate degree program in Department of People who read Abstracts and the Graduate Faculty of the University of Kansas in partial fulfillment of the requirements for the degree of Doctor of Philosophy.

Hume Feldman, Chairperson

Barbara Anthony-Twarog

Committee members

Mikhail Medvedev

Sergei Shandarin

Suzanne Shontz

Date defended: May 29, 2020

The Dissertation Committee for Yuyu Wang certifies
that this is the approved version of the following dissertation :

Large Scale Structure: Dynamics and Statistics

Hume Feldman, Chairperson

Date approved: June 08, 2020

# Abstract

The peculiar velocity of galaxies and galaxy clusters is the only dynamical probe of gravity on cosmic scales, which makes it a crucial tool in studying gravitational instability, mass distributions and density fluctuations on large scales.

In this dissertation, I present the work we did in estimating the cosmic peculiar velocity field. We introduce a new method of estimating peculiar velocities from kinetic Sunyaev-Zel'dovich (kSZ) effect using deep learning neural networks to simplify the complicated calculation steps in the conventional method. We explore the feasibility of applying the formalism to future kSZ observations by testing it with multiple noise models using numerical simulations designed for these purposes.

We further discuss an analysis of the two-point peculiar velocity correlation function using data from both observations and simulations. We find a non-Gaussian distribution of the cosmic variance of the correlation function, which makes the peculiar velocity correlation function less than ideal as a probe of large-scale structure.

To solve this problem, we develop an improved method for calculating the parallel and perpendicular velocity correlation functions directly from peculiar velocity surveys using maximum-likelihood estimators. The central feature of this method is the use of a position-dependent weighting scheme in order to reduce the contribution of nearby galaxies, which are typically overrepresented relative to more distant galaxies that occupy the volume of most surveys. We demonstrate that the correlation function calculated in this way is less susceptible to bias due to our particular location in the Universe and provides a better approximation of a Gaussian distribution errors than other velocity correlation functions. In addition, the position weighted parallel velocity correlation function provides stabler and tighter cosmological parameter constraints than other methods.

# Acknowledgements

I would like to express my deepest gratitude to my adviser Dr. Hume Feldman, who gives me advice, encouragement and motivation from the first day of my graduate study. Dr. Feldman is not only the mentor of my graduate study and this dissertation, but also a pioneer who inspires me to grow to a researcher and physicist. His passion for intellectual pursuit will always be my inspiration.

I would also like to thank my dissertation committee: Dr. Barbara Anthony-Twarog, Dr. Mikhail Medvedev, Dr. Sergei Shandarin, and Dr. Suzanne Shontz for the supervision and guidance that has been important for the materialization of this dissertation.

I very much appreciate my collaborators Dr. Richard Watkins, Abhinav Kumar, and Christopher Rooney, from whom I got many helps and learned a lot.

I would like to appreciate the help from the friendly faculty and staff at the Department of Physics and Astronomy, especially Dr. Jennifer Delgado, Dr. Gregory Rudnick, Dr. Kyoungchul Kong, Alan Feltz, Kim Hubbel, Kristin Rennells, Joel Sauerwein, and Kayla Wegley, whose readiness to help students cannot be overestimated.

My graduate student life in the University of Kansas was enjoyable due to many wonderful friends. I had the best office mates Nesar Ramachandra and Keita Todoroki, who make the office full of intellectual discussion about research and humorous conversation about life. I met my good friends Safa Alhussainalali and Rachel Crist, who shared moments of frustration, laughter and excitement with me. I also want to thank my amazing roommates Ning Liu, who provides me helps since the first day I arrived the University of Kansas.

Thank you Mum and Dad, for the unconditional love you give through my life. None of this would have been possible without your encouragements and supports. I miss you Grandma, I hope you could see this. I can not grow up to achieve this without you. I miss you so much!

# Contents

# List of Figures

# List of Tables

# Chapter 1

# Background: Peculiar Velocity

In the early 20 century, physicist (Leavitt, 1908; Leavitt & Pickering, 1912; Hubble, 1929) discovered the expansion of the universe: $V = H_0 r$, where $V$ is the Doppler-shift measured velocity of galaxies, $H_0$ is the Hubble constant and $r$ is the radial distance. Due to the difficulties in measuring distances, results of early studies (see, Burstein, 1990) indicated that the Universe expansion was smooth and homogeneous. Gamow (1946) first questioned if there are deviations from a smooth expansion. Rubin (1951) first explored this question suggesting a possible rotation of the Universe. Later, many studies explored the problem with large-scale motions of galaxies. Corey & Wilkinson (1976) and Smoot et al. (1977) confirmed the existence of a dipole anisotropy in the cosmic microwave background (CMB), which implies a large-scale motion of the Local Group, which is the galaxy group of the Milky Way and our nearest neighboring galaxies. The motion of galaxies and galaxy clusters caused by gravity is called peculiar velocity in cosmology.

The existence of galaxies, clusters and other structures formed by gravitational instability, indicates that our Universe is not perfectly homogeneous. Rather, the Universe had small density fluctuations at early times that grew into the structures we observed today by gravitational instability. The relation between the velocity field and the density field $\mathbf{v} = \frac{H_0 f}{4\pi} \int d^3\mathbf{r}' \frac{\mathbf{r}'-\mathbf{r}}{|\mathbf{r}'-\mathbf{r}|^3} \delta(\mathbf{r}')$ (Peebles, 1980), where $f$ is the growth rate of structure, $\delta$ indicates the density field, $\mathbf{r}$ and $\mathbf{r}'$ are the radial distances of the velocity and density fields, makes the peculiar velocity a good tracer of density fluctuations and gravitational instability. A direct test of gravitational instability comes from the comparison of peculiar velocity and redshift surveys (e.g. Watkins et al., 2009; Feldman et al., 2010; Davis et al., 2011; Nusser et al., 2011; Macaulay et al., 2011; Turnbull et al., 2012; Macaulay et al., 2012; Nusser, 2014; Springob et al., 2014a; Johnson et al., 2014; Scrimgeour et al., 2016a). Furthermore, the peculiar velocity field can be used to constrain cosmological model parameters, such as the matter density ($\Omega_m$) and the growth rate ($f$) (e.g. Borgani et al., 2000; Wang et al., 2018; Adams & Blake, 2020).

Today, we know that the peculiar velocity causes deviations from the Hubble Flow, which makes the redshift we observe a linear combination of the peculiar velocity and the Hubble Flow:

$$cz = H_0 r + v, \tag{1.1}$$

where $c$ is the speed of light, $z$ is the redshift, and $v$ is the peculiar velocity. For better accuracy, the redshift $z$ can be replaced by $z_{mod}$ by including the cosmic acceleration: $z_{mod} = z[1 + 0.5(1 - q_0)z - (1/6)(1 - q_0 - 3q_0^2 + 1)z^2]$, where $q_0$ is the deceleration parameter (Springob et al., 2014a; Davis & Scrimgeour, 2014; Watkins & Feldman, 2015a). Equation 1.1 shows that the estimate of peculiar velocities relies on the measurements of redshift and distance. The redshift can be accurately measured by the Doppler effect of the light spectrum. Theoretically, the distance can be determined by the luminosity of galaxies with the inverse-square law. However, the luminosity of galaxies cannot be measured directly, which makes the distance measurement more challenging than the redshift.

Many methods have been introduced to determine the luminosity of galaxies, such as Tully-Fisher (TF) relation (Tully & Fisher, 1977), Faber-Jackson (FJ) relation (Faber & Jackson, 1976), Fundamental Plane (FP, Djorgovski & Davis, 1987; Dressler et al., 1987b), Surface Brightness Fluctuation (SBF, Tonry & Schneider, 1988), and Type Ia supernova distances (Rest et al., 2014). TF describes the relation between the luminosity and the rotation velocity of spiral galaxies. FJ illustrates the relation between the luminosity and the velocity dispersion of elliptical galaxies. FP expresses the relation between the effective radius, surface brightness and velocity dispersion of elliptical galaxies. SBF measures the variance in the light distribution of galaxies arising from fluctuations in the numbers and luminosities of individual stars per resolution element. The type Ia supernova is a category of supernovas that have consistent luminosity peaks, which can be used as standard candles whose luminosities are known.

The luminosity is then being used to calculate the distance modulus. The distance modulus describes the distance in logarithmic scale ($\mu = 5log_{10}(\frac{r}{10\text{pc}})$), which will cause a non-Gaussian error distribution of the distance and therefore in the peculiar velocity. This non-Gaussian problem can be addressed by using the unbiased estimator $v = czlog(\frac{cz}{H_0 r})$ introduced by Watkins & Feldman (2015a), since its velocity is proportional to the logarithm of distances.

In current peculiar velocity surveys, the distance uncertainty is about 20% (e.g. Masters et al., 2006; Springob et al., 2007; Tully et al., 2013, 2016), which leads to a low signal-to-noise ratio for the peculiar velocity estimates. Due to the large peculiar velocity error, statistical studies of velocity ensembles are necessary. The most widely used statistical approaches for studying the peculiar velocity field are bulk flow, velocity correlation function, and pairwise velocity statistic.

The bulk flow is the lowest order statistic of the velocity field and is generally thought of as the weighted average of peculiar velocities in a volume. Rubin et al. (1976a,b) first detected a bulk flow of the Local Group relative to the volume defined by a sample of 96 galaxies. Later, the research of bulk flows has been further refined by many studies (e.g. Schechter, 1980; Tonry & Davis, 1981; Dressler et al., 1987a; Lauer & Postman, 1994). Bulk flows are typically calculated by two methods. The first is the maximum likelihood estimate (MLE) method (e.g. Kaiser, 1988; Watkins & Feldman, 2007). The MLE formalism estimates the bulk flow as a weighted average of sample velocities, with the weight calculated to minimize its overall uncertainty given the position, velocity and error distributions in the catalogue. A modern formulation is the minimum variance (MV) method (Watkins et al., 2009; Feldman et al., 2010; Agarwal et al., 2012b; Scrimgeour et al., 2016a). The MV formalism minimizes the differences between the actual observational data and an “ideal" survey that may be designed to probe a volume in a particular way.

The velocity correlation function is a two-point correlation function of velocity fields. The most widely used velocity correlation estimator was introduced by Gorski (1988) and further developed in Gorski et al. (1989). The velocity correlation function can be expressed as two independent functions, one for velocity components along the separation vector of pairs of galaxies and one for components perpendicular to the vector. The Gorski (1988) correlation estimator is a combination of these two functions, with the precise mixture given by selection functions that depend on the distribution of survey objects as well as the separation distance. The velocity correlation function has revealed interesting results in constraining cosmological parameters (e.g. Jaffe & Kaiser, 1995; Zaroubi et al., 1997; Juszkiewicz et al., 2000; Borgani et al., 2000; Abate & Erdoğdu, 2009; Nusser & Davis, 2011; Okumura et al., 2014; Howlett et al., 2017; Hellwing et al., 2017; Wang et al., 2018; Dupuy et al., 2019).

The pairwise velocity is the mean value of the peculiar velocity difference of galaxy pairs at separation **r**, which is introduced by Peebles (1980). Juszkiewicz et al. (1999) derived approximate solution of the pair conservation equation relating the pairwise velocity to the matter density and two-point correlation functions of mass density fluctuations, which is used in many studies (e.g. Ferreira et al., 1999; Juszkiewicz et al., 2000; Feldman et al., 2003; Hellwing, 2014; Hellwing et al., 2014). Studies show that the pairwise velocity can also be used to investigate the kinetic Sunyaev-Zel'dovich effect (Zhang et al., 2008; Hand et al., 2012; Planck Collaboration et al., 2016a).

The error in distance measurement grows with redshift, which will propagate to the velocity and make the velocity signal-to-noise ratio worse at high redshift. Thus, current peculiar velocity surveys are shallow ($z < 0.05$). In contrast, the kinetic Sunyaev-Zel'dovich effect provides a distance and redshift independent approach for measuring peculiar velocities, which could increase the depth of peculiar velocity surveys significantly.

The Sunyaev-Zel'dolvich (SZ) effect (Sunyaev & Zeldovich, 1970, 1972, 1980) describes the CMB distortion caused by the inverse Compton scattering of CMB photons off electrons in galaxy clusters. The SZ effect has two contributions: the thermal (tSZ) and the kinetic Sunyaev-Zel'dolvich (kSZ) effects. The tSZ effect is caused by random motions of hot electrons in the intra-cluster medium, while the kSZ effect is caused by the bulk motion of galaxy clusters. Therefore, the kSZ effect can be used to estimate peculiar velocities of galaxy clusters. Haehnelt & Tegmark (1996) first discussed the feasibility of estimating peculiar velocities of clusters from CMB observations. Holzapfel et al. (1997) estimated peculiar velocities of two distant galaxy clusters through milimeter-wavelength observations of SZ effect. Later, many studies estimated peculiar velocities and bulk flows through kSZ effect on large scales (e.g. Kashlinsky & Atrio-Barandela, 2000; Benson et al., 2003; Kashlinsky et al., 2008; Zhang et al., 2008; Planck Collaboration et al., 2014b; Soergel et al., 2017; Sayers et al., 2019). However, the kSZ signal is very weak, which causes limitation on the accuracy of peculiar velocity estimations. With improvements in the kSZ measurements (e.g. Mittal et al., 2018), the peculiar velocity estimation from kSZ effect for individual clusters may become feasible in the near future.

In this dissertation, I present and discuss the work we have done by studying the peculiar velocity field. In chapter 2, I present the work we did in estimating peculiar velocities from kSZ effect using deep learning neural networks, and discuss the feasibility and advantages of applying the deep learning algorithms to the kSZ velocity estimate with both simulations and observations. In chapter 3, I discuss the peculiar velocity correlation function with new findings of its non-Gaussian cosmic variance distribution. In chapter 4, I present our work improving the method for estimating peculiar velocity correlation functions by implementing a position-dependent weighting scheme to reduce the effect caused the non-Gaussian cosmic variance.

# Chapter 2

# Analysis of Peculiar Velocity Estimate from Kinematic SZ Effect using Deep Neural Networks

The Sunyaev-Zel'dolvich (SZ) effect is expected to be instrumental in measuring distant velocities of galaxy clusters in future surveys. We simplify the conventional calculations of peculiar velocities of galaxy clusters using a deep learning model. Using one of the largest Cosmological hydrodynamical simulations, the image of distorted photon backgrounds are generated for idealized observations. We explore the feasibility of applying the deep learning neural network to extract peculiar velocities from future kSZ observations with multiple noise models. We combining kinetic and thermal SZ effects in the neural network architectures to understand the effect of the optical depth and extending the pipeline to include redshift-dependence. This chapter is from the project collaborated with Nesar S. Ramachandra, Edgar M. Salazar, Hume A. Feldman, Richard Watkins and Klaus Dolag. It is under preparation for submission.

## 2.1 Introduction

The Sunyaev-Zel'dolvich (SZ) effect (Sunyaev & Zeldovich, 1970, 1972, 1980) describes the process of Cosmic Microwave Background (CMB) distortion caused by the inverse Compton scattering of the CMB photons off by the electrons in galaxy clusters. The SZ effect has two contributions: the thermal (tSZ) and the kinetic Sunyaev-Zel'dolvich (kSZ) effect. The tSZ effect is caused by the random motion of hot electrons in the intra-cluster medium, while the kSZ effect is caused by the bulk motion of galaxy clusters. Therefore, the kSZ effect can be used in estimating peculiar velocities of galaxy clusters (e.g. Rephaeli & Lahav, 1991; Bhattacharya & Kosowsky, 2008;

Kashlinsky et al., 2009; Zhang et al., 2008; Atrio-Barandela et al., 2012; Planck Collaboration et al., 2014c; Sayers et al., 2016; Planck Collaboration et al., 2018a; Soergel et al., 2017; Hurier, 2017; Kirillov & Savelova, 2019). However, the weak signal of the kSZ effect makes its detection very difficult. Hand et al. (2012) first detected the kSZ effect from CMB maps with the Atacama Cosmology Telescope (ACT) through pairwise momentum estimator. Using similar methods, several groups have detected the kSZ effect in both real and Fourier spaces (e.g. Planck Collaboration et al., 2016b; Soergel et al., 2016; Sugiyama et al., 2018; Calafut et al., 2017; Li et al., 2018). In addition, some studies detected the kSZ effect by cross-correlating kSZ temperature map with density or velocity field (e.g. Schaan et al., 2016; Hill et al., 2016). Planck Collaboration et al. (2018b) detected the kSZ effect through measurements of the CMB temperature dispersion. Furthermore, Mittal et al. (2018) discussed the ability of measuring the kSZ effect for individual clusters in the upcoming multi-frequency surveys. With the improvements in the kSZ measurement, the estimate of peculiar velocities from kSZ effects for individual clusters becomes possible.

The peculiar velocity field is a powerful tracer of density fluctuations, which is generally studied through ensemble statistics such as bulk flows, velocity correlation functions, and the pairwise velocity statistic (e.g. Borgani et al., 2000; Watkins et al., 2009; Kumar et al., 2015; Wang et al., 2018). The pairwise velocity statistic is the mean value of the peculiar velocity difference of galaxy pairs at separation $\mathbf{r}$ and is a widely used approach to study the large-scale velocity field (e.g. Ferreira et al., 1999; Feldman et al., 2003; Zhang et al., 2008; Hand et al., 2012; Planck Collaboration et al., 2016a). Estimating peculiar velocities using kSZ effect requires information about optical depth, which describes the integration of electron densities. However, the measurement of optical depth has errors and bias that may affect peculiar velocity estimates. Lindner et al. (2015) has a average uncertainty of the cluster optical depth around 31% and Mittal et al. (2018) forecasts a average uncertainty about 24% in observations. In addition, using emission-weighted temperature instead of the density-weighted temperature, which is not observable, in the optical depth measurement may cause a systematic bias of the optical depth (Diaferio et al., 2005; Dolag & Sunyaev, 2013). In simulations, the optical depth varies between models with and without star-formation and feedback (Flender et al., 2016, 2017). The weak kSZ signal and errors of optical depth make the kSZ peculiar velocity calculation imprecise and difficult. Machine learning algorithms may provide a simpler and more accurate method for estimating kSZ peculiar velocities.

Machine learning algorithms are designed without explicit programming of the physical phenomena, instead they perform complex analyses in a data-driven manner. Some of the machine learning methods including Gaussian processes, decision trees, nearest neighbor algorithms and support vector machines have been used in astrophysical context. On the other hand, utilization of deep learning (DL) methods, specifically the Convolutional Neural Networks (CNNs), is rapidly increasing due to the availability of data, advancements of computational architectures (such as the Graphic Processors, Tensor Processors and dedicated accelerators), and the development of libraries (such as TensorFlow, Keras, Torch).

However, the model interpretability and explainability of DL methods remains to be an area of active research since they are generally characterized as 'black box' inference techniques. However, complex deep learning neural networks trained on sufficiently large amount of data capture information much more efficiently than traditional machine learning techniques (shown in various comparison studies, e.g., Metcalf et al. (2019) in strong lensing detection problem).

Learning the intrinsic characteristics of the dataset may be accomplished unsupervised where training is unaccompanied by correct responses, for instance in Generative models (Ravanbakhsh et al. (2016), Morningstar et al. (2018), He et al. (2019)). Alternatively, a supervised learning routine involves providing the correct mapping during training. Supervised techniques for object identification have been applied to a broad variety of astrophysical problems including strong lensing image classification (Petrillo et al. (2017)) and parameter estimation (Levasseur et al. (2017), Hezaveh et al. (2017), Morningstar et al. (2018)), which have demonstrated improvements on predictive precision and inference speed compared to traditional inference techniques.

Machine learning applications in Cosmological analyses frequently deal with using simulated data instead of real astronomical data. This is in part due to the dearth of large quantity of data. On the other hand, calibrating the forward model parameters is not robust enough to generate unbiased training data.

In this chapter, we use simulation data to test the feasibility of extracting peculiar velocities from kSZ effect by deep learning architectures. In section 2.2, we describe the relation between the SZ effect and the peculiar velocity. In section 2.3, we introduce the simulation we used for generating training and validation data. In section 2.4, we display the CNN structure of the deep learning model. In section 2.5, we explain the training methods and results of the model. In section 2.6, we display the error analysis for the model. In section 2.7, we examine the model predictions through the pairwise velocity statistic. In section 2.8, we discuss the feasibility of the model using various noise templates. In section 2.9, we conclude this chapter.

## 2.2 Sunyaev-Zel'dovich Effect

The relation between radial motions of galaxy clusters and the observed radiation temperature was first introduced by Sunyaev & Zeldovich (1980) with the Equation 2.1, where $\tau = \int \sigma_T N_e dl$ is the optical depth with respect to Thomson Scattering. $\sigma_T$ is the Thomson Scattering cross-section and $N_e$ is the electron density.

$$v = -\frac{c}{\tau}\frac{\Delta T_{kSZ}}{T_{CMB}}, \tag{2.1}$$

On the other hand, the tSZ effect (Sunyaev & Zeldovich, 1970) is usually expressed by the Compton y parameter:

$$\frac{\triangle T_{tSZ}}{T_{CMB}} = yf(x), \quad y = \int \frac{k_B T_e}{m_e c^2}\sigma_T N_e dl, \tag{2.2}$$

where $f(x) = xcoth(x/2) - 4$ and $x$ is the dimensionless frequency given by $x = h\nu/(k_B T_{CMB})$.

Since the kSZ signal is independent of the redshift and has a strong suppression on the secondary CMB anisotropy, the kSZ effect can be available up to the era of reionization. However, due to the weakness of the signal and the error in optical depth measurement, the peculiar velocity estimation from kSZ effect is still very challenging in real observations.

Alternatively, the potential of utilizing numerical simulations for estimating peculiar velocity from kSZ effect are being studied extensively. For instance, Soergel et al. (2017) has shown promising results with obtaining pairwise velocity statistics with kSZ effect by applying map filtering to the signals and used tSZ signal to estimate average optical depth.

For both the observation and the simulation, the requirement of optical depth is inevitable when using the conventional method to kSZ peculiar velocity. In addition, the estimation of optical depth in simulation is various between models with and without star-formation and feedback. The measurement of optical depth for single cluster in observation is even harder. Therefore, a new method that can predict peculiar velocity from the kSZ effect without optical depth would reduce the difficulty in calculating kSZ peculiar velocity significantly. The deep learning algorithms provide a possible approach to achieve it. A training data set from a numerical simulation with a realistic SZ map-making pipeline may empower a deep learning model to simplify the computation in the estimation of peculiar velocities by avoiding the signal integral, map filtering and optical depth estimates.

## 2.3 Simulation and Training Data

The Deep Neural Networks typically require a large amount of training data in order to optimize a large amount of weights. Therefore, a big enough cosmological simulation that can provide large number of galaxy cluster samples is necessary. In addition, the simulation data must resemble idealized observations from telescopes, which leads to a lightcone pipeline to generate kSZ and tSZ images.

In this paper, we use the Magneticum Simulations[1] to generate kSZ and tSZ cluster images. The Magneticum simulations are a set of cosmological hydrodynamical simulations with a large range of scales and resolutions. The Magneticum Simulations are generated by an extended version of the N-body/SPH GADGET3 code (Springel et al., 2001; Springel, 2005; Beck et al., 2016) with WMAP7 (Larson et al., 2011) cosmological parameters from Komatsu et al. (2011). The dark matter only (DM-only) simulation includes dark matter and dark energy which provide gravity information, while the hydrodynamical simulation uses the hydrodynamic equations to include the

---

[1] http://www.magneticum.org

Table 2.1: The cosmological parameters of the Magneticum Simulation Box0 and parameters of training data sets

| | |
|---|---|
| Matter density, $\Omega_m$ | 0.272 |
| Cosmological constant density, $\Omega_\Lambda$ | 0.728 |
| Baryon density, $\Omega_b$ | 0.046 |
| Hubble parameter, $h$ ($100kms^{-1}Mpc^{-1}$) | 0.704 |
| Amplitude of matter density fluctuations, $\sigma_8$ | 0.809 |
| Primordial scalar spectral index, $n_s$ | 0.963 |
| Box size ($h^{-1}$Mpc) | 2688 |
| Number of particles | $2 \times 4536^3$ |
| Mass of dark matter particles, $m_{dm}$ ($10^9 h^{-1} M_\odot$) | 13 |
| Mass of gas particles, $m_{gas}$ ($10^9 h^{-1} M_\odot$) | 2.6 |
| Softening of particles, $f_p$ ($h^{-1}kpc$) | 10 |
| Softening of stars, $f_s$ ($h^{-1}kpc$) | 5 |
| Redshift of slice 1 | [1.04,1.32] |
| Redshift of slice 2 | [1.32, 1.59] |
| Redshift of slice 3 | [1.59, 1.84] |
| Redshift of slice 4 | [1.84, 2.15] |
| Mass of galaxy clusters | $> 10^{13} M_\odot$ |
| kSZ maps of each slice | $10,000$ |
| tSZ maps of each slice | $10,000$ |
| Size of maps | $2R_{vir}$ |

baryonic component, which can be described as an ideal fluid. With the baryonic particles and temperature information, the SZ signal can be detected by tracking back along the line of sight.

In this chapter, we use the largest box, Box0, in the Magneticum Simulation suite. Table 2.1 shows the cosmological parameters of the simulation box and the parameters of our data sets. We take four redshift slices from the simulation that cover redshift in a range of [1.04, 2.15]. From those four redshift slices, we generated 40000 kSZ and 40000 tSZ images (10000 images for each redshift slice) through SMAC (Dolag et al., 2005), which is a map making utility for idealized observations. The size of a cluster image is set to be two times of its virial radius. To reduce the calculation expense, we use the redshift of each slice instead of the redshift of each cluster in calculating the virial radius, which means the size of the cluster images is not perfectly normalized to the virial radius. According to our test, the difference is tiny and its effect on the final results is negligible.

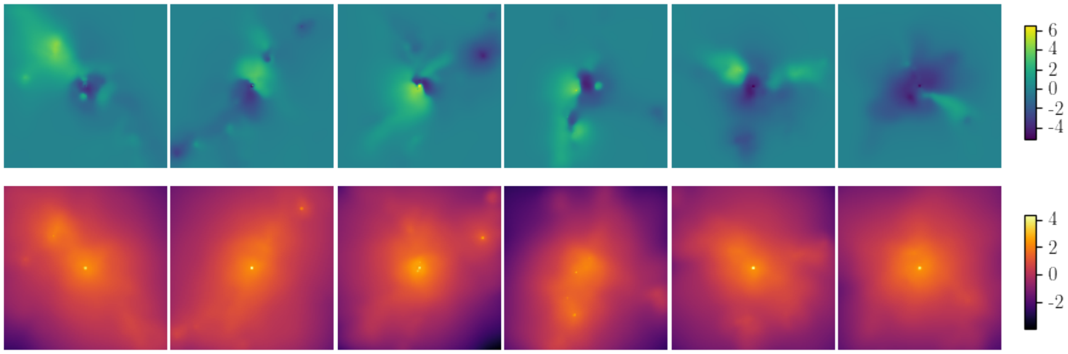

Figure 2.1: kSZ images (upper panel) and tSZ images (lower panel) of six clusters. The unit of the kSZ images is $sinh^{-1}(\Delta T_{kSZ}/T_{CMB} \times 10^6)$, and the unit of the tSZ image is $log_{10}(y \times 10^6)$.

Figure 2.1 shows the kSZ and tSZ examples of six clusters generated from the Magneticum Simulation. We train the neural network with 80% of the kSZ & tSZ images, which are similarly to the examples shown in figure, and use the remaining 20% as validation data for testing.

## 2.4 The Learning Model

An end-to-end deep learning algorithm is implemented here to predict the peculiar velocity from kSZ effect. Convolutional Neural Networks (CNNs) are an obvious choice for such image-based regression analyses due to the following reasons: First, the amount of generated data (40000 kSZ images) can be efficiently utilized in deep learning neural networks which consist of a large number of trainable model parameters called weights. It can be seen that with respect to the scaling of accuracy with the size of the data set, deep learning neural networks outperform most existing machine learning models. Secondly, despite having characteristic features in the SZ image (as seen in Figure 2.1), the modeling is complex and the feature-mapping to peculiar velocity is not straightforward due to the optical depth. This makes feature-agnostic training algorithms like CNNs is more desirable than feature-specified learning methods for modeling SZ images. The CNNs can extract high and low level features from a series of convolutional filters, which are used to train the peculiar velocity prediction model.

While there are numerous advanced deep learning neural network architectures in literature and

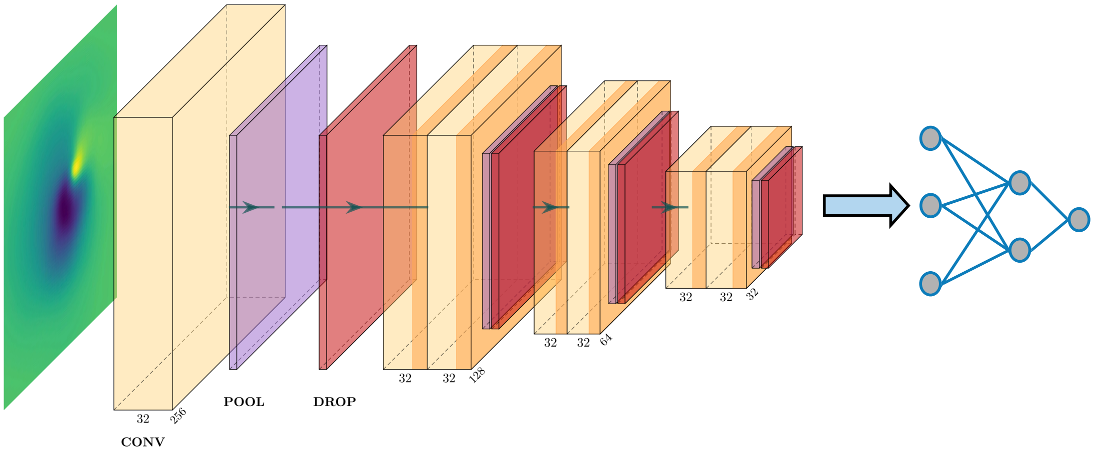

Figure 2.2: Schematic Convolutional Neural Network architecture for regression including kSZ effect only. The real architecture used in this analyses is multiple blocks of convolutional, pooling and dropout layers repeated before feeding the dense layers.

under active research, our goal is not to achieve the best accuracy. Instead, we would simply like to demonstrate the feasibility of using deep learning neural networks to estimate peculiar velocities using the direct input of kSZ images and highlight the advantage of such simulation-based training approaches over traditional calculation techniques on the kSZ peculiar velocity estimation.

Figure 2.2 shows our CNN architecture with only kSZ images as input data. It follows a Conventional Deep Neural Network architecture like the CIFAR-10 (LeCun et al. 2015), with layers stacked sequentially. The kSZ image, the input data, will be addressed through several layer blocks (includes convolutional, pooling and dropout layers) and multiple dense layers to get peculiar velocity as the output. Short descriptions of each layer are as follows: 1. Convolutional layers consist of numbers of image kernels that extract morphological features of images. While

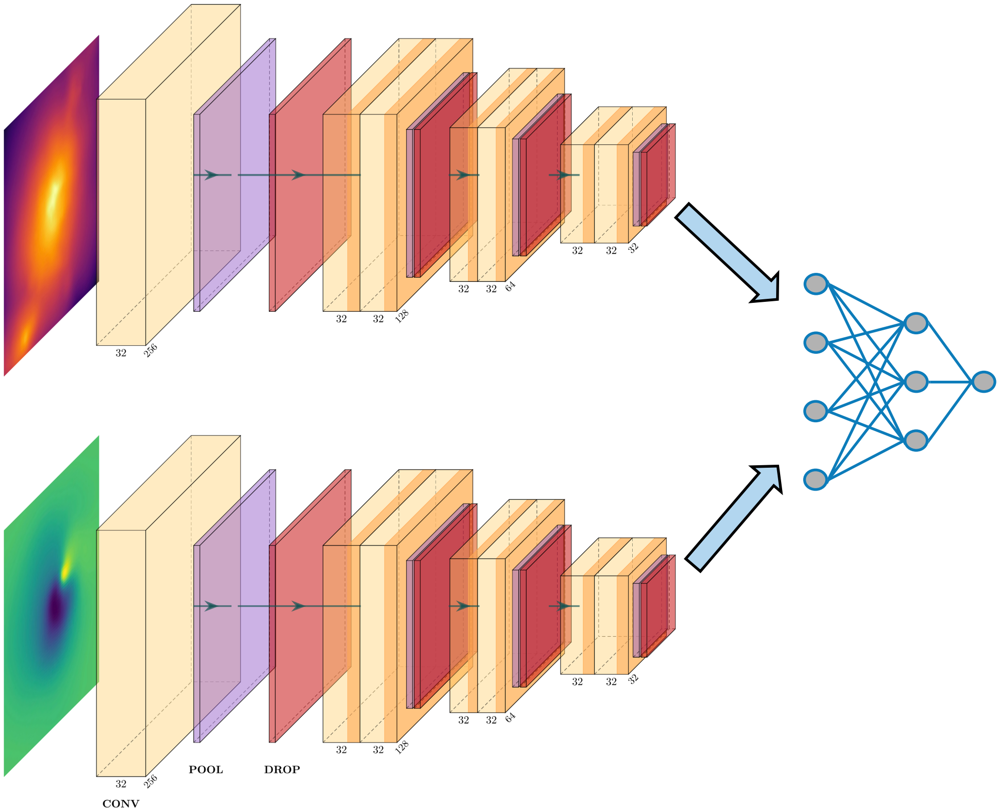

Figure 2.3: Schematic Convolutional Neural Network architecture for regression including both kSZ and tSZ effect. The real architecture used in this analyses is multiple blocks of convolutional, pooling and dropout layers repeated before feeding the dense layers.

the high-level features are extracted at the initial layer, a more abstract featured map (2D matrix that contains the image information) is obtained after. 2. The pooling layer operates on each map independently, and progressively reduces the spatial size of the map to reduce the amount of computations in the network. 3. Dropout layers re-initialize a sub-set of neurons of the network at every epoch of the training, which reduces the chances of over-training. 4. The flattening layer converts the map from 2-D matrix to a single 1-D vector. 5. Dense layers change the dimension of the flattened 1-D vector to peculiar velocity scatter corresponding to the input image.

Overall, the repeated convolutional layer blocks extract abstract featured maps from the images, which are then used as inputs in the dense layers toward to the end of the network. As opposed to the image classification, this regression pipeline has a linear activation to get point estimation of the peculiar velocity. In addition, the loss function is defined by the mean square error (MSE) value $L = (v - v_p)^2$, where $v$ is the true peculiar velocity and $v_p$ is the predicted peculiar velocity from deep learning model. By providing enough correct data to learn from, the model would be trained to project the input kSZ images to the output peculiar velocities.

The model of including both kSZ and tSZ images has similar architecture with an independent repeated convolutional structure, shown in figure 2.3. The only difference in the combined SZ image analysis is that the kSZ and tSZ are computed in separate branches. After the flattening layer, the outputs from those two branches are concatenated to a 1-D vector, which is then fed into a dense layer block for predicting the peculiar velocity.

### 2.4.1 Uncertainty Quantification

One of the shortcomings of a traditional regression analysis with CNNs is that it lacks proper treatment for the uncertainty quantification. Methods like Bayesian Neural Network frameworks using Markov Chain Monte Carlo (MCMC) or Variational Inference (VI) techniques have been explored for solving this problem. However, most of these methods are challenging due to convergence, diagnosis or computational expenses.

Alternatively, Monte Carlo (MC) Dropout method (see Gal & Ghahramani (2015) for a detailed review) enables utilizing existing trained deep learning models in interpreting prediction uncertainty. While the dropout layer is generally used to avoid over-fitting in the training phase, using it in the testing phase can be a highly useful uncertainty quantification. It also shown by Gal & Ghahramani (2015) that the MC dropout is a Bayesian approximation of Neural Networks to Gaussian processes, where the error modeling is formally defined.

The implementation involves an ensemble of neural networks (of ensemble size $N_{tot}$) that only differ from each other by a fraction (prescribed by the dropout rate $d$) of trained neurons that are dropped out. We use our base architectures shown in Figures 2.2 and 2.3 with dropout rate $d = 0.5$ and form an ensemble of $N_{tot} = 100$ test-phase networks. We find the prediction uncertainty reduces with the dropout rate. We use a large dropout rate ($d = 0.5$) in this chapter to test out model with more challenges.

The validation image $I$ is forward propagated through each of the network, providing individual point-predictions $v_p^i(I)$, where $i = 0, ..., N_{tot}$. The mean and standard deviation of the prediction for each image is calculated by $< v_p >= \frac{1}{N_{tot}} \sum_i^{N_{tot}} v_p^i(I)$ and $\sigma_v = \frac{1}{N_{tot}} \sum_i^{N_{tot}} [v_p^i(I) - < v_p >]^2$.

Hence, the MC dropout is a simple prediction uncertainty quantification tool, without any additional expensive computation tasks while training, unlike the Bayesian Neural Networks that explicitly define distributions in predictions Kendall & Gal (2017). In addition to providing uncertainty estimations, such ensemble methods can also monitor failure modes, i.e., the choice of network architecture and training schemes can be compared in terms for robustness of the results.

## 2.5 Training

We build two models respective to the two CNN architectures in section 2.4: Model I, kSZ only model shown in Figure 2.2; Model II, the combined kSZ and tSZ model shown in Figure 2.3. For training strategy, we check the universality of the model in different redshifts by training the models with data of single redshift slices and with data of multiple redshift slices (all the four redshift slices).

For Model I, we first train the model with kSZ images of each redshift slice, which means we

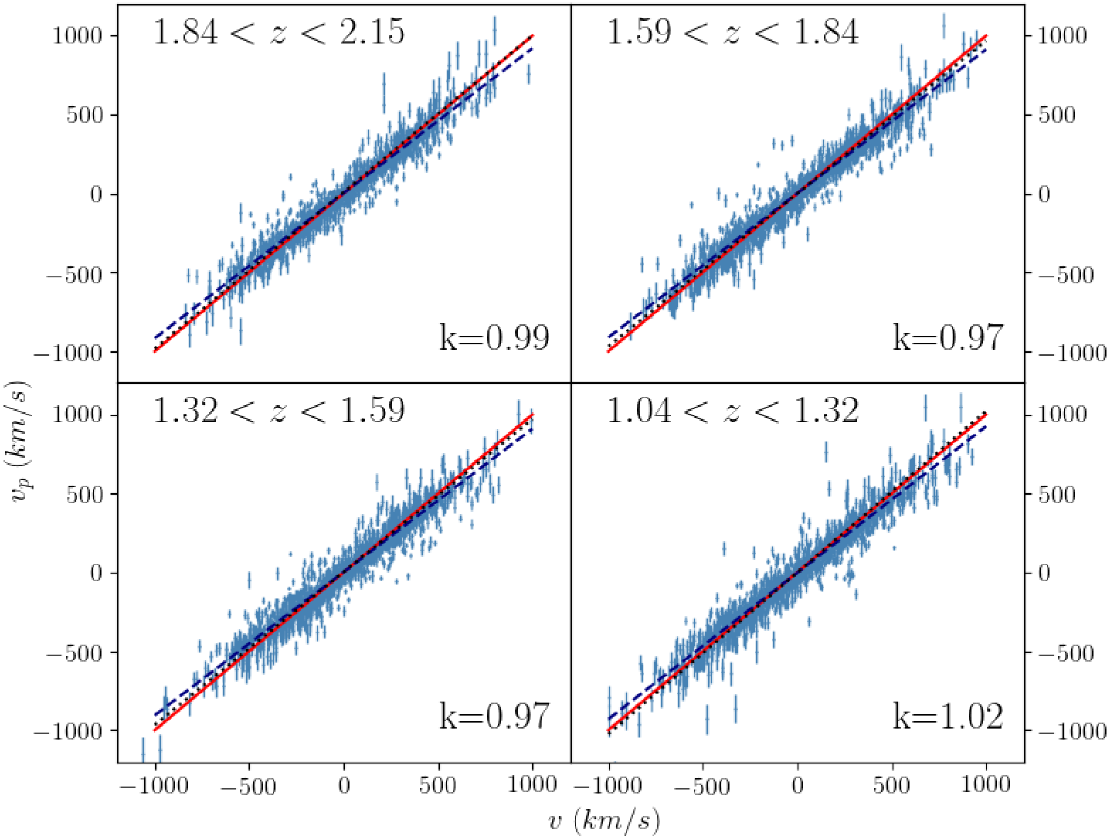

Figure 2.4: The results of the Model I trained by kSZ images of each redshift slice. The x-axis shows the true peculiar velocity and the y-axis indicate the predicted peculiar velocity. The red solid line shows the 1:1 ideal relation between the true and predicted velocities, the navy dashed line shows the regular linear fitting of the scatters, and the black dotted line shows the uncertainty weighted linear fitting of the scatters. The error bar shows the uncertainty of the predicted velocity using the MC Dropout method.

train the model four times independently and each time use the 80% of the 10000 kSZ images of a single redshift slice; secondly, we train the model with the data of multiple redshift slices, which means the training data is the 80% of the whole 40000 kSZ images.

Model II is trained with both kSZ and tSZ images. Due to the scaling relation between $\tau$ and $y$ (Battaglia, 2016), adding tSZ images into training may improve network predictions by including information of optical depth.

Figure 2.4 shows the prediction results of Model I trained by kSZ images of single redshift slices. In the figure, we show two linear fittings of the scatter: regular (uniform-weighted) fitting and uncertainty weighted fitting, where the weight equals to $1/\sigma_v$. Though the regular fitting (navy dashed line) is biased from the 1:1 ideal expectation (red solid line), the uncertainty weighted fitting result (black dotted line) agrees with the ideal expectation well. In the figure, k value shows the slope of the uncertainty weighted fitting. Although trained by data from different redshift slices, the prediction results of those four training sets have very similar fitting slopes, which means the model for predicting peculiar velocity from kSZ images is fairly stable with different redshift. This is consistent with eq. 2.1 that the kSZ effect is independent of the redshift. In addition, the similarity of contours (tested but not shown in the figure) of the scatters of different redshfit slices proves the redshift independence.

Figure 2.5 shows the results of the Model I trained by the kSZ images from multiple redshift slices, which covers a larger redshift region. Comparing with figure 2.4, figure 2.5 has larger scatters due to more validation data. However, the fitting slope is similar as figure 2.4. Though the model trained by full data (from all four redshift slices) may have larger errors, it covers a larger region which makes the model more universal and flexible for applications.

In both figure 2.4 and 2.5, the predictions ($v_p$) using kSZ images show good agreements with the true velocities ($v$). However, the difference from the regular fitting line to the expectation shows that some predictions of the model have inevitable bias from the expectation. Since the Model I does not include information of optical depth, we add tSZ information into the training to explore a possible improvement (Model II).

The prediction results of Model II trained by both kSZ and tSZ images of single and multiple redshift slices show negligible difference from the results of Model I. Figure 2.6 shows the results of Model II using data of multiple redshift slices. Similar as Model I, the results of Model II are redshift independence. However, the fitting slope and the scatters are not improved by adding tSZ information into consideration. The similar performances between Model I and Model II might mean that the deep learning neural network could estimate the peculiar velocity well enough with only kSZ input, which simplifies the calculation significantly.

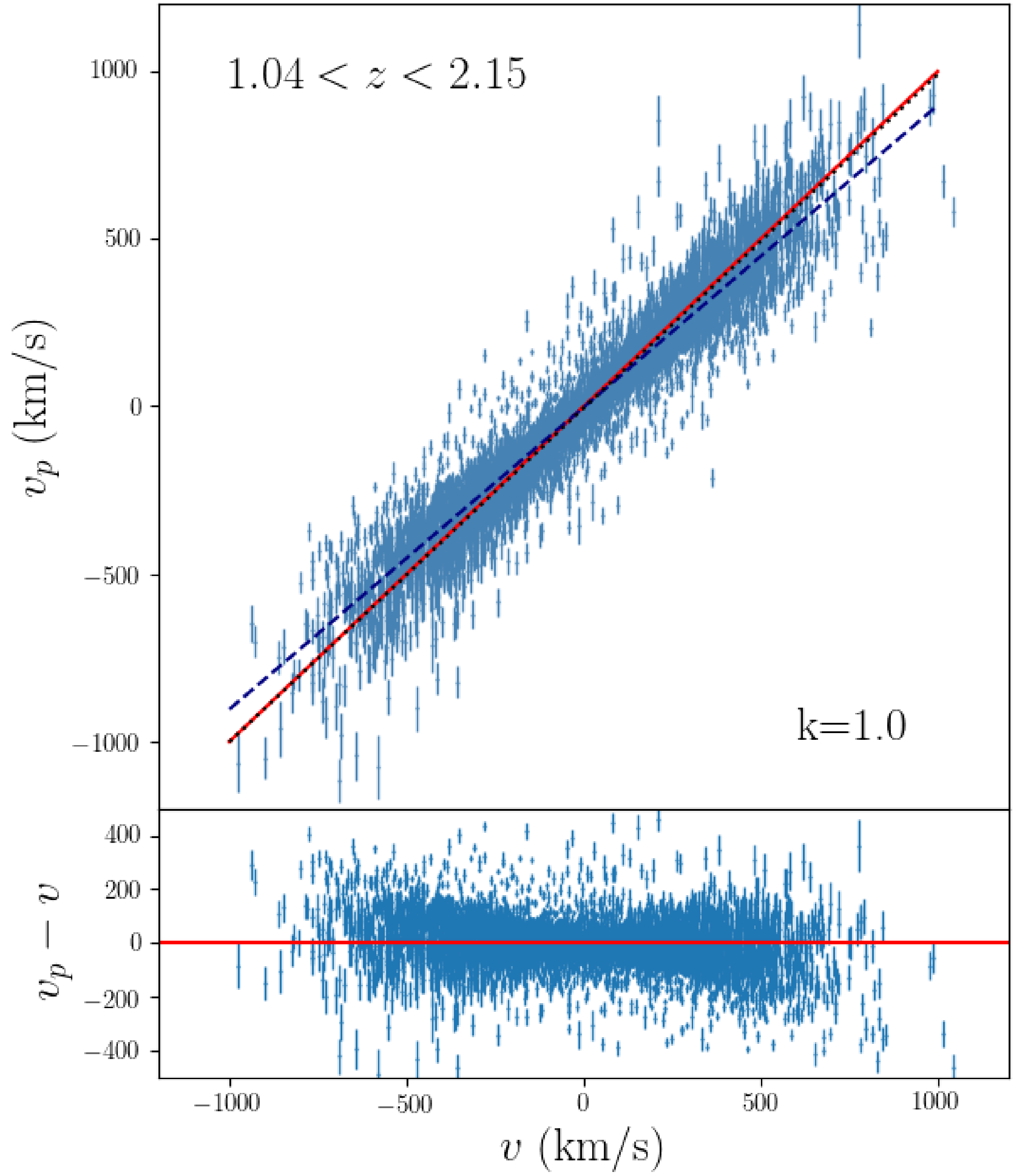

Figure 2.5: The results of the Model I trained by kSZ images of multiple redshift slices. The x-axis shows the true peculiar velocity and the y-axis indicate the predicted peculiar velocity. The red solid line shows the 1:1 ideal relation between the true and predicted velocities, the navy dashed line shows the regular linear fitting of the scatters, and the black dotted line shows the uncertainty weighted linear fitting of the scatters. The error bar shows the uncertainty of the predicted velocity using the MC Dropout method.

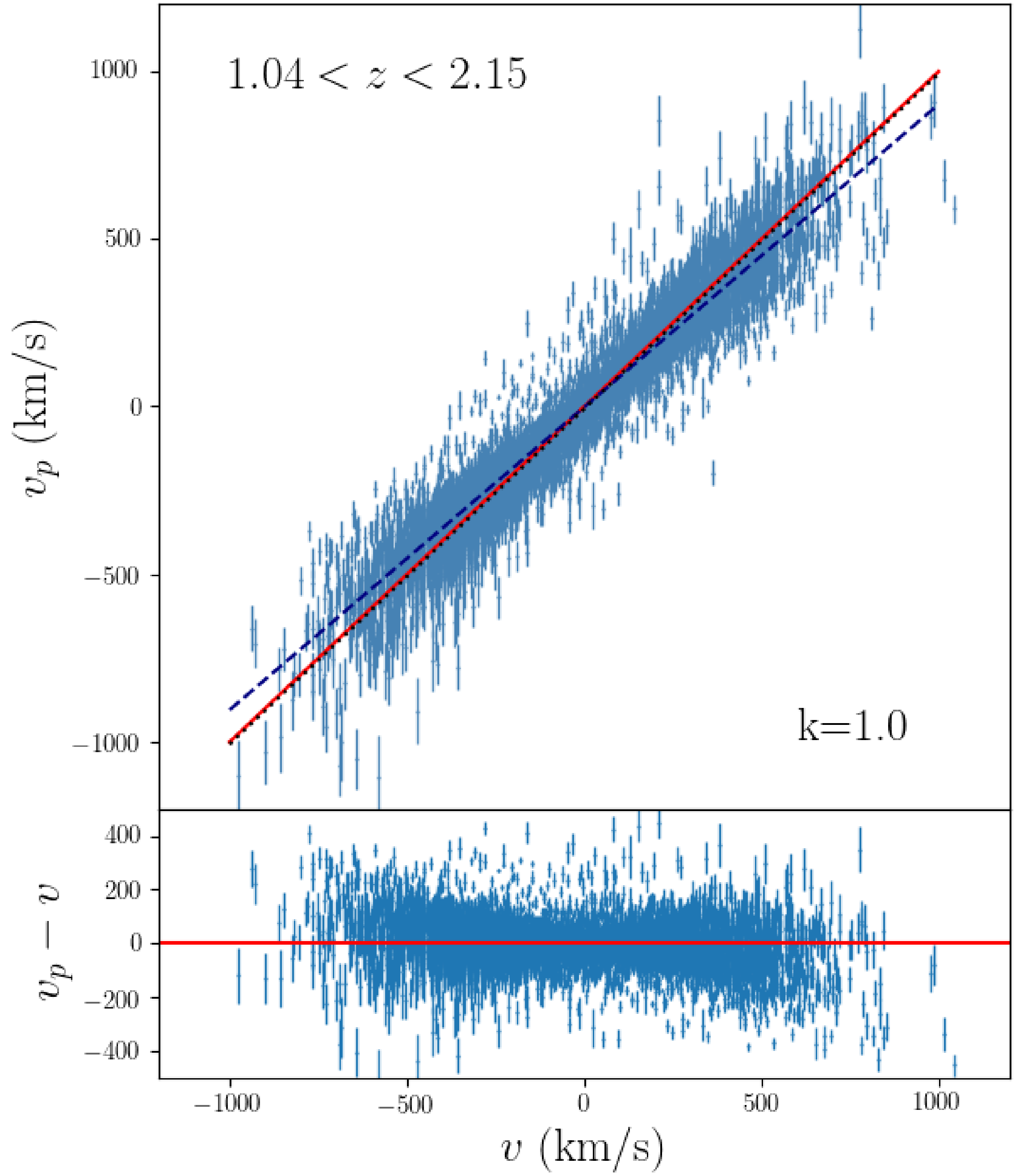

Figure 2.6: Same as figure 2.5 but for Model II trained by both kSZ and tSZ images.

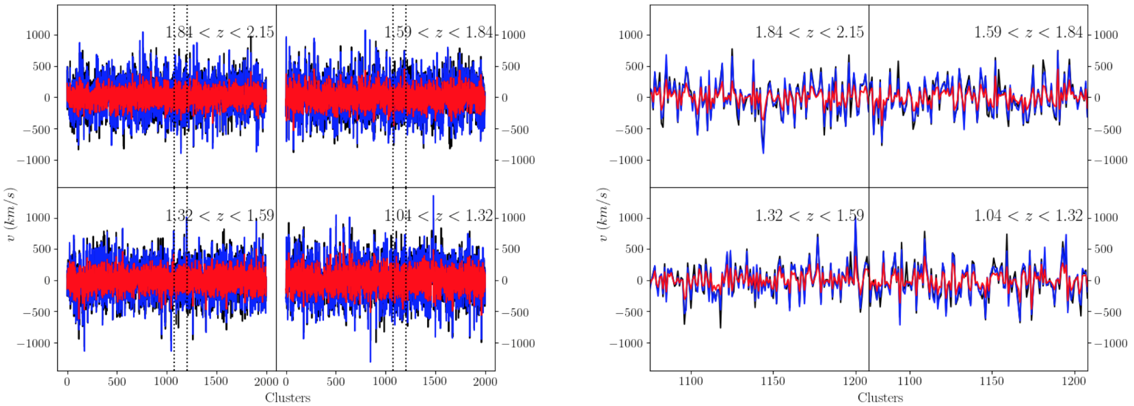

Figure 2.7: The prediction of Model I (blue line), result of conventional method (red line) and true velocities from the simulation (black line). The left panel shows the results of 2000 testing clusters in each redshift slice and the right panel shows amplification of the selected areas (areas between the black dotted lines).

### 2.5.1 Comparing with Conventional Method

The conventional method for estimating peculiar velocities from kSZ effect requires information of optical depth of each individual clusters (equation 2.1). The optical depth of individual clusters in this chapter is calculated through equation:

$$\tau_{cluster} = \frac{\int_0^{R_{vir}} \int_{l_-}^{l_+} \sigma_T N_e dl dr}{\pi R_{vir}^2}, \tag{2.3}$$

where $l_- = -100h^{-1}$Mpc, $l_+ = +100h^{-1}$Mpc and $R_{vir}$ is the virial radius of clusters. Therefore, the optical depth of individual clusters is calculated by averaging the electron density within the virial radius. The integral distance for the optical depth is 200 $h^{-1}$Mpc, which is large enough since it has already converged at 100 $h^{-1}$Mpc. The kSZ value used in the conventional method is calculated by averaging the kSZ signals of each cluster within its virial radius.

Figure 2.7 shows the results of Model I and conventional method of each redshift slice. From the figure, we could find that the predictions using the deep learning neural network and conventional method both have very strong correlations with the true peculiar velocity from the simulation. However, the predictions of conventional method show smaller magnitude than the predictions of deep learning neural networks and the true velocity. The bias caused by the smaller magnitude becomes more obvious in the figure 2.8. The slope of the fitting line of conventional method is around 0.45, which indicates a significant bias from the expected value (the true peculiar velocity).

For conventional method, the choice of the averaging area of the cluster is heuristic, therefore, the calculations of kSZ signals and optical depth are affected the averaging radius or aperture. We set the averaging radius of the calculation to be the virial radius of each cluster. However, the setting of averaging radius may miss some features of kSZ signals out side the radius. The deep learning algorithm, instead, provides a better approach for dealing with the image that it can extract more details about the cluster pattern from kSZ images with convolutional neural networks. Therefore, it provides less biased velocity predictions. In addition, the deep learning neural network provides reasonable predictions without optical depth information, which makes it more powerful for estimating peculiar velocities in observations due to difficulties in measuring optical depth.

## 2.6 Error Analysis

In this section, we quantify the uncertainty in order to test the performance of our models. Since the difference between the results of Model I and Model II is negligible, we only present the dropout uncertainties of Model I in this section. In the figure 2.5, the dropout uncertainties increase with the magnitude of the predicted velocity, and the average relative dropout uncertainty ($\Delta v_p / v_p$) is about $25\%$.

However, the value of the relative uncertainty is highly affected by its denominator, the predicted velocity $v_p$. Though the dropout uncertainty of low $v_p$ is smaller than the uncertainty of high $v_p$, the smaller denominator will increase the relative uncertainty of low $v_p$. Therefore errors of low velocity clusters might bias the estimate of the average uncertainty. We set different velocity limits ($v_{limit}$) to eliminate the effect from the low velocities, which is shown by the red line in figure 2.9. Eliminating velocities lower than 20 km $\mathrm{s}^{-1}$ reduces the average uncertainty significantly to about $12\%$. With larger velocity limits, the average uncertainty converges to about $8\%$.

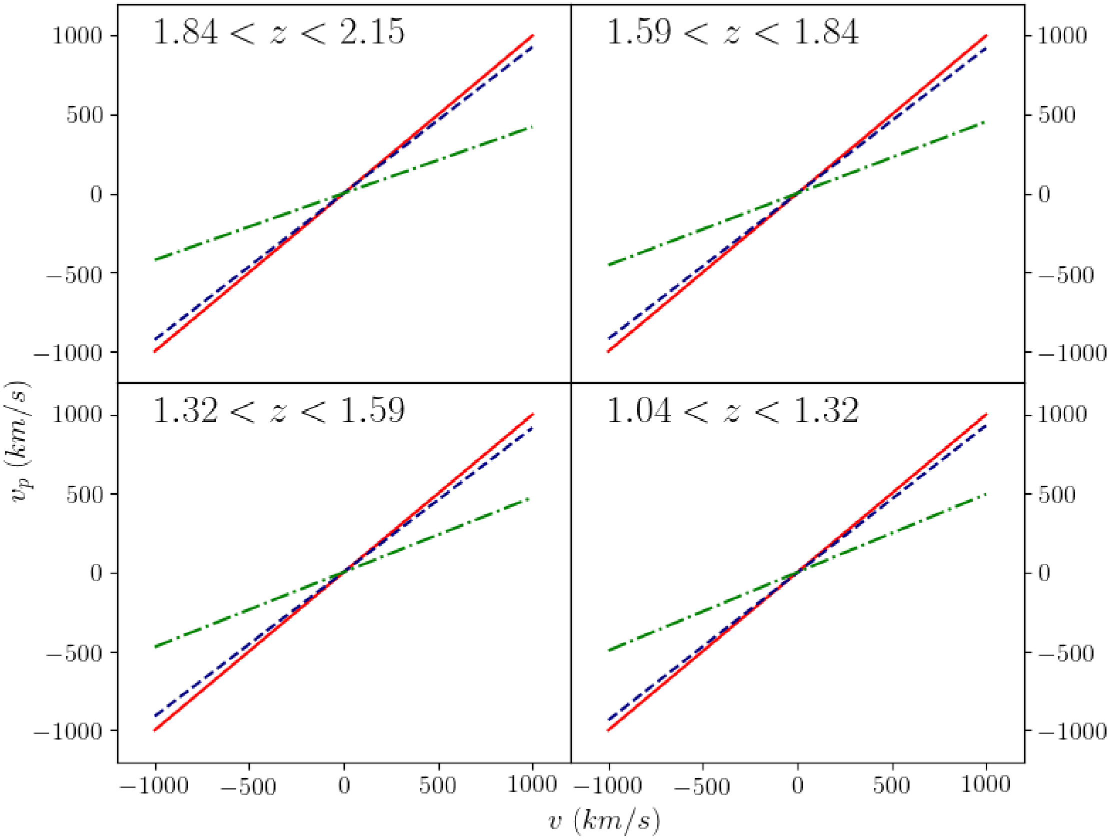

Figure 2.8: The linear fitting of the results of Model I and conventional method. The x-axis shows the true peculiar velocity and the y-axis indicate the predicted peculiar velocities. The red solid line shows the 1:1 ideal relation between the true and predicted velocities, the navy dashed line shows the regular linear fitting of Model I predictions, and the green dash-dotted line shows the fitting of the conventional method result.

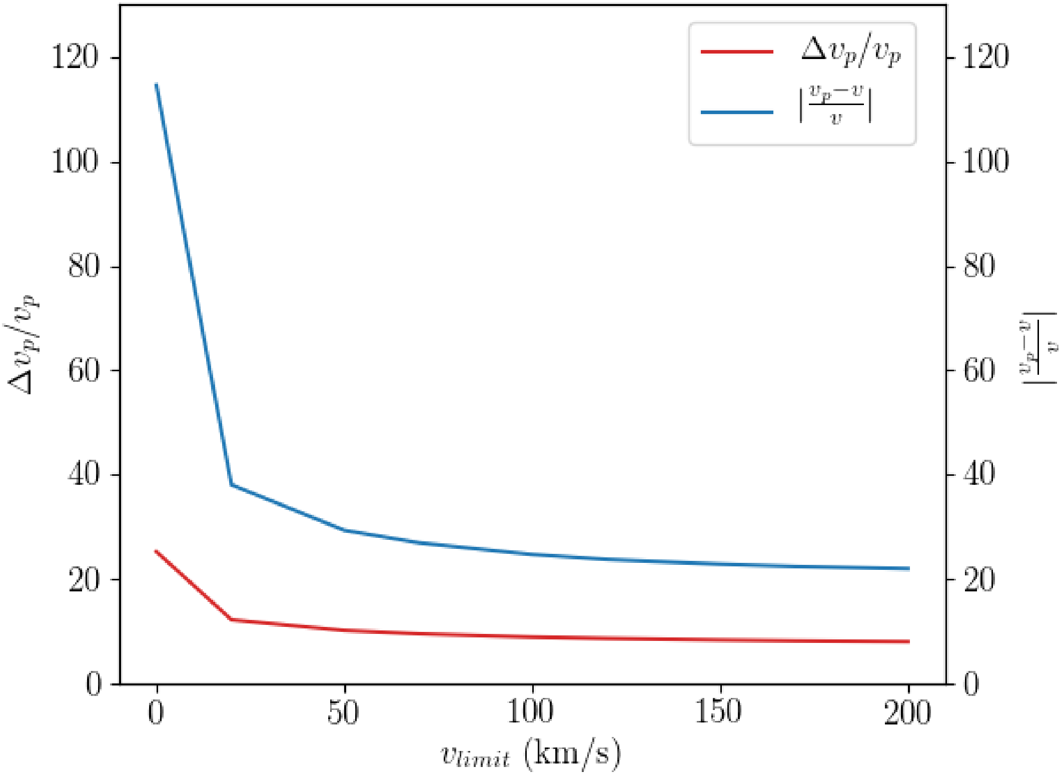

Figure 2.9: The average dropout uncertainties and the average scatter in percentage of Model I trained by data from multiple redshift slices with different velocity limits. The x-axis is the velocity limits, for instance the label 20 in x-axis means eliminating all the predicted velocities lower than 20 km $s^{-1}$ ($|v_p| < 20$). The y-axis is the average uncertainties and the average scatter in percentage. The red line indicates the average uncertainties in percentage and the blue line shows the average scatter in percentage.

In addition, the scatter between the true velocity $v$ and the predicted velocity $v_p$ is another factor that affects the accuracy of the prediction. Using the same method, we calculate the average scatter with different velocity limits, which is shown by the blue line in figure 2.9. After eliminating the velocities lower than 20 km $s^{-1}$, the average scatter becomes to about 38%.

## 2.7 Pairwise Velocity

Though our model trained by simulation data provides predictions with average uncertainties around 12%, the average scatter off from expectations is not ideal (38%). In addition, the uncertainty using observational kSZ signals can be worse due to difficulties in the detection. Therefore, ensemble statistics of peculiar velocities is more necessary than analysis of individual velocities. We apply pairwise velocity statistic to the predicted peculiar velocity.

Figure 2.10 shows the pairwise velocity statistics of Model I trained by the data from multiple redshift slices. In the pairwise velocity calculation, we use the all the predicted velocities without any velocity limits. Although the uncertainty and scatter without velocity limits are larger, the pairwise velocity results of predictions agree with the results of true velocities within tiny uncertainties (error bars). The uncertainty of the pairwise velocity are calculated through two different ways: 1) the jackknife method and 2) perturbation method that is perturbing the velocity catalog 100 times by the dropout uncertainty and calculating the statistical error through the standard deviation of the 100 perturbed catalogs. In the figure, the error bars of the perturbation method are significantly small, which are invisible.

## 2.8 Feasibility to Observations

To test the feasibility of our model to observations, we mimic observational kSZ signals by perturbing the simulated kSZ images with multiple noise models. We employ three noise schemes in the perturbations: 1) Gaussian blur noise, 2) white noise, and 3) residual tSZ signals.

Figure 2.11 shows the example images using different noise schemes. For 1) the Gaussian blur

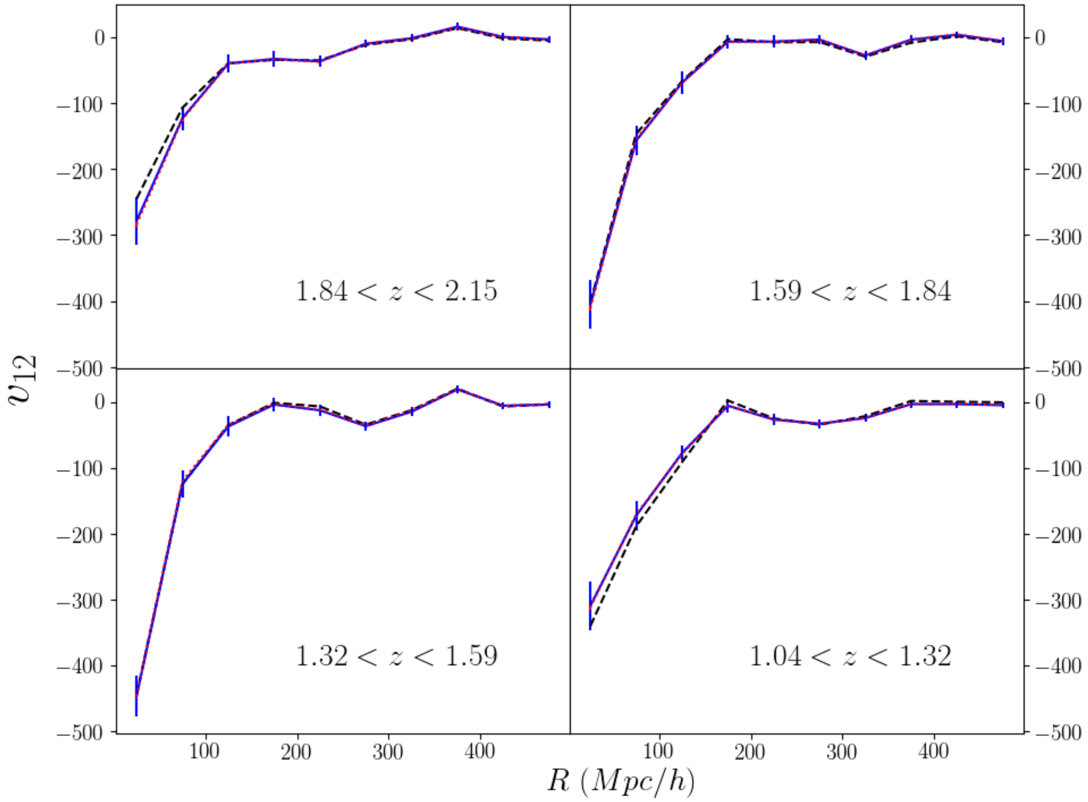

Figure 2.10: The pairwise velocity statistic of true velocities and predicted velocities of Model I. The black dashed line shows the result of true velocities, the blue line indicates the result of predicted velocities with error bars showing the statistical errors using jackknife method, and the red dotted line indicates the results of predicted velocities with error bars calculated through the perturbation method.

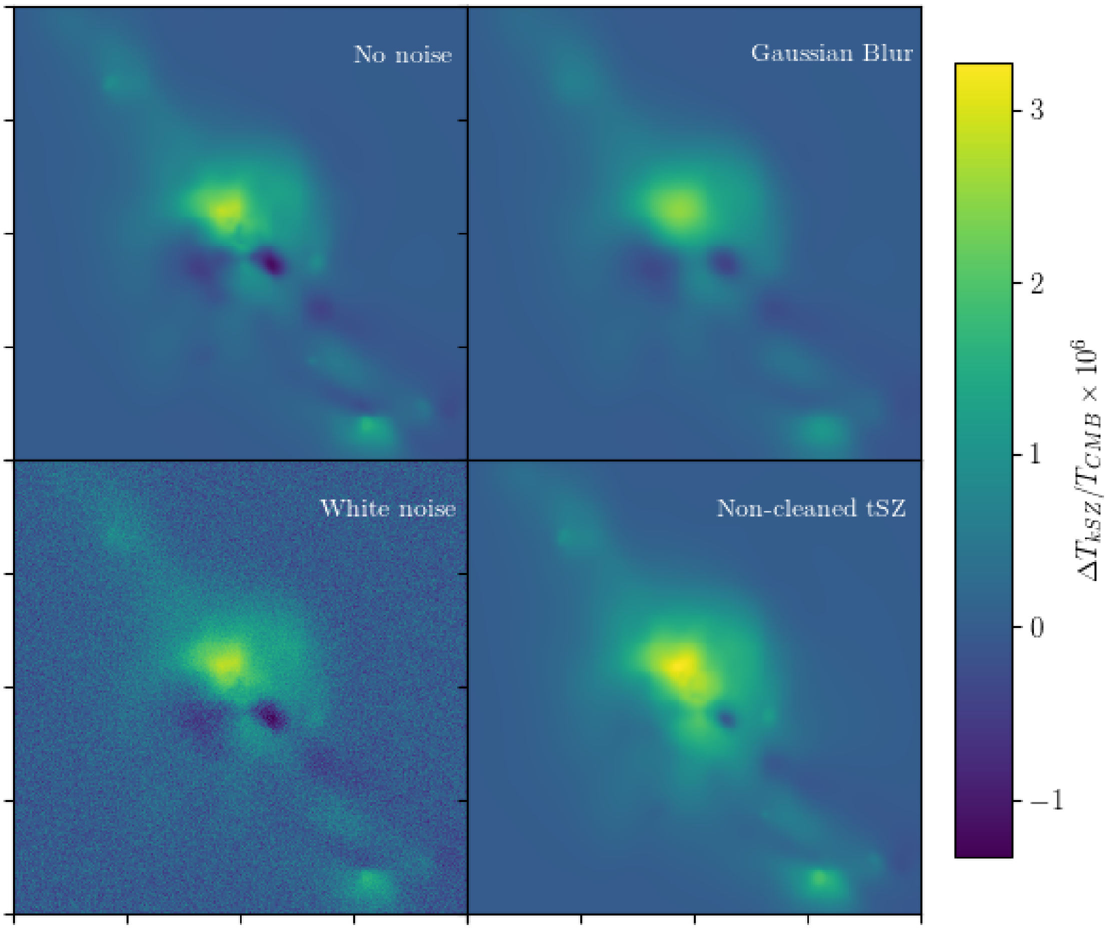

Figure 2.11: kSZ images with different noise schemes.

noise, we set the smoothing width equal to 8% of the cluster virial radius. The Gaussian blur width varies from observations. Here, we do not use any observation setting as reference for the Gaussian blur width, since we are only testing the effect of Gaussian blur noise on the model with simulation data. For 2) the white noise scheme, we use Gaussian distribution noise with the standard deviation equals to the average value of the original kSZ signal, which means the noise-to-signal ratio equals to one. Again, this ratio is only used for testing. For 3) the residual tSZ signal as noise, we added 1% tSZ signals to the kSZ image to mimic the possible noise caused by the remnant tSZ signals in kSZ observations. The 1% fraction is a testing value too.

We test our model with those noise schemes and present the predictions in figure 2.12. One should notice that we implement two methods in the test: 1). the model is trained without noise but tested with the noisy images (blue scatters and navy dotted lines); 2). the model is trained and tested both by the noisy images (green scatters and dark green dashed lines).

For method 1), our model shows great compatibility with the white noise. However, the prediction of adding the residual tSZ noise shows bias from expectations, and the bias of adding Gaussian blur noise is even worse.

For method 2), the prediction of white noise shows no difference from the method 1). Furthermore, biases caused by the Gaussian blur and residual tSZ noise are improved by training the model with noisy images, especially for the Gaussian Blur noise.

Due to the difficulty in kSZ and optical depth detections, the observational kSZ detection for individual clusters is very rare and the peculiar velocity estimated from kSZ observations is not accurate enough (Sayers et al., 2019) to train a deep learning model. Therefore, the possibility for applying the deep learning neural network model on estimating peculiar velocities from kSZ observations is to train the model with simulation data. In this chapter, we only tested three possible sources of uncertainties (Gaussian blur, white noise, and residual tSZ signal) in observations, and the intensity of those noise are set only for testing. A real kSZ observation may include more kinds of noise, such as residual CMB anisotropy signals. Therefore, to apply the deep learning algorithm to a specific observation, the simulated training data set should include noise that repre-

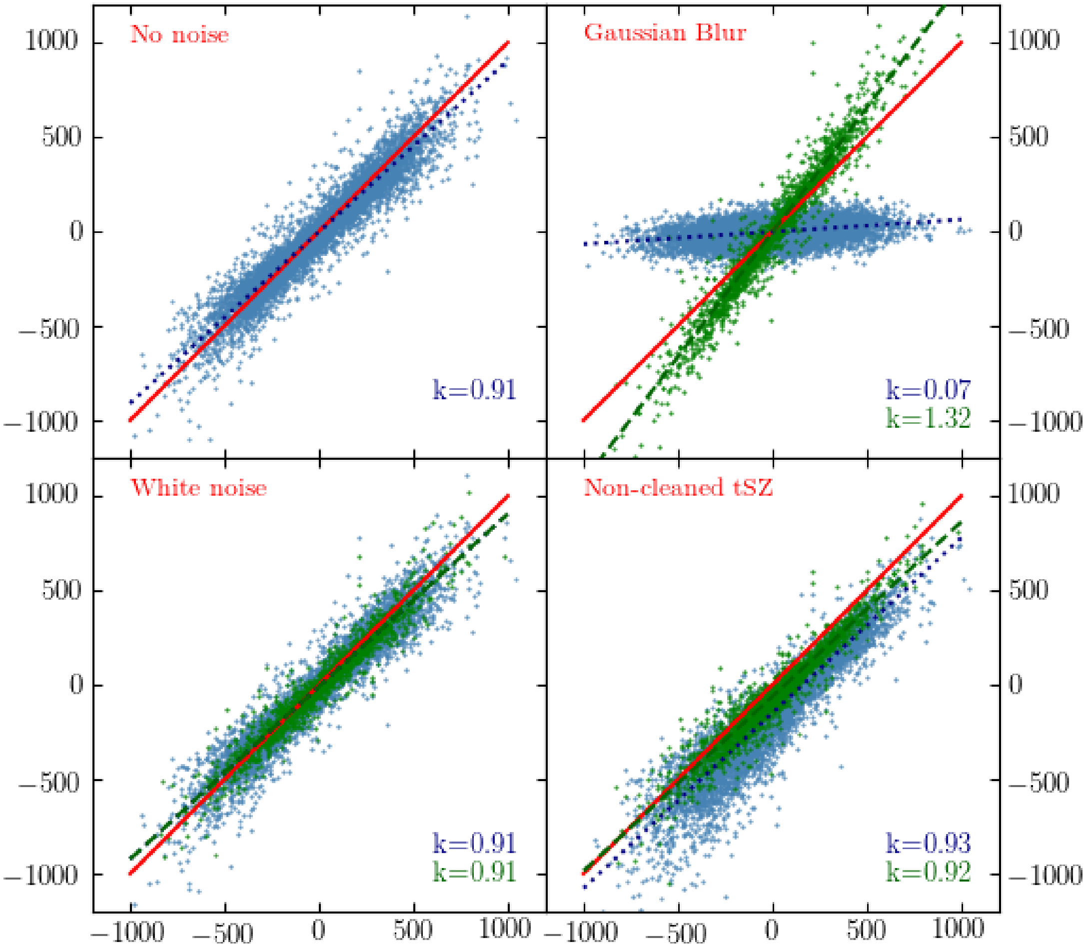

Figure 2.12: Predictions with different noise schemes. The models are trained by data of multiple redshift slices with (green) and without (blue) noise and tested by the noisy kSZ images. The red line shows the 1:1 ideal relation between the true and predicted velocities. The blue scatters and navy dotted lines show the results and linear fitting of models trained by kSZ images without noise and tested by the kSZ images with noise. The green scatters and dark green dashed line show the results of models trained and tested by kSZ images with noise.

sent the corresponding observation conditions. Considering the advantages of using deep learning neural networks than using the conventional method ( subsection 2.5.1), estimating peculiar velocities from kSZ effect with deep learning algorithms is very promising. With the upcoming kSZ detections (e.g. Mittal et al., 2018), a suitable machine learning model for observational kSZ is foreseeable.

## 2.9 Conclusion

The conventional method of estimating peculiar velocities from the kSZ effect requires several steps, such as integration of signals, map filtering, and optical depth estimates. In addition, the error in optical depth estimate makes it difficult to predict the peculiar velocity accurately.

In this chapter, we test the feasibility of using deep learning neural networks to simplify the estimation of peculiar velocities from the kSZ effect. We find our deep learning model is redshift independent, which is consistent with the theory, by comparing results using simulation data from different redshift slices.

Considering the relation between the tSZ effect and the optical depth, we build models that are trained by kSZ images only (Model I) and kSZ+tSZ images (Model II). Those two models have similar predictions and uncertainties. We find that the average uncertainty of Model I is about 12% and the average scatter is about 38%. Although the average scatter is not ideal, the pairwise velocity statistic of the predictions indicates that our model can provide reliable kSZ peculiar velocities for cosmological studies elaborate further.

The similar results of Model I and Model II indicate that including tSZ does not show significant improvement to the velocity predictions when using deep learning neural networks. According to our model structures and prediction results, we have two explanations for the inefficacy of Model II. First, the predictions of Model I have a good fitting with slope around one, therefore the improvement of adding tSZ effect is negligible. In this instant, simplifying of the kSZ peculiar velocity estimate using deep learning neural networks performs even better than our original expectations. Second, our model structure and training is not sufficiently accurate to show the effect of tSZ. Though the prediction of Model I has a good fitting curve, adding tSZ input may have the possibility to improve the scatter, further detailed studies are needed to resolve this issue.

We test applying our model to observations by perturbing the kSZ signals with three noise models: Gaussian blur, white noise and residual tSZ noise. For using noise-free training data and noisy validation data, the predictions with white noise show little bias, whereas the biases caused by the Gaussian blur and residual tSZ are significant. However, those biases can be reduced by using noisy data for both training and testing. It proves that deep learning neural network can be used to estimate peculiar velocities from the kSZ effect for simulations and for observations. A possible way for applying the deep learning neural network to observations is to train the model with simulated training data sets that include noise models corresponding to observations. However, a suitable model for observations still needs more kSZ detections of individual galaxy clusters in the future.

To summarize, using deep learning neural networks to estimate peculiar velocities from the kSZ effect is both feasible and promising. It simplifies the calculation of kSZ peculiar velocities significantly with only kSZ input, and thus avoids the error prone estimation of optical depth as well as map filtering.

## Acknowledgements

This work used the Extreme Science and Engineering Discovery Environment (XSEDE), which is supported by National Science Foundation grant number ACI-1548562.

HAF and RW were partially supported by NSF grant AST-1907404. An award of computer time was provided by the INCITE program. This research used resources of the Argonne Leadership Computing Facility, which is a DOE Office of Science User Facility supported under Contract DE-AC02-06CH11357. RW and SP acknowledge support from the Murdock Charitable Trust College Research Program.

# Chapter 3

# The Peculiar Velocity Correlation Function

In this chapter, we present an analysis of the two-point peculiar velocity correlation function using data from the Cosmicflows catalogues. The Millennium and MultiDark Planck 2 N-body simulations are used to estimate cosmic variance and uncertainties due to measurement errors. We compare the velocity correlation function to expectations from linear theory to constrain cosmological parameters. Using the maximum likelihood method, we find values of $\Omega_m = 0.315^{+0.205}_{-0.135}$ and $\sigma_8 = 0.92^{+0.440}_{-0.295}$, consistent with the Planck and WMAP CMB derived estimates. However, we find that the cosmic variance of the correlation function is large and non-Gaussian distributed, making the peculiar velocity correlation function less than ideal as a probe of large-scale structure. The results in the chapter were first discussed in Wang et al. (2018).

## 3.1 Introduction

The peculiar velocity field is a sensitive probe of mass fluctuations on large scales and a powerful tool for constraining cosmological parameters. However, the precision measurement of the velocity field is limited by the error in the measurement of radial distance. Many methods have been introduced to measure the distance with the smallest possible error, such as Tully-Fisher (TF) (Tully & Fisher, 1977), Faber-Jackson (Faber & Jackson, 1976), and the Fundamental Plane (FP) (Djorgovski & Davis, 1987; Dressler et al., 1987b).

These methods do not directly measure radial distance. Rather they estimate the distance modulus, which is proportional to the logarithm of the distance. While the errors in the distance modulus are Gaussian, the distances themselves have a non-Gaussian error distribution which may bias the results. To address this issue, Watkins & Feldman (2015a) introduced a new unbiased estimator of the peculiar velocity that gives Gaussian distributed errors. In this chapter we will use this unbiased estimator together with the measured redshift (see also Davis & Scrimgeour, 2014; Tully et al., 2016) to derive the velocity correlation function.

The fractional observational errors of the radial distances are typically on the order of $\approx 20\%$ (e.g. Masters et al., 2006; Springob et al., 2007; Tully et al., 2013), and peculiar velocities tend to have errors proportional to the distances, which may be large. Because of this large error, a single peculiar velocity measurement is not a good approximation of the velocity of a galaxy. However, statistical ensembles, especially the low-order moment statistics, may be a good estimator of the cosmic velocity field and thus a good tracer of the underlying mass distribution in the Universe (e.g. Feldman & Watkins, 2008; Watkins et al., 2009; Feldman et al., 2010; Davis et al., 2011; Nusser et al., 2011; Macaulay et al., 2011; Turnbull et al., 2012; Macaulay et al., 2012; Nusser, 2014; Springob et al., 2014a; Johnson et al., 2014; Scrimgeour et al., 2016a).

Many recent studies have focused on the bulk flow, which is the lowest order statistic of the velocity field and is generally thought of as the average of peculiar velocities in a volume (e.g. Abate & Feldman, 2012; Nusser, 2014; Kumar et al., 2015; Seiler & Parkinson, 2016; Scrimgeour et al., 2016b; Nusser, 2016). Bulk flows are typically calculated using one of two popular methods.

The first is the maximum likelihood estimate (MLE) method (e.g. Kaiser, 1988; Watkins & Feldman, 2007). The MLE formalism estimates the bulk flow as a weighted average of the sample velocities, with the weights calculated to minimize its overall uncertainty given the positions, velocities and errors distributions in the catalogue. The formalism reduces the entire dataset to three numbers, namely the components of the bulk flow vector. Since the particular data and error distribution in the surveys analyzed are unique to each catalogue, it is difficult to compare the bulk flow calculated using this method between independent surveys.

The other popular formulation is the minimum variance (MV) method (Watkins et al., 2009; Feldman et al., 2010; Scrimgeour et al., 2016a). The MV formalism minimizes the differences between the actual observational data and an “ideal" survey that may be designed to probe a volume in a particular way. It can be used with Gaussian-weighted (Agarwal et al., 2012b) or tophat-weighted ideal survey distributions (Davis et al., 2011; Hoffman et al., 2016). Because it uses a standard ideal survey bulk flow as a reference, it easily lends itself to direct comparisons between independent surveys.

Another approach to studying the large-scale velocity field is the pairwise velocity statistic ($v_{12}$) (Ferreira et al., 1999; Juszkiewicz et al., 2000; Feldman et al., 2003; Hellwing, 2014; Hellwing et al., 2014), which is the mean value of the peculiar velocity difference of a galaxy pair at separation $r$. Recent studies show that it can also be used to detect the kinetic Sunyaev-Zel'dovich effect (Zhang et al., 2008; Hand et al., 2012; Planck Collaboration et al., 2016a).

In this chapter we will use a different approach to probe the cosmic velocity field, namely the peculiar velocity correlation function. It was first introduced by Gorski (1988) and further elucidated in Gorski et al. (1989). In subsequent studies, the velocity correlation function has shown potential for providing interesting constraints on cosmological parameters (e.g. Jaffe & Kaiser, 1995; Zaroubi et al., 1997; Juszkiewicz et al., 2000; Borgani et al., 2000; Abate & Erdoğdu, 2009; Nusser & Davis, 2011; Okumura et al., 2014; Howlett et al., 2017). At the time that the original studies of velocity correlation were done, the small sizes of peculiar velocity catalogues limited its usefulness. The recent availability of large, calibrated catalogues of peculiar velocities and large-scale cosmological simulations suggests that the it is worthwhile to revisit the velocity correlation function as a cosmological probe.

Here we will present a feasibility study of this statistic for the study of the large-scale-structure given state-of-the-art peculiar velocity catalogues CosmicFlow-2 (CF2) (Tully et al., 2013) and CosmicFlows-3 (CF3) (Tully et al., 2016). In particular, we assess the magnitude of the cosmic variance expected in the correlation function using mock catalogues extracted from the Millennium Simulation[1]. Using this result, we show that the velocity correlation functions calculated from CF2 and CF3 are consistent with the standard cosmological model. However, our results suggest that the particular cosmological volume we live in is on the higher end of the cosmic variance,

---

[1] http://gavo.mpa-garching.mpg.de/Millennium/

suggesting that the $\sim 150h^{-1}$Mpc radius region around us has greater large scale motions than one would expect on average.

The organization of this chapter is as follows: in section 3.3 we detail our use of N-body simulations to generate mock surveys. In section 3.2 we introduce the velocity correlation statistic and the methods used to calculate it. In Section 3.4 we discuss the use of the Monte Carlo method for error analysis. In section 3.5, we show the results for the velocity correlation function using the CosmicFlows catalogues. In Section 3.6 we explore using the correlation function to constrain cosmological models. Section 3.7 concludes this chapter.

## 3.2 Velocity Correlations

Measuring the velocity correlation tensor $\Psi_{ij}(r) = \langle v_i(r_1) v_j(r_2) \rangle$ directly is untenable in practice, since we can only measure the radial component of a galaxy velocity. Gorski et al. (1989) got around this problem by introducing two velocity correlation statistics that use only the radial peculiar velocity, $u = \mathbf{v} \cdot \hat{\mathbf{r}}$,

$$\psi_1(r) \equiv \frac{\Sigma_{\text{pairs}(r)} u_1 u_2 \cos\theta_{12}}{\Sigma_{\text{pairs}(r)} \cos^2\theta_{12}}, \tag{3.1}$$

$$\psi_2(r) \equiv \frac{\Sigma_{\text{pairs}(r)} u_1 u_2 \cos\theta_1 \cos\theta_2}{\Sigma_{\text{pairs}(r)} \cos\theta_{12} \cos\theta_1 \cos\theta_2}. \tag{3.2}$$

where $r = |\mathbf{r_2} - \mathbf{r_1}|$ is the scalar separation between galaxies and the sums are performed over separation bins, the quantities $u_1$ and $u_2$ are the radial peculiar velocities of the first and second galaxy in a given pair, respectively. The angles $\theta_1$, $\theta_2$ are the angles between the position vectors of galaxies, $\mathbf{r_i}$, and the vector separating them, *e.g.* $\cos\theta_1 = \hat{\mathbf{r}}_\mathbf{1} \cdot \hat{\mathbf{r}}$, where $\hat{\mathbf{r}} = \frac{\mathbf{r_2} - \mathbf{r_1}}{r}$. The angle $\theta_{12}$ is the angle between the position vectors of the two galaxies, so that $\cos\theta_{12} = \hat{\mathbf{r}}_\mathbf{1} \cdot \hat{\mathbf{r}}_\mathbf{2}$. Thus the numerator of $\psi_1$ is the sum over the dot products of the radial peculiar velocities, while that of $\psi_2$ is the sum over the products of the components of the radial velocities along the separation vector.

Theoretically, the velocity field should be a potential flow field (Bertschinger & Dekel, 1989), so that the radial peculiar velocity field should in principle carry all of the information contained in the full 3-D velocity field. Indeed, Gorski et al. (1989) showed that when making this assumption, the radial and transverse velocity correlation tensor $\Psi_{ij} = \langle v_i v_j \rangle$ can be recovered from the statistics $\psi_1$ and $\psi_2$. We begin by expressing the correlation between radial peculiar velocities in terms of the velocity correlation tensor,

$$\langle u_1 u_2 \rangle = \hat{r}_1 \hat{r}_2 \langle v_{1i} v_{2j} \rangle \hat{r}_{1i} \hat{r}_{2j} \,, \tag{3.3}$$

Gorski (1988) showed that the full velocity correlation tensor can be written in terms of two independent functions $\Psi_{\|}(r)$ and $\Psi_{\perp}(r)$, the correlation of the components of the velocity along and perpendicular to the vector separating two galaxies respectively,

$$\langle v_{1i} v_{2j} \rangle = \left[ \Psi_{\|}(r) - \Psi_{\perp}(r) \right] \hat{r}_{1i} \hat{r}_{2j} + \Psi_{\perp}(r) \delta_{ij} \,, \tag{3.4}$$

and $\mathbf{r} = \mathbf{r_2} - \mathbf{r_1}$.

Plugging Eqs. (3.3) and (3.4) into Eqs. (3.1) and (3.2) results in

$$\begin{aligned} \psi_1(r) &= A(r)\Psi_{\|} + [1 - A(r)]\Psi_{\perp} \,, & (3.5) \\ \psi_2(r) &= B(r)\Psi_{\|} + [1 - B(r)]\Psi_{\perp} \,, & (3.6) \end{aligned}$$

where functions $A(r)$ and $B(r)$ are given by

$$\begin{aligned} A(r) &= \frac{\Sigma_{\mathrm{pairs}(r)} \cos\theta_1 \cos\theta_2 \cos\theta_{12}}{\Sigma_{\mathrm{pairs}(r)} \cos^2\theta_{12}} \,, & (3.7) \\ B(r) &= \frac{\Sigma_{\mathrm{pairs}(r)} \cos^2\theta_1 \cos^2\theta_2}{\Sigma_{\mathrm{pairs}(r)} \cos\theta_{12} \cos\theta_1 \cos\theta_2} \,. & (3.8) \end{aligned}$$

Note that the functions $A$ and $B$ are independent of the velocities and only depend on the distribution of the galaxies in the sample.

Inverting these relations, we can express the parallel and perpendicular components of the velocity correlation as simple linear combination of $\psi_1$ and $\psi_2$,

$$\psi_{\parallel}(r) = \frac{[1-B(r)]\,\psi_1(r) - [1-A(r)]\,\psi_2(r)}{A(r)-B(r)}, \tag{3.9}$$

$$\psi_{\perp}(r) = \frac{B(r)\psi_1(r) - A(r)\psi_2(r)}{B(r)-A(r)}. \tag{3.10}$$

These relations allow us to estimate the physically meaningful 3-D velocity correlations from catalogues using only measurements of radial peculiar velocities.

Eqs. (3.1), (3.2), (3.7), (3.8), (3.9) and (3.10) all involve sums over pairs of galaxies whose separation falls within a given bin. Thus it is important to determine the positions of galaxies as accurately as possible. Here we will follow previous researchers (Gorski et al., 1989; Borgani et al., 2000) and use redshift to estimate galaxy distances and hence galaxy separations. Redshift provides more accurate distances than distance indicators for all but the closest galaxies in our catalogues and also removes the need for Malmquist bias corrections (e.g. Davis et al., 1996; Willick et al., 1997; Tully et al., 2016).

## 3.3 Mock Catalogues

To study the properties of the velocity correlation function, we use mock catalogues generated from the Virgo - Millennium Database of the Millennium Simulation (Springel et al., 2005), which contains the result of the L-Galaxies run used in De Lucia & Blaizot (2007). The Millennium Simulation is a dark matter only simulation using the GADGET-2 simulation code (Springel et al., 2005). Table 3.1 (Guo et al., 2013) shows the cosmological parameters of the simulation we used. We generate 100 mock catalogues for each real survey centered at random locations in the box. Each mock catalogue is designed to have the same radial selection function as the real CF2/CF3 surveys we use here.

Each of the CosmicFlows catalogues comes in two versions, one where galaxies are given individually, which we will call the galaxy compilation, and a group catalog where galaxies in known groups have had their distance moduli and redshifts averaged, resulting in a single velocity

Table 3.1: The cosmological parameters of the Millennium Simulation

| | |
|---|---|
| Matter density, $\Omega_m$ | 0.272 |
| Cosmological constant density, $\Omega_\Lambda$ | 0.728 |
| Baryon density, $\Omega_b$ | 0.045 |
| Hubble parameter, $h$ ($100 kms^{-1}Mpc^{-1}$) | 0.704 |
| Amplitude of matter density fluctuations, $\sigma_8$ | 0.807 |
| Primordial scalar spectral index, $n_s$ | 0.967 |
| Box size ($h^{-1}$Mpc) | 500 |
| Number of particles | $2160^3$ |
| Particle mass, $m_p$ ($10^8 h^{-1} M_\odot$) | 8.61 |
| Softening, $f_c$ ($h^{-1} kpc$) | 5 |

and position for the group as a whole . The CF2 galaxy catalogue (CF2-galaxy) (Tully et al., 2013) contains 8,135 galaxies, whereas the CF2 group catalogue (CF2-group) contains 4,842 galaxies and groups. The characteristic depth of both catalogues is $\sim 33\ h^{-1}$Mpc (Watkins et al., 2009; Feldman et al., 2010; Agarwal et al., 2012b). The CF2 catalogues were assembled by a compilation of Type Ia Supernovae (SNIa) (Tonry et al., 2003), Spiral Galaxy Clusters (SC) TF clusters (Giovanelli et al., 1998; Dale et al., 1999), Streaming Motions of Abell Clusters (SMAC) FP clusters (Hudson et al., 1999, 2004), Early-type Far Galaxies (EFAR) FP clusters (Colless et al., 2001), TF clusters (Willick, 1999), the SFI++ catalogue (Masters et al., 2006; Springob et al., 2007, 2009), group SFI++ catalogue (Springob et al., 2009), Early-type Nearby Galaxies (ENEAR) survey (da Costa et al., 2000; Bernardi et al., 2002; Wegner et al., 2003) and a surface brightness fluctuations (SBF) survey (Tonry et al., 2001).

The CF3-galaxy catalogue (Tully et al., 2016) contains 17,669 galaxies, including all the CF2 galaxy distances together with 2,257 distances derived from the correlation between galaxy rotation and luminosity with photometry at $3.6\mu m$ obtained with Spitzer Space Telescope and 8,885 distances based on the Fundamental Plane sample derived from the Six Degree Field Galaxy Survey (6dFGS) (Springob et al., 2014b). The CF3-group catalogue contains 11,878 groups and galaxies.

We select the galaxies for each mock survey by ensuring a best fit to the radial selection function of the real catalogue, parametrized as (see also Feldman et al., 1994)

$$f(r) = \mathcal{A} \left( \frac{r}{r_0} \right)^{n_1} \left[ 1 + \left( \frac{r}{r_0} \right)^{n_1+n_2} \right]^{-1} , \tag{3.11}$$

where $\mathcal{A}$ is the scaling factor, which depends on the number of galaxies and the bin size. The constants $n_1$ and $n_2$ are the powers that fit the volume- and magnitude-limited regions, respectively, and $r_0$ is the distance at which the number of galaxies is maximum. At $r < (>)\ r_0$, volume (magnitude)–limited effects dominate, respectively.

The galaxies in the real surveys are binned by their estimated distance, and the selection function given in Eq. 3.11 is fit to the radial distribution by the least-squares method, as shown in Fig. 3.1 (the smooth dashed curve). The resulting fit is then used to select the correct number of galaxies from the Millennium Simulation at each distance. The relevant selection function parameters for each of the four catalogues we use are fairly similar. For each real survey catalogue, we generated 100 mock catalogues by placing the centers of the mock catalogs randomly in the simulation box, which can be regarded as Copernican observers.

We studied in detail the construction of mock catalogues, both their distribution in the simulation boxes and the parameters used to produce them. A recent study choosing local group observers was introduced by Hellwing et al. (2017), that provides a detailed study of cosmic variance by considering differences in velocity observables as measured by a Copernican observer and its local group (LG)–equivalents. As discussed in Sec. 3.4.1 below, the differences between the velocity correlation functions in our mock catalogs are cosmic variance dominated; the large variations between random observers thus overwhelm the difference between choosing random or LG–equivalent locations. The angular distribution of the CosmicFlows surveys is not considered in the mock catalogues, since its effect was found to be negligible on both velocity correlation statistics and cosmological parameter estimation.

The mean distance between the centers of mock catalogs from Millennium Simulation is about 250 $h^{-1}$Mpc, which is not large enough for the mock catalogs to be completely independent.

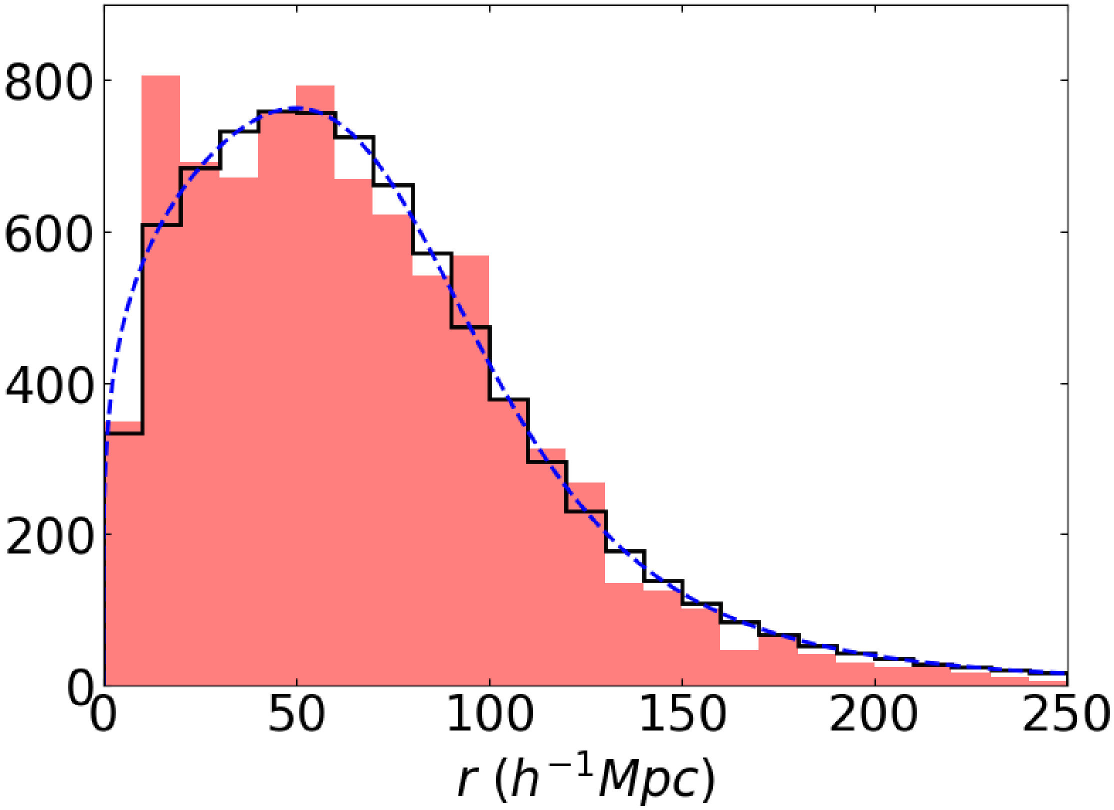

Figure 3.1: The radial distribution the CF2-galaxy survey (red histogram) and an example of one of its mock catalogues (solid line histogram). The dashed blue line indicates the selection function for CF2-galaxy survey given in Eq. 3.11 with parameter values $\mathscr{A} = 933$, $r_0 = 96\ h^{-1}$Mpc, $n_1 = 0.23$, and $n_2 = 4.25$. The bin width is $10h^{-1}$Mpc. For the real survey, the fit has a $\chi^2 = 191$ for 25 degrees of freedom, whereas for the mock survey it is $\chi^2 = 41.7$.

However, we also tested mock catalogs from the MultiDark Planck 2 (MDPL2[2]) Simulation (box size equals 1,000 $h^{-1}$Mpc, mean center separation about 680 $h^{-1}$Mpc) and found no significant differences in the results.

## 3.4 Variance Analysis

To use velocity correlation statistics effectively, one needs to know how much they can be expected to vary between different locations and from sample to sample due to measurement errors. While it would be ideal to estimate variances theoretically, the sums over pairs form of the statistics

---

[2] https://www.cosmosim.org/cms/simulations/mdpl2/

make this extremely difficult. Here we will estimate the variances using mock surveys from the Millennium Simulation data. As mentioned before, we also used the MDPL2 simulation to verify that the results are robust.The two main components of the variance of the velocity correlation statistics are the cosmic variance, which can be estimated using mock surveys drawn from different locations in the simulation box, and measurement uncertainty, which can be estimated by making multiple realizations of a single survey with randomly generated errors.

### 3.4.1 Cosmic Variance

In section 3.3, we discussed generating one hundred simulation catalogues for each real survey. Since the simulation box is much larger than the survey volume, if we draw mock surveys centered on random galaxies in the box we can study how much our correlation statistics are affected by cosmic variance.

In figure 3.2 we show the mean and variance of the velocity correlation function with 500 km $s^{-1}$ bin width calculated from CF2-galaxy mock catalogues. In order to match our calculations with real catalogues, we have calculated the correlation function using the redshift instead of distance as discussed above. Using CF2-groups instead of CF2-galaxies makes very little difference in our results.

Comparing the six plots in Fig 3.2, we might be surprised that the velocity independent functions $A(r)$ and $B(r)$ also show cosmic variance. This is due to the fact that even though the simulation catalogues have the same radial selection functions, each mock catalogue has a slightly different distribution of galaxies due to the particular locations of the galaxies in the region of the simulation box where the catalogue was drawn from.

Several things are notable in Fig. 3.2. First, we see that the statistic $\psi_2$ appears to be well behaved on CosmicFlow type surveys, $\psi_2$ of CF3 shows similar result. This is in contrast to the Gorski et al. (1989) findings (Fig. 2 in Gorski et al. (1989)) , who neglected to use this statistic since it was deemed less stable when applied to the catalogues that were available at the time.

Further, we see that the cosmic variance in the velocity correlation function is large, of the

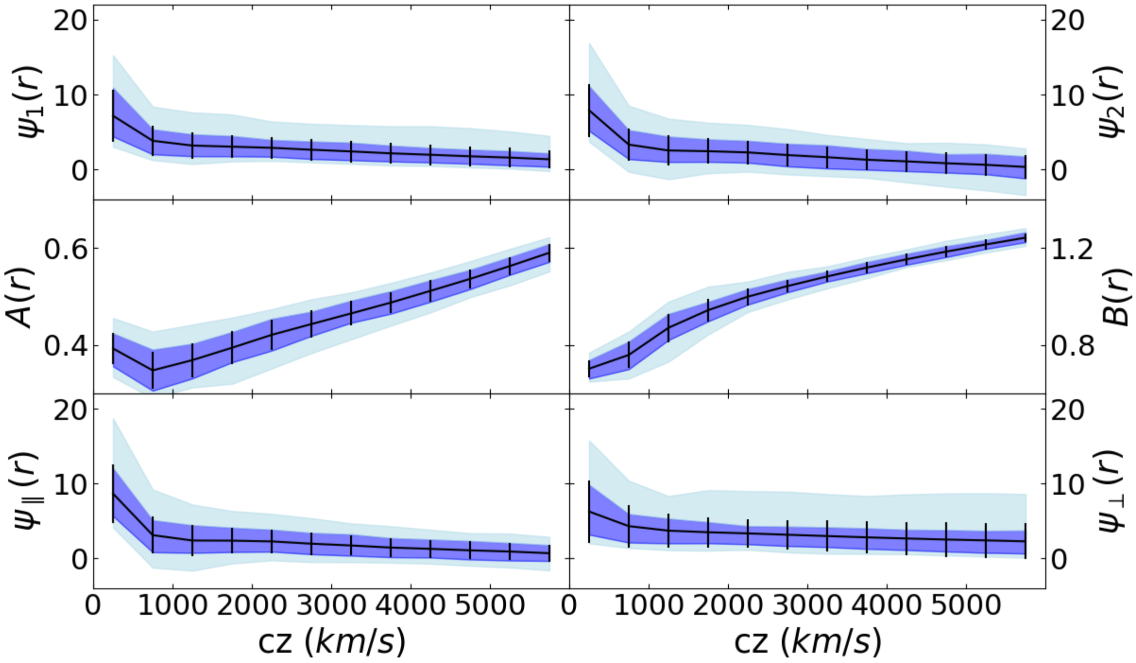

Figure 3.2: The mean and cosmic variance of $\psi_1$, $\psi_2$, $A(r)$, $B(r)$, $\psi_\parallel$ and $\psi_\perp$, of 100 mock catalogues with CF2-galaxy distribution. $\psi_1$, $\psi_2$, $\psi_\parallel$ and $\psi_\perp$ are in units of $(100 \text{ km s}^{-1})^2$. The center solid line and error bars show the average and standard deviation of each function. The contours indicate the regions containing 68% and 95% of the results. The bins in this plot are 500 km $\text{s}^{-1}$ wide.

order of the mean, and the distribution of cosmic variance is skewed, and thus non-Gaussian. This can be seen most clearly from the 95% contours in Fig. 3.2, which are not symmetric about the mean. We can understand the skewness by noticing that the correlation function is quadratic in the velocity, which is itself a Gaussian distributed variable. Thus we expect the cosmic variance of the correlation functions to have a bi-variate Gaussian distribution, that is, a Wishart distribution (Wishart, 1928), which is a generalization of a $\chi^2$-distribution. Like the $\chi^2$ distribution, this distribution has exponential tails which fall off much more slowly than Gaussian tails. We expect that the correlation functions also contain contributions from noise, which we would expect to be Gaussian distributed.

In general, then, the variance in the correlation function has a distribution that is a convolution of a Wishart and a Gaussian, as the example in Fig. 3.3 clearly shows. The skewness becomes more non-Gaussian in larger separation bins, due to the lower number of degrees of freedom, in that fewer modes are contributing to the correlation function. The non-Gaussian distribution of the cosmic variance, in particular, the exponential tails of the distribution, limits the information we get using the velocity correlation function. Thus, both the size of the cosmic variance and its distribution pose challenges for using velocity correlation statistics to constrain cosmological models.

We compare the cosmic variance of mock catalogs from the Millennium and the MDPL2 Simulations, with and without including an angular mask (*i.e.* reproducing the CF3 angular distribution). We find the mean measurement and the contours of the cosmic variance are all within the uncertainties and show little differences across the samples. The cosmic variance from those four kinds of mock catalogs are combinations of Wishart and Gaussian distributions; however, their distribution parameters may be different, which leads to variations in the cosmological constraints. The cosmic variance distribution is somewhat sensitive to non-Gaussian skewness (*e.g.* bin width, correlation truncations, and mock selections), which leads to some differences in cosmological parameter constrains. This topic will be discussed further in section 3.6.

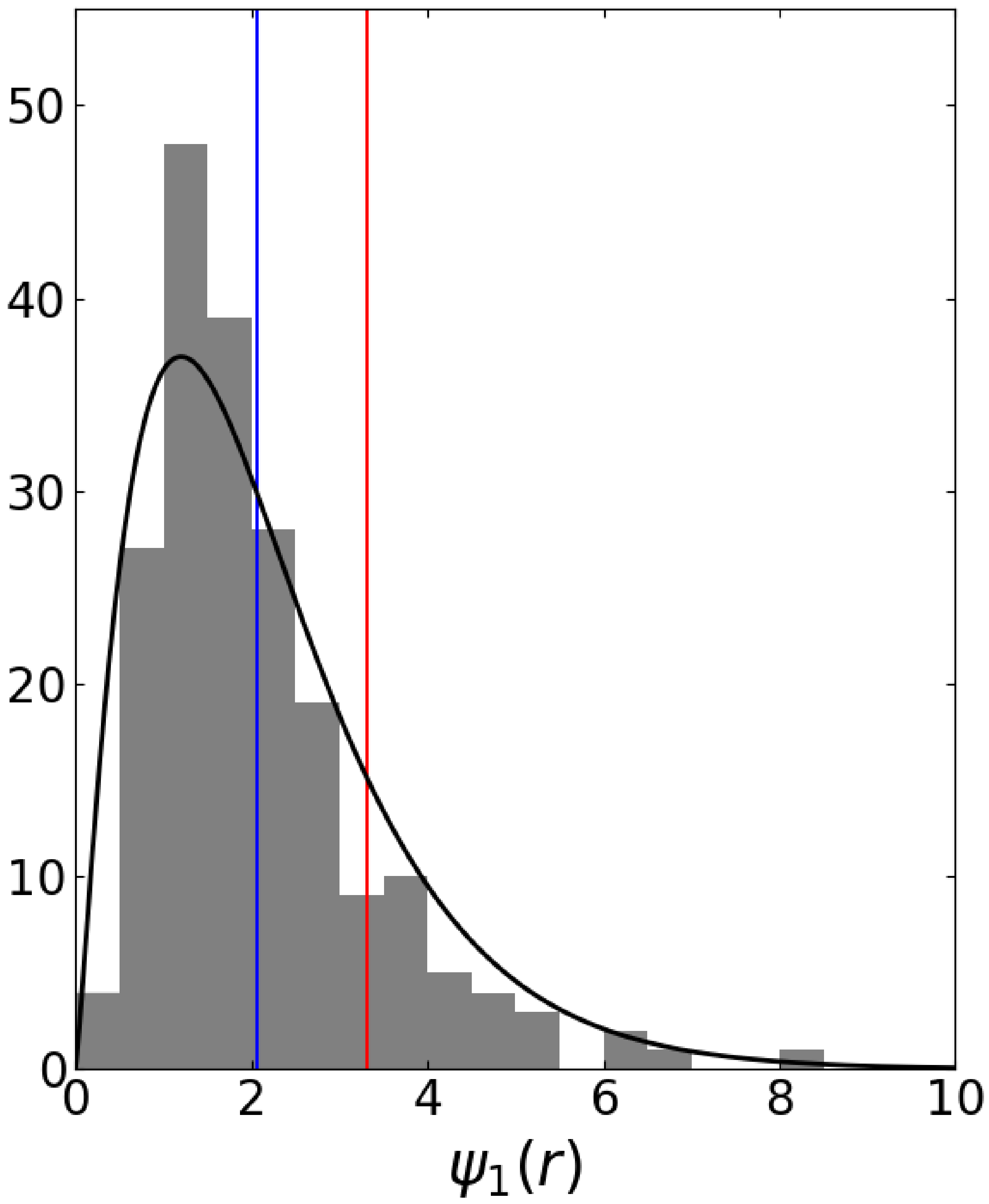

Figure 3.3: The distribution of $\psi_1$ in 4,000-4,500 km s$^{-1}$ bin of 200 mock catalogues, in units of (100 km s$^{-1}$)$^2$. The blue vertical line on the left is the mean of the mock catalogues ($\overline{\psi_1}$); the red vertical line on the right is the CF3-galaxy catalogue measurement in the bin; the black solid curve is the Wishart distribution fitting.

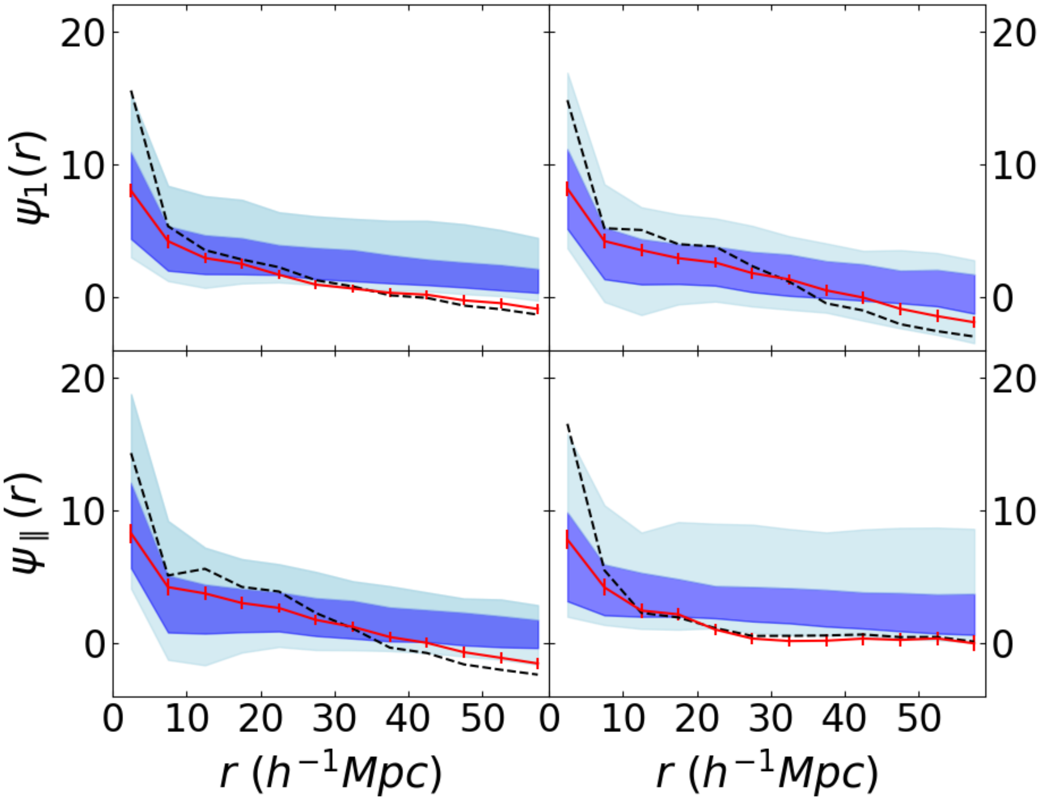

Figure 3.4: The result of perturbing the distance moduli of one CF2-galaxy simulation catalogue, in units of (100 km $s^{-1}$)$^2$. The bin width is 500 km $s^{-1}$ (redshift). The black dashed line shows the original simulation catalogue; the red solid line with error bars is the average of the perturbed catalogues. The error bars show the standard deviation of the perturbed results, which is regarded as the measurement error. The background contours indicate the cosmic variance from Fig. 3.2.

### 3.4.2 Measurement Error

The other main source of uncertainty in the correlation functions comes from the uncertainty of the peculiar velocity measurements. Because the peculiar velocity measurements from the simulation do not have uncertainty, we used a Monte Carlo method to simulate distance measurement errors, which are also manifested as uncertainties in radial peculiar velocities. We generate 100 error analysis catalogues of each mock with distance perturbed by a constant Gaussian variance, which is about 20% (e.g. Masters et al., 2006; Springob et al., 2007; Tully et al., 2013); however, this uncertainty is non–Gaussian, since it originates from the uncertainty of the distance modulus. Thus, we simulate the measurement error by generating a set of 100 versions of each mock catalogue with distance moduli perturbed with a constant Gaussian variance $\sigma = 0.43$, which roughly corresponds to $\sim 20\%$ distance error. The perturbed distances are used to calculate new velocities using the unbiased method described in Watkins & Feldman (2015b) so that the errors in the velocities are Gaussian distributed. The uncertainties in the correlation function due to measurement errors are estimated by averaging the standard deviations of the correlations calculated from the perturbed data sets. In Fig. 3.4 we show the results of perturbing a single CF2-galaxy catalogue in this way. From the figure it is evident that measurement errors affect our results much less than cosmic variance (see also Fig. 3.5).

### 3.4.3 Measurement Error and Sample Size

Once we have a large enough sample size to adequately probe a volume, we do not expect cosmic variance to change with sample size, since in this case it is due to the variations between volumes of a similar size. To decrease the cosmic variance we would need to increase the depth of our sample; larger volumes should vary less as we approach the scale of homogeneity for the Universe.

In contrast, we can reduce the effect of measurement errors by increasing our sample size, even if the volume being probed stays the same. To characterize the effect of sample size on measurement errors, we select new mock surveys with up to $20,000$ galaxies by changing $\mathscr{A}$ in Eq. (3.11) while leaving the other selection function parameters unchanged. We then perturb them

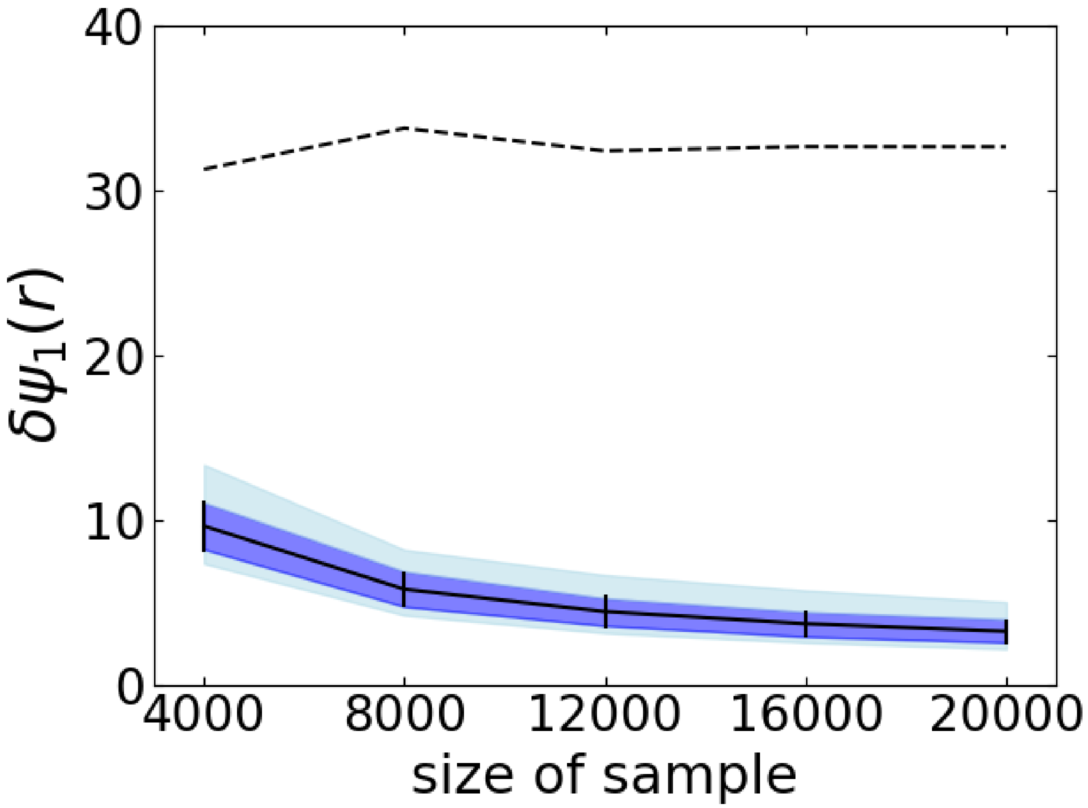

Figure 3.5: The dashed line shows the standard deviation of the cosmic variance of the correlation statistic $\psi_1$ at the redshift separation bin 0 - 500 km $s^{-1}$ of the simulation catalogues as a function of sample size. The solid line indicates measurement error of the perturbed sample averaged over all the bins as a function of sample size, in units of 1000 $km^2$ $s^{-2}$. The contours show the 68% and 95% ranges of the results, whereas the error bars are the standard deviations of the measurement errors.

using the same method described in section 3.4.2. In Fig. 3.5 we show how the cosmic variance and measurement errors of the correlation statistic $\psi_1$ changes with sample size. Increasing the sample size reduces the statistical errors significantly, while, as expected, the cosmic variance doesn't show significant difference.

## 3.5 Correlation Results

Fig. 3.5 shows the relationship between sample size and statistical error. Using this relation, we can calculate the statistical error of CF3 surveys, which have many more data points than the CF2 surveys. Fig. 3.6 shows the correlation function of CF3-galaxy survey with Hubble constant $H_0 = 75$ km s$^{-1}$ Mpc$^{-1}$; this is the value given by Tully et al. (2016) as the best fit to the data. We see that the correlation function of CF3 is larger than the mean value of correlations of mock catalogs. Hellwing et al. (2017) show that cosmic variance of local group (LG) observer mock catalogs with a Virgo like cluster is larger than the Copernican observer mock catalogs without Virgo, which explains the smaller mean correlation value from mock catalogs in Fig. 3.6.

The 75 km s$^{-1}$ Mpc$^{-1}$ value for the Hubble constant is in significant tension with the larger-scale Planck Collaboration et al. (2014a) result of $67.74 \pm 0.46$ km s$^{-1}$ Mpc$^{-1}$ obtained from the cosmic background radiation. One possible source of this discrepency is an error in the calibration of the distance indicators used in the CF3 measurement. Given that distance indicators are calibrated in sequence working outward, this would most likely be an error near the base of the distance ladder; for example, with the calibration of cepheid distances (see *e.g.* Riess et al., 2016, for a discussion of this tension). However, a second possibility is that our local volume has a significant outflow which is artificially inflating the value of $H_0$. Tully et al. (2016) discuss this possibility qualitatively by assessing the size and radial profile of the outflow required to obtain different underlying values of $H_0$. Given that radial flows also impact the correlation function, we can preform a similar analysis here by varying the Hubble constant used in estimating velocities from distances in the CF3 survey.

In Fig. 3.7 we show the correlation functions assuming $H_0$ values from 70-75 km s$^{-1}$ Mpc$^{-1}$ in

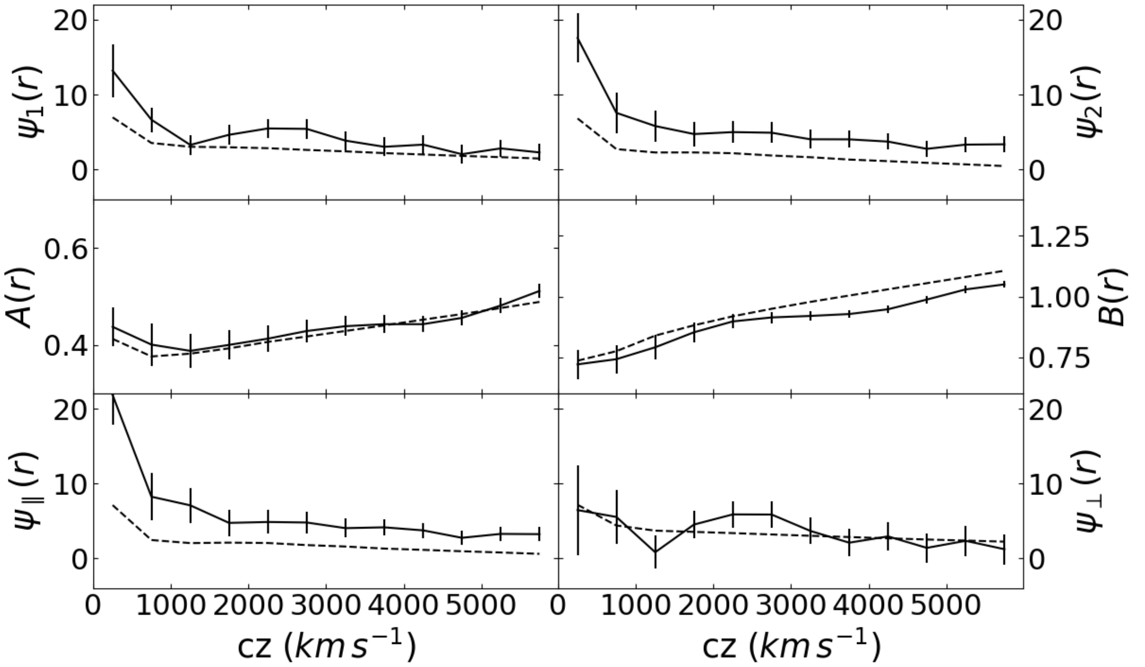

Figure 3.6: Velocity correlation functions of CF3-galaxy survey with $H = 75$km s$^{-1}$ Mpc$^{-1}$. $\psi_1$, $\psi_2$, $\psi_\parallel$ and $\psi_\perp$ are in units of (100 km s$^{-1}$)$^2$. The solid line shows the real survey result, the error bar indicates its uncertainty, combining the effects of cosmic variance and measurement error. The dashed line indicates the average of 100 mock catalogues.

the top panel and 75-80 km s$^{-1}$ Mpc$^{-1}$ in the bottom panel. As can be seen, even small deviations from the value of 75 km s$^{-1}$ Mpc$^{-1}$ can lead to unrealistically large correlations on a wide range of scales. Particularly troubling is the increase in $\psi_1$ (or equivalently $\psi_\perp$) with increasing scale. This analysis confirms the conclusion of Tully et al. (2016) that it is unlikely that outflows can be the source of the discrepancy in the value of the Hubble constant between the Planck result and more local probes.

## 3.6 Linear Theory

In this section we explore the use of the correlation function to constrain cosmological models. This was previously attempted by Borgani et al. (2000); however, they incorrectly assumed that the cosmic variance in the correlation function $\psi_1$ was Gaussian distributed. We examine the implications that the cosmic variance in $\psi_1$ is, to a good approximation, Wishart distributed, as

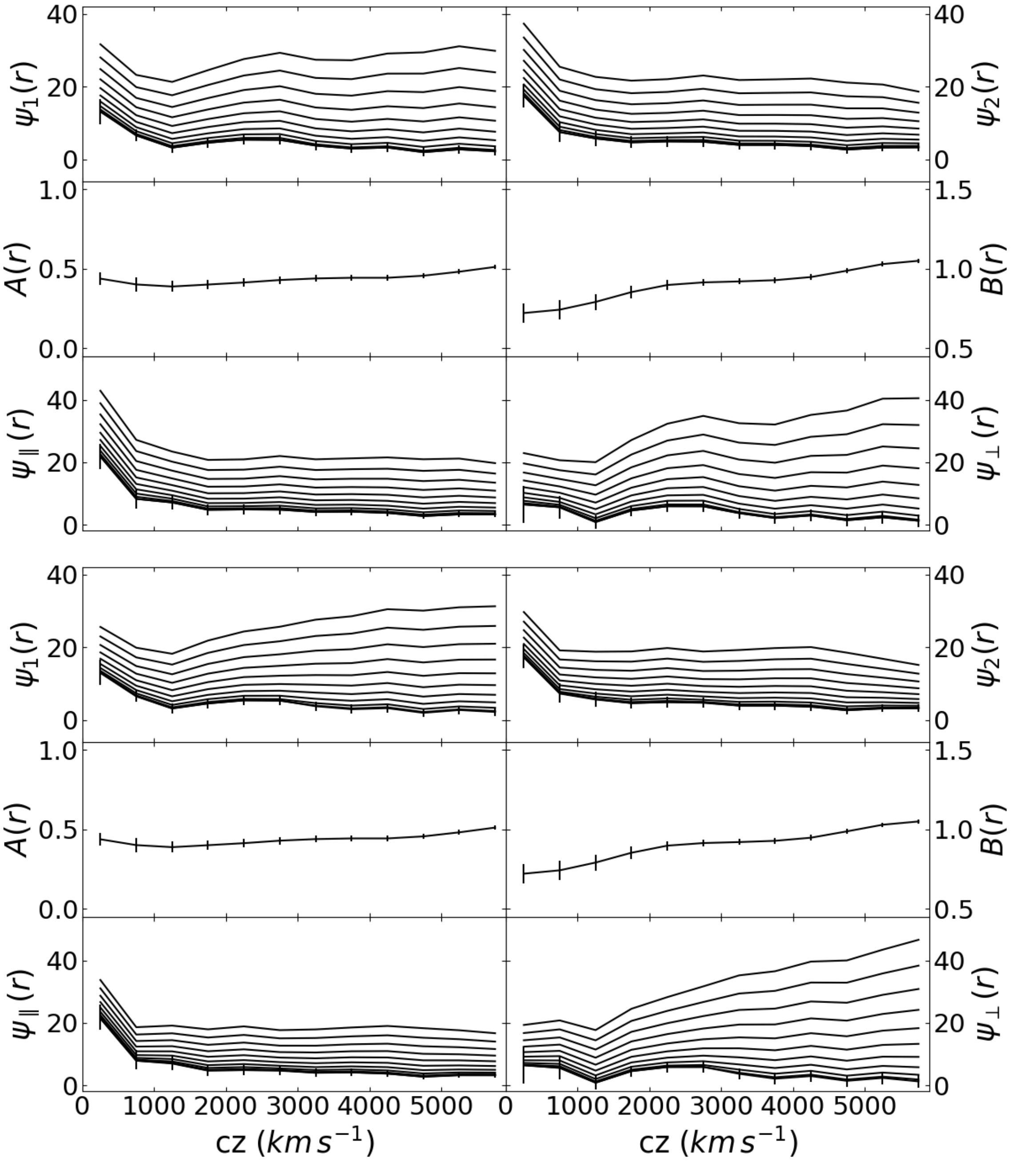

Figure 3.7: **Top Panel:** Velocity correlation functions of CF3-galaxy surveys with Hubble constant from 70 to 75 km $s^{-1}$ $Mpc^{-1}$ (top to bottom, 0.5 km $s^{-1}$ $Mpc^{-1}$ each). $\psi_1$, $\psi_2$, $\psi_\parallel$ and $\psi_\perp$ are in units of (100 km $s^{-1})^2$. The contours indicates the cosmic variance. **Bottom Panel:** Same as the top panel, but Hubble constant from 75 to 80 km $s^{-1}$ $Mpc^{-1}$ (bottom to top, 0.5 km $s^{-1}$ $Mpc^{-1}$ each).

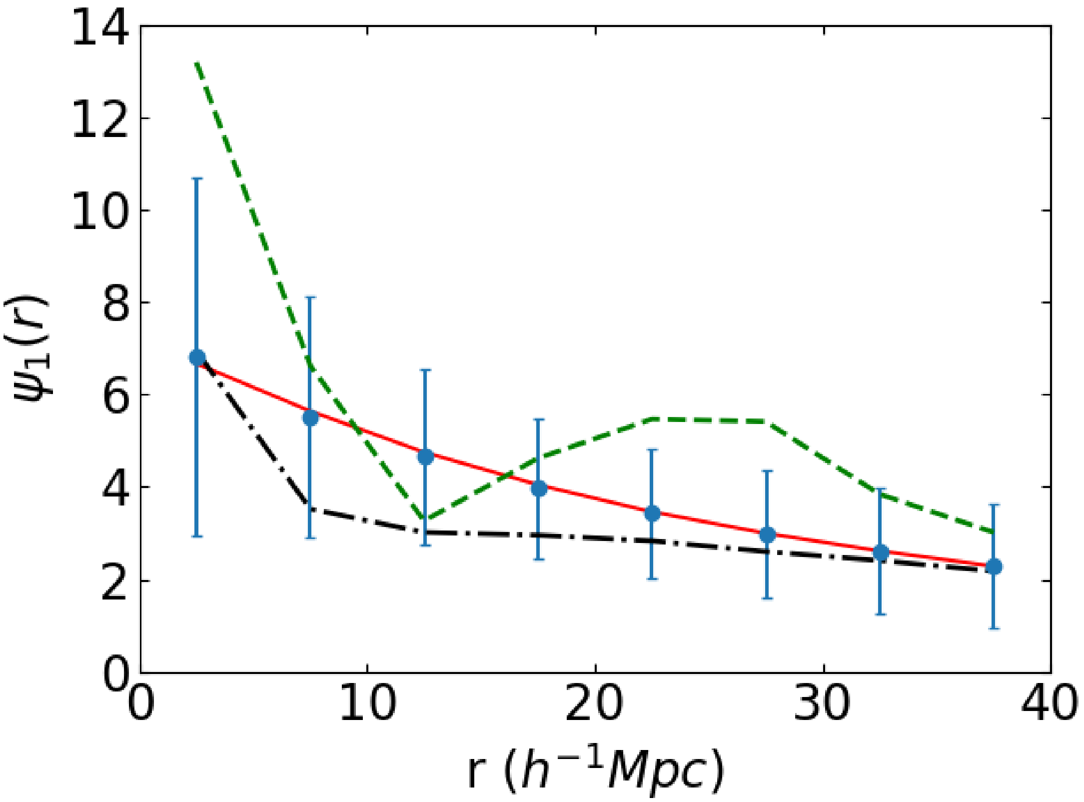

Figure 3.8: $\psi_1$ values of CF3-galaxy catalogue, mock catalogues and linear theory predictions, in units of (100 km $s^{-1}$)$^2$. The blue dots show the mean of 100 mock catalogues using distance separation, the black dash dotted line shows the mean of the mock catalogues using redshift separation, the red solid line indicates the linear theory prediction, and the green dashed line shows the CF3-galaxy correlation value using redshift separation. The blue error bars represent the cosmic variance.

discussed in section 3.4.1.

Linear theory describes the relation between the radial and transverse correlation functions and the power spectrum of density fluctuation $P(k)$ (Borgani et al., 2000). The radial and transverse velocity correlations can be written in terms of the power spectrum as follows:

$$\psi_{\|}(r) = \frac{\beta^2 H_0^2}{2\pi^2}\int P(k)\left[j_0(kr)-2\frac{j_1(kr)}{kr}\right]dk, \tag{3.12}$$

$$\psi_{\perp}(r) = \frac{\beta^2 H_0^2}{2\pi^2}\int P(k)\frac{j_1(kr)}{kr}dk, \tag{3.13}$$

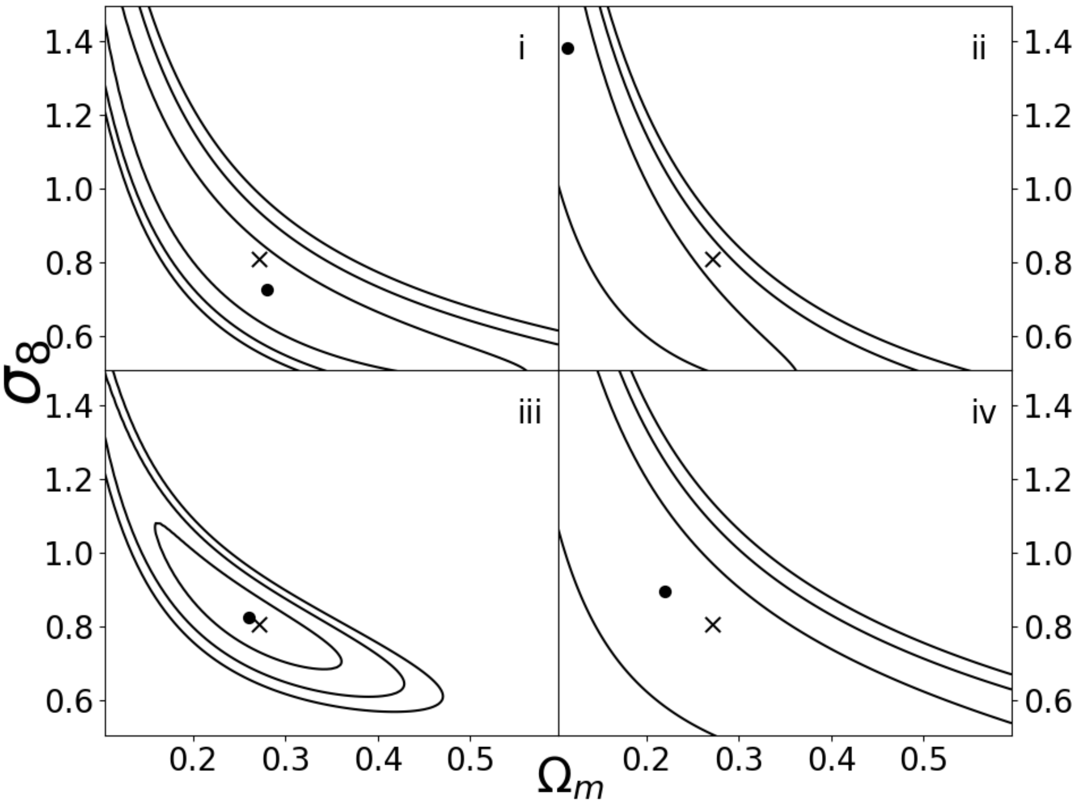

Figure 3.9: $\chi^2$ plots of four weighting schemes of mock catalogue correlations in redshift and linear theory predictions truncated at 4000 km s$^{-1}$ with 500 km s$^{-1}$ binwidth. The minimum $\chi^2$ value has been subtracted from each cell. The dot indicates the best $\chi^2$ fitting, and the contours show 68% and 95% and 99.9% likelihood of $\chi^2$ values. The cross indicates the value of the Millennium simulation (Table 3.1).

where $j_i(kr)$ is the i$^{\text{th}}$-order spherical Bessel function, $P(k)$ is the power spectrum, and on large scales $\beta = f(\Omega_m)\sigma_8$ (Guzzo et al., 2008; Turnbull et al., 2012), $f(\Omega_m) = \Omega_m^{0.55}$ (Linder, 2005) and $\sigma_8$, is the amplitude of density fluctuations on a scale of $8h^{-1}$Mpc. For $P(k)$ we use the parametrization of Eisenstein & Hu (1998), that expresses $P(k)$ in terms of the matter density $\Omega_m$, the baryon density $\Omega_b$, and the Hubble parameter $h$. We normalize the power spectrum using the value of $\sigma_8$. We checked that $P(k)$ obtained from this parametrization is in good agreement with those produced by more sophisticated methods, such as Heitmann et al. (2010, 2014); Agarwal et al. (2012a, 2014).

Linear theory reproduces the average correlation functions from the mock catalogues quite well if true distances are used to specify positions rather than redshift. In Fig 3.8 we show $\psi_1$

obtained from linear theory using the simulation cosmological parameters from Table 3.1 together with the mean $\overline{\psi_1}$ from the mock catalogues. We used the average $A$ and $B$ functions from the mock catalogues to go from the linear theory $\psi_{\parallel}$ and $\psi_{\perp}$ to $\psi_1$ via Eq. 3.5. We see that linear theory prediction matches the averages of the mock catalogues well when using distance separation. However, when redshift is used to specify distance, we see the effects of redshift distortion, although even in this case the effects are smaller than the cosmic variance. Redshift distortions also affect the estimation of cosmological parameters and we discuss their inclusion below.

The velocity correlation functions measured using the CF3 catalogues are within the cosmic variance of those using mock catalogues from the simulations, which in turn use initial conditions close to those parameters measured by seven-year Wilkinson Microwave Anisotropy Probe (WMAP Larson et al., 2011, see also Table 3.1). Thus the CF3 correlation function appears to agree with the cosmological standard model. We can make this assessment more quantitative by developing a $\chi^2$ statistic for the difference between the measured correlation function and the prediction from linear theory. This analysis results in constraints on $\Omega_m$ and $\sigma_8$, which are the main factors that determine the shape and amplitude of the power spectrum, respectively. In addition, $\chi^2$ analysis is complicated by the fact that the values of $\psi_1$ in different bins are strongly correlated, since the large-scale velocity modes lead to correlations that contribute similarly to all separations. In order to account for this correlation, we use the weighted $\chi^2$ fitting method first introduced by Kaiser (1989):

$$\chi^2 = \sum_i w(r_i) \left[\psi_1^M(r_i) - \psi_1^L(r_i)\right]^2 , \tag{3.14}$$

where $w$ is the weighting function, $\psi_1^M$ is the measured value from the catalogue (CF2 or CF3), $\psi_1^L$ is the linear prediction.

The $\chi^2$ fitting is strongly affected by the errors of velocity correlation functions: the cosmic variance, the redshift distortion, and the measurement error, which is small enough to be negligible. In order to explore the effects of the complicated error distributions, we choose four different weighting schemes and test them with mock catalogues: *i*) Linear prediction weight $w(r) = 1/\psi_1^L(r)$; *ii*) Cosmic variance based weight using covariance matrix (Borgani et al., 2000);

*iii*) redshift distortion based weight using the redshift distortion matrix, which can be regarded as an error correlated matrix; *iv*) Combination of error and redshift distortion based weight using the sum of the covariance matrix and redshift distortion matrix, which leads to a full covariance matrix (Blobel, 2003; D'Agostini, 1995).

Eq. 3.15 - 3.18 below show the four weighting schemes, where $C$ is the covariance matrix; $\lambda$ is the redshift distortion matrix; $N_{mock}$ is the number of mock catalogues; $\psi^{i}_{1,l}$ is the correlation value of the $i^{th}$ separation bin of the $l^{th}$ mock catalogue; $\overline{\psi}^{i}_{1}$ is the average value of $N_{mock}$ catalogues in the $i$th separation bin; $\psi^{i,s}_{1,l}$ ($\psi^{i,r}_{1,l}$) is the correlation value of the $i^{th}$ bin of the $l^{th}$ mock catalogue using redshift (distance) separation.

$$i).\ \chi^2 = \sum_i \frac{\left[\psi^M_1(r_i) - \psi^L_1(r_i)\right]^2}{\psi^L_1(r_i)} \tag{3.15}$$

$$ii).\ \chi^2 = \sum_{i,j} \left[\psi^M_1(r_i) - \psi^L_1(r_i)\right] C^{-1}_{ij} \left[\psi^M_1(r_j) - \psi^L_1(r_j)\right] \quad C_{ij} = \frac{1}{N_{mock}} \sum_{l=1}^{N_{mock}} \left(\psi^{i}_{1,l} - \overline{\psi}^{i}_{1}\right)\left(\psi^{j}_{1,l} - \overline{\psi}^{j}_{1}\right) \tag{3.16}$$

$$iii).\ \chi^2 = \sum_{i,j} \left[\psi^M_1(r_i) - \psi^L_1(r_i)\right] \lambda^{-1}_{ij} \left[\psi^M_1(r_j) - \psi^L_1(r_j)\right] \quad \lambda_{ij} = \frac{1}{N_{mock}} \sum_{l=1}^{N_{mock}} \left(\psi^{i,s}_{1,l} - \psi^{i,r}_{1,l}\right)\left(\psi^{j,s}_{1,l} - \psi^{j,r}_{1,l}\right) \tag{3.17}$$

$$iv).\ \chi^2 = \sum_{i,j} \left[\psi^M_1(r_i) - \psi^L_1(r_i)\right] \left(C_{ij} + \lambda_{ij}\right)^{-1} \left[\psi^M_1(r_j) - \psi^L_1(r_j)\right] \tag{3.18}$$

In Fig. 3.9, we show the $\chi^2$ estimates of the mock catalogue correlations and the estimates for the parameters $\Omega_m$ (x-axis) and $\sigma_8$ (y-axis) for each of the weighting schemes. (The 68% and 95% contours are defined by the same method used in Borgani et al. (2000).)

*i)* Linear prediction weighted scheme (Eq. 3.15) gives a reasonable though not very tight constraint, especially for $\Omega_m$, it is somewhat sensitive to the truncation of the correlation functions. Note that this method treats the bins as independent from each other, and thus does not incorporate the strong correlations among different bins.

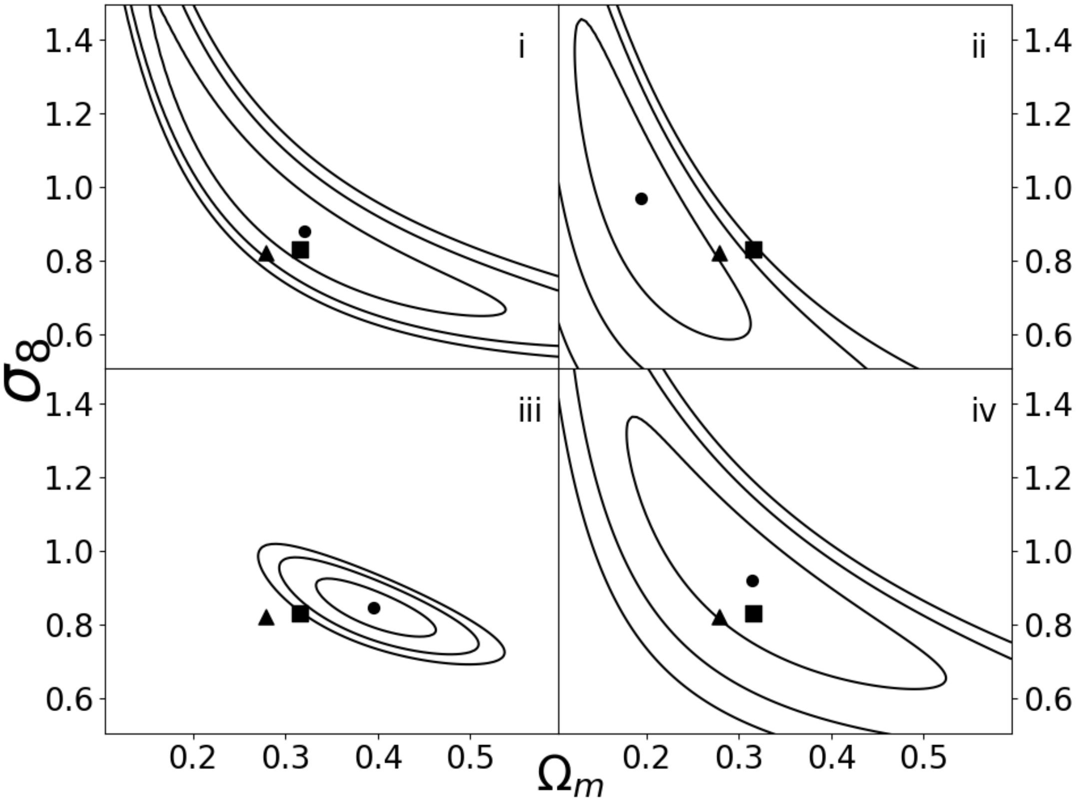

Figure 3.10: Same as Fig. 3.9, but using CF3-galaxy correlations. The triangle is the WMAP result (Bennett et al., 2013) and the square is the Planck result (Planck Collaboration et al., 2014a).

*ii)* Covariance matrix weighted scheme (Eq. 3.16) does not provide strong constraints. That is because the covariance matrix is dominated by cosmic variance which is decreasing for increasing separation, and thus larger separations are given more weight in the $\chi^2$ fitting scheme. Furthermore, the non-Gaussian skewness also becomes more pronounced in large separation bins (see Sec. 3.4.1) and thus biases the results. In addition, the Wishart error distribution is sensitive to different mock selections. Comparing the Millennium and MDLP2 mock catalogs with and without the angular mask, we found that the simulation mock catalogs effect the covariance matrix estimates since the covariance matrix weighted scheme is sensitively dependent on the Wishart distribution parameters for the determination of cosmic variance (see Sec. 3.4.1). However, differences caused by the different simulation mock catalogs do not show any trend of improving the constraints, instead, they are somewhat random. Non–Gaussian skewness is the dominant source of bias for the covariance matrix weighted scheme.

*iii)* Redshift distortion weighted scheme (Eq. 3.17) provides a good estimate of the parameters while using mock catalogues only and the contours are more compacted than other schemes.

*iv)* We combine the effects of cosmic variance and redshift distortion. The constraining result of combined weighting scheme is not as tight as methods *i* and *iii*, but it does agree with the simulation parameters within $1\sigma$.

Fig. 3.10 shows the constraints using the CF3-galaxy. The redshift distortion scheme by itself shows very tight contours, but disagrees with the Planck and WMAP results at a high confidence limit, which leads us to conclude that the simulation redshift distortions do not mimic the distortions in the CF3 catalogue well. In addition, the schemes become more sensitive to truncations when using real survey. Figs. 3.11 and 3.12 show the $\Omega_m$ and $\sigma_8$ results of the four weighting schemes with different truncations. The redshift distortion weighted scheme (*iii*) is more strongly dependent on the truncation choice but mostly agrees within two standard deviations, whereas the others agree within one standard deviation.

Considering the performances of those four weighting schemes for the simulation and observation data, we choose the scheme *iv* that combines the cosmic variance and redshift distortion

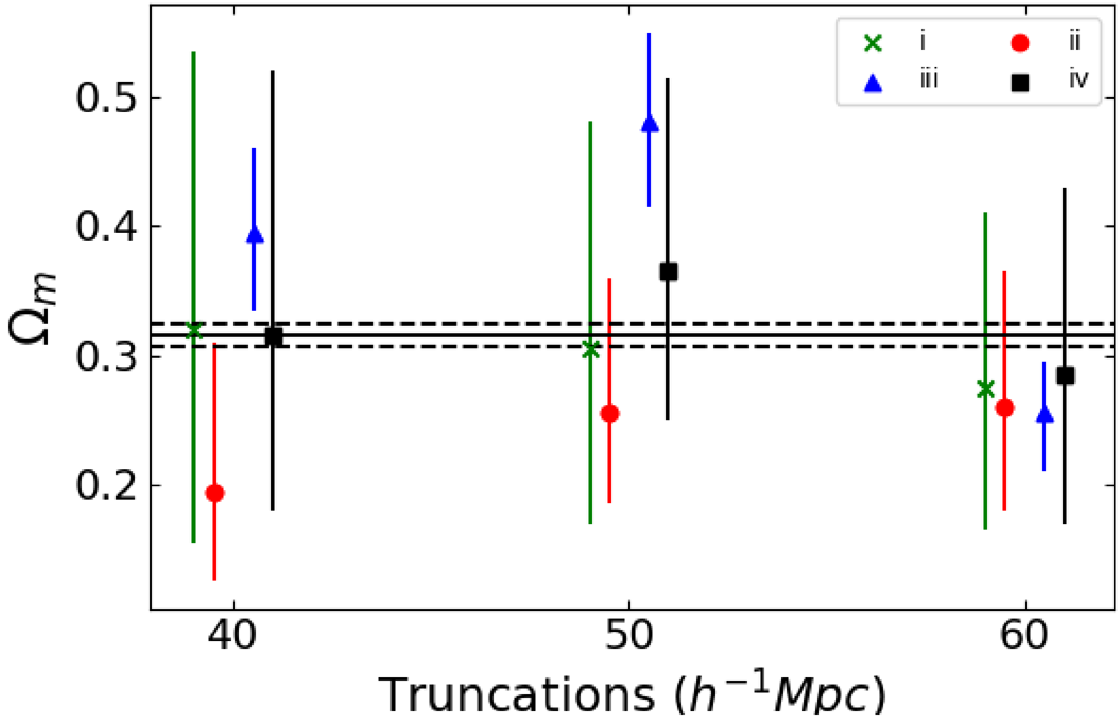

Figure 3.11: The effect truncation has on the estimation of $\Omega_m$. the green cross markers show the constrains using the linear prediction weighted scheme ($i$), the red circle markers show the results using covariance matrix weighted scheme ($ii$), the blue triangle markers indicate the results using redshift distortion weighted scheme($iii$) and black square indicate the results using the combo weighting scheme ($iv$). The horizontal black lines are the $\Omega_m$ value and $1\sigma$ determined by Planck.

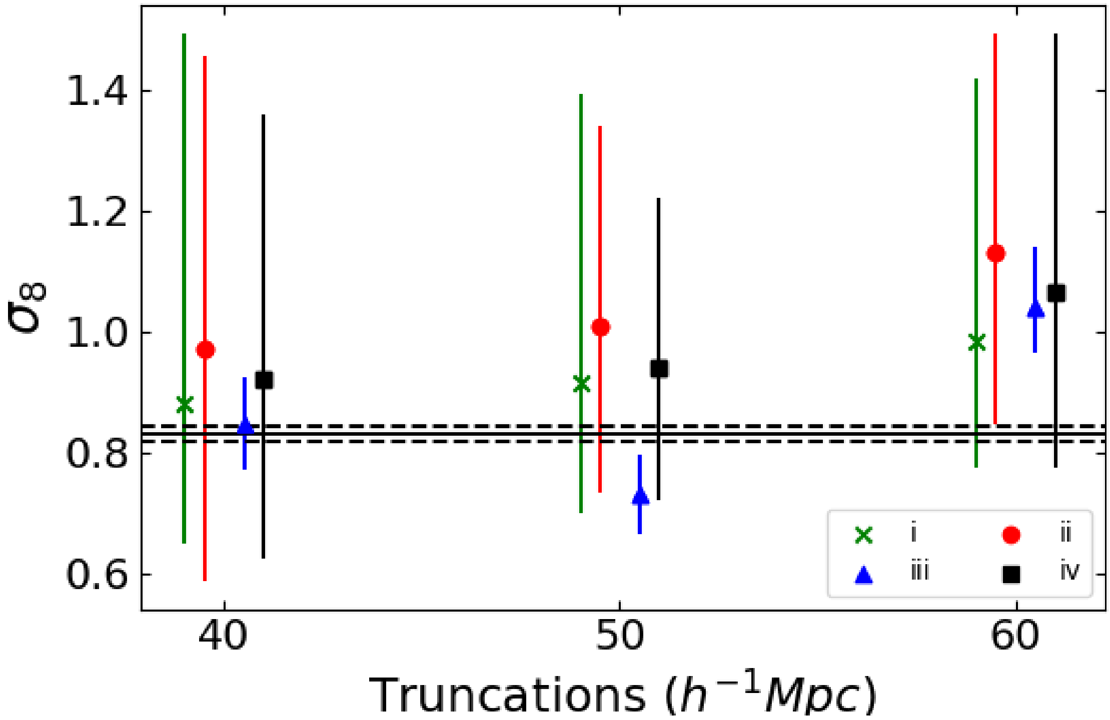

Figure 3.12: Same as Fig. 3.11, but showing the $\sigma_8$ truncation results.

effects in this chapter to be most reliable. In Fig. 3.13, we show the $\chi^2$ of CF3-galaxy correlations using the redshift distortions and cosmic variance combination scheme (Eq. 3.18). We get $\Omega_m = 0.315^{+0.205}_{-0.135}$ and $\sigma_8 = 0.92^{+0.440}_{-0.295}$. As can be seen, the value of $\Omega_m$ and $\sigma_8$ agree with the results from Planck ($\Omega_m = 0.315 \pm 0.013$; $\sigma_8 = 0.831 \pm 0.013$, Planck Collaboration et al., 2014a) and WMAP9 ($\Omega_m = 0.279 \pm 0.023$; $\sigma_8 = 0.821 \pm 0.023$ Bennett et al., 2013), whereas the value of $\sigma_8$ we get from the correlation analysis with CF3 is slightly larger but still within $1\sigma$.

Part of the discrepancy in $\sigma_8$ could be due to the fact that in the present analysis $\sigma_8$ is obtained from local data. As was clearly shown in Juszkiewicz et al. (2010), estimators that probe the value of $\sigma_8$ on small cosmological scales do not take into account the nonlinear evolution of the parameter at late times. Using the parametrization from Juszkiewicz et al. (2010), we should compare our $\sigma_8$ results to 0.888 (Planck) and 0.879 (WMAP9) which agree to within $\sim 1\sigma$.

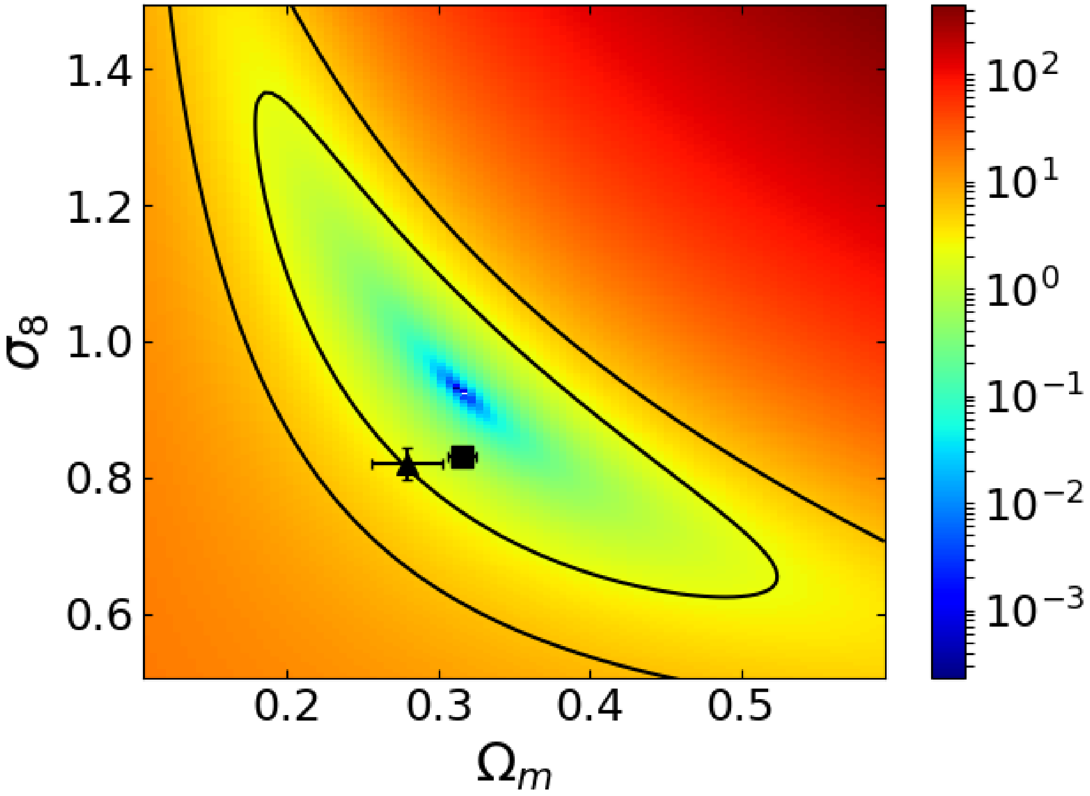

Figure 3.13: $\chi^2$ plot for the CF3-galaxy survey with combo weighting scheme for binwidth equals 500 km s$^{-1}$ and truncation at 4000 km s$^{-1}$. The minimum $\chi^2$ value has been subtracted from each cell. The contours indicate 68% and 95% likelihood of $\chi^2$ values. The square marker indicates the best value from Planck (Planck Collaboration et al., 2014a), whereas the triangle marker is the value of WMAP9 (Bennett et al., 2013).

## 3.7 Conclusion

In principle, the velocity Correlation Function is a powerful statistical tool in exploring the Peculiar Velocity Field and through that, the mass distribution on cosmological scales. We have shown that on average the correlation function calculated from simulated catalogues recovers the expected signal from linear theory, thus demonstrating that it is an unbiased statistic. Since the statistical error in the correlation function is significantly smaller than the cosmic variance, the velocity correlation function does a reasonable job dealing with the large uncertainty inherent in the determination of peculiar velocities of galaxies and groups. However, the non-Gaussian nature of the cosmic variance and redshift distortion put limits on how well we can use this statistic to constrain cosmological parameters.

We have calculated the velocity correlation functions for the CosmicFlows-2 and CosmicFlows-3 catalogues and shown that they are consistent with expectations from the standard cosmological model. In addition, we have used our results together with linear theory to constrain the cosmological parameter $\Omega_m$ and $\sigma_8$. In constraining the cosmological parameters, we have assumed Gaussian distributed errors, while the simulations have clearly shown that the error distribution of the cosmic variance has distinct non-Gaussian tails. Furthermore, since the cosmic variance is smaller at larger separations, the covariance matrix gives more weight at larger separations, where skewness is most pronounced and thus, may introduce systematic biased parameter estimations. In addition, redshift distortions give rise to the mismatch between CosmicFlows correlations and linear predictions and thus may contribute further bias to parameter constrains. To mitigate this effect, we have used a weighting scheme that combines the effects of cosmic variance and redshift distortion, which appears to be both more stable and less biased. Future studies that account for the non-Gaussian distribution of cosmic variance may result in more robust constraints, particularly with regard to uncertainties in parameter estimation.

The systematically larger velocity correlations observed in this study, especially in closer bins, using both the CosmicFlows-2 and and CosmicFlows-3 compilations is consistent with the observed bulk flows from these and other catalogues that is on the larger end of the expected range given the predictions from the $\Lambda$CDM model with CMB derived parameters. However, this excess may also arise from local inhomogeneities in our local volume.

## 3.8 Acknowledgements

The CosmoSim database used in this chapter is a service by the Leibniz-Institute for Astrophysics Potsdam (AIP). The MultiDark database was developed in cooperation with the Spanish MultiDark Consolider Project CSD2009-00064.

The authors gratefully acknowledge the Gauss Centre for Supercomputing e.V. (www.gauss-centre.eu) and the Partnership for Advanced Supercomputing in Europe (PRACE, www.prace-ri.eu) for funding the MultiDark simulation project by providing computing time on the GCS Supercomputer SuperMUC at Leibniz Supercomputing Centre (LRZ, www.lrz.de). The Bolshoi simulations have been performed within the Bolshoi project of the University of California High-Performance AstroComputing Center (UC-HiPACC) and were run at the NASA Ames Research Center.

# Chapter 4

# Improved Methods for Estimating Peculiar Velocity Correlation Functions Using Volume Weighting

In this chapter, we present a feasible solution for the problems mentioned in Chapter 3. In this chapter, we investigate an improved method for calculating the parallel and perpendicular velocity correlation functions directly from peculiar velocity surveys using maximum-likelihood estimators. A central feature of our method is the use of position-dependent weighting in order to reduce the influence of nearby galaxies, which are typically overrepresented relative to more distant galaxies that occupy the volume of most surveys. We demonstrate that the correlation functions calculated in this way are less susceptible to bias due to our particular location in the Universe, and thus are easily comparable with linear theory and between surveys. Our results suggest that the parallel velocity correlation function is a promising cosmological probe, given that it provides a better approximation of a Gaussian distribution than other velocity correlation functions and that its bias is more easily minimized by weighting. The position weighted parallel velocity correlation function specifically provides stabler and tighter cosmological parameter constraints than other popular methods (*e.g.*, Gorski $\psi_1$ correlation function). The results in the chapter were first discussed in Wang et al. 2020, collaborated with Sarah Peery, Hume A. Feldman and Richard Watkins (will be submitted soon).

## 4.1 Introduction

Studies of density perturbations provide information used to analyze the large scale structure of the Universe. However, density perturbation studies based on redshift galaxy distributions are limited by the bias due to peculiar velocities, also known as redshift space distortion (RSD). Many studies have shown the effects of peculiar velocities in RSD studies (e.g. Kaiser, 1987; Thomas et al., 2004; Scoccimarro, 2004; Taruya et al., 2010; Reid & White, 2011; Seljak & McDonald, 2011; Zhang et al., 2013; Zheng et al., 2013; Song et al., 2013; Taruya et al., 2013; Senatore & Zaldarriaga, 2014; Uhlemann & Kopp, 2015; Okumura et al., 2015; Vlah et al., 2016; Bianchi et al., 2016; Hand et al., 2017; Bel et al., 2018).

Peculiar velocity is a powerful tracer of mass distribution (e.g. Watkins et al., 2009; Feldman et al., 2010; Davis et al., 2011; Nusser et al., 2011; Macaulay et al., 2011; Turnbull et al., 2012; Macaulay et al., 2012; Nusser, 2014; Springob et al., 2014a; Johnson et al., 2014; Scrimgeour et al., 2016a). However, current peculiar velocity measurements are still based on radial distances, which limit the precision of peculiar velocity surveys. A different method of measuring the peculiar velocity can be made using the kinematic Sunyaev-Zel'dovich effect (e.g. Sunyaev & Zeldovich, 1980; Dolag et al., 2005; Kashlinsky et al., 2008; Hand et al., 2012; Dolag et al., 2016; Planck Collaboration et al., 2016a, 2018c). However, due to the signal weakness, it is a very difficult measurement. Therefore, ensemble statistics of peculiar velocities is more practical for current studies (e.g. Kaiser, 1988; Ferreira et al., 1999; Juszkiewicz et al., 2000; Feldman et al., 2003; Watkins & Feldman, 2007; Watkins et al., 2009; Feldman et al., 2010; Davis et al., 2011; Agarwal et al., 2012b; Abate & Feldman, 2012; Hand et al., 2012; Nusser, 2014; Hellwing, 2014; Planck Collaboration et al., 2016a; Kumar et al., 2015; Scrimgeour et al., 2016b,a; Seiler & Parkinson, 2016; Hoffman et al., 2016; Nusser, 2016; Hellwing et al., 2017).

The velocity correlation function analysis provides another tool to investigate the peculiar velocity field. The most widely used velocity correlation estimator was introduced by Gorski (1988) and further formulated in Gorski et al. (1989). It has revealed interesting results constraining cosmological parameter (e.g. Jaffe & Kaiser, 1995; Zaroubi et al., 1997; Juszkiewicz et al., 2000; Borgani et al., 2000; Abate & Erdoğdu, 2009; Nusser & Davis, 2011; Okumura et al., 2014; Howlett et al., 2017; Hellwing et al., 2017; Wang et al., 2018; Dupuy et al., 2019).

The velocity correlation function can be expressed as two independent functions, one for velocity components along the separation vector of a pair of galaxies and one for components perpendicular to this vector. The Gorski (1988) correlation estimator results in a complicated combination of these two functions, with the precise mixture given by selection functions that depend on the distribution of the survey objects as well as the separation distance. This estimator has the decided disadvantage of not being comparable between studies that use different survey objects. At the same time it was introduced that it was seen as being more stable than other methods given the small size of the available datasets. Given the availability of much larger peculiar velocity catalogs today, it is an opportune time to explore other methods of estimating velocity correlations. In addition, Wang et al. (2018) found that the cosmic variance of the correlation function using the Gorski estimator is large and non-Gaussian distributed, and Hellwing et al. (2017) showed that it is susceptible to biases due to our special location near a large overdensity – the Virgo Cluster. These problems make peculiar velocity correlation function estimator less than ideal as a probe of large-scale structure.

In this chapter, we use an alternative method, introduced by Kaiser (1989) and Groth et al. (1989), that estimates the parallel and perpendicular correlation functions directly in a way that is independent of the survey distribution. This method further allows for the weighting of individual velocity measurements to improve the estimator. While Groth et al. (1989) used weighting to reduce the effect of random errors, we introduce a novel weighting scheme that reduces cosmic variance and bias by increasing the effective volume probed by a survey.

The chapter is organized as follows: In section 4.2, we derive the weighted estimators for the parallel and perpendicular correlation functions. In section 4.3, we discuss the CosmicFlow-3 (CF3) catalog we analyze. In section 4.4, we introduce the N-body simulations and methods used for generating mock catalogs. In section 4.5, we show results for our method on both randomly centered mock catalogs as well as those centered in environments similar to that of the Milky Way for several different weighting schemes. We also apply our methods to obtain estimates of the parallel and perpendicular correlation functions in the local Universe using data from the CF3 catalog. In section 4.6, we discuss the parameter constraining result using the weighted estimators.

Section 4.7 concludes this chapter.

## 4.2 The Peculiar Velocity Correlation Estimator

The general form of the two-point velocity correlation tensor is

$$\Psi_{ij}(\mathbf{r}) = \langle v_i(\mathbf{r_0}) v_j(\mathbf{r_0}+\mathbf{r})\rangle, \tag{4.1}$$

where $i$ and $j$ designate the cartesian components of the velocity and the average is over points separated by the vector $\mathbf{r}$. Making the usual assumption that the velocity field is a statistically isotropic and homogeneous random field, we can write the correlation tensor in terms of two functions which depend only on the magnitude of the separation vector $r = |\mathbf{r}|$,

$$\Psi_{ij}(r) = \Psi_{\|}(r)\hat{r}_i\hat{r}_j + \Psi_{\perp}(r)\left(\delta_{ij} - \hat{r}_i\hat{r}_j\right) \tag{4.2}$$

where $\hat{r}$ is a unit vector in the direction of the separation vector. These two functions have simple physical interpretations; $\Psi_{\|}(r)$ is the (parallel) correlation of the velocity components along the separation vector and $\Psi_{\perp}(r)$ gives the (perpendicular) correlation of the components of the velocity perpendicular to the separation vector.

Our goal is to estimate $\Psi_{\|}(r)$ and $\Psi_{\perp}(r)$ from the correlations in the radial component of the peculiar velocity, $u$, which is the only component that can be measured. Given a pair of galaxies at positions $\mathbf{r_1}$ and $\mathbf{r_2}$, we can write the correlation of their radial peculiar velocities as

$$\begin{aligned} \langle u_1 u_2\rangle &= \hat{r}_{1i}\hat{r}_{2j}\langle v_i v_j\rangle \\ &= \Psi_{\|}(r)(\mathbf{\hat{r}_1}\cdot\mathbf{\hat{r}})(\mathbf{\hat{r}_2}\cdot\mathbf{\hat{r}}) \\ &+ \Psi_{\perp}(r)\left[\mathbf{\hat{r}_1}\cdot\mathbf{\hat{r}_2} - (\mathbf{\hat{r}_1}\cdot\mathbf{\hat{r}})(\mathbf{\hat{r}_2}\cdot\mathbf{\hat{r}})\right]. \end{aligned} \tag{4.3}$$

This expression can be written in terms of $\theta_1$ and $\theta_2$, the angles the separation vector $\mathbf{r}$ makes with the position vectors $\mathbf{r_1}$ and $\mathbf{r_2}$ respectively. Specifically,

$$(\hat{\mathbf{r}}_\mathbf{1} \cdot \hat{\mathbf{r}})(\hat{\mathbf{r}}_\mathbf{2} \cdot \hat{\mathbf{r}}) = \cos(\theta_1)\cos(\theta_2), \tag{4.4}$$

and

$$\hat{\mathbf{r}}_\mathbf{1} \cdot \hat{\mathbf{r}}_\mathbf{2} = \cos(\theta_2 - \theta_1) = \cos(\theta_1)\cos(\theta_2) + \sin(\theta_1)\sin(\theta_2). \tag{4.5}$$

Using these results, we can put eq. 4.3 into the simple form

$$\langle u_1 u_2 \rangle = \Psi_{\parallel}(r) f(\theta_1, \theta_2) + \Psi_{\perp}(r) g(\theta_1, \theta_2), \tag{4.6}$$

where $f = \cos(\theta_1)\cos(\theta_2)$ and $g = \sin(\theta_1)\sin(\theta_2)$.

Following Kaiser (1989) and Groth et al. (1989), we use a weighted least-squares method to estimate $\Psi_{\parallel}(r)$ and $\Psi_{\perp}(r)$ from a catalog of peculiar velocities $u_m$. We minimize the function

$$\chi^2(r) = \sum_{m,n} w_{m,n} \left[ u_m u_n - \Psi_{\parallel}(r) f(\theta_1, \theta_2) - \Psi_{\perp}(r) g(\theta_1, \theta_2) \right] \tag{4.7}$$

with respect to $\Psi_{\parallel}(r)$ and $\Psi_{\perp}(r)$, where the sum is over pairs of galaxies whose separations fall within a specified bin and $w_{i,j}$ is a weight assigned to each galaxy pair. The minimization can be done analytically, resulting in the estimates

$$\Psi_{\parallel}(r) = \frac{\sum wg^2 \sum wf u_1 u_2 - \sum wfg \sum wg u_1 u_2}{\sum wf^2 \sum wg^2 - \left(\sum wfg\right)^2}, \tag{4.8}$$

and

$$\Psi_{\perp}(r) = \frac{\sum wf^2 \sum wg u_1 u_2 - \sum wfg \sum wf u_1 u_2}{\sum wf^2 \sum wg^2 - \left(\sum wfg\right)^2}, \tag{4.9}$$

where the sums are over galaxy pairs whose separations lie in a bin centered on $r$.

An alternative approach to studying peculiar velocity correlations is to use the $\psi_1$ and $\psi_2$ statistics introduced by Gorski et al. (1989) and utilized in several subsequent studies (e.g. Borgani et al., 2000; Hellwing et al., 2017; Wang et al., 2018). While these statistics in principle carry the same information as $\Psi_{||}$ and $\Psi_{\perp}$, in practice they depend on the particular distribution of objects in a survey, making them not comparable between surveys. While in the past there was some motivation to focus on $\psi_1$ as being particularly stable when applied to the small datasets available at the time, there is now sufficient data to estimate $\Psi_{||}$ and $\Psi_{\perp}$ directly. It is possible to calculate $\Psi_{||}$ and $\Psi_{\perp}$ from $\psi_1$ and $\psi_2$ given the positions of the survey objects (see e.g. Wang et al., 2018); however, this process can be shown to be mathematically equivalent to the calculations shown in Eqs. 4.8 and 4.9.

It is not obvious how best to choose weights to use in Eqs. 4.7, 4.8 and 4.9. Kaiser (1989) used the simplest choice, $w = 1$, while Groth et al. (1989) chose weights with an eye towards reducing the effects of measurement errors. However, previous work (Wang et al., 2018) has shown that, for the surveys we will be working with, statistical errors are small compared to the effects of cosmic variance, since we calculate the correlation function in a volume that is smaller than the scale of homogeneity. This problem is exacerbated by the radial distribution of galaxies in a typical survey; the concentration of galaxies and clusters at small distances puts greater emphasis on the nearby volume, so that the effective volume reflected in the correlation function can be significantly smaller than that of the survey. This effect increases the cosmic variance and may also lead to bias. Here we will weight the pairs in order to better “balance" the survey, so that it has a larger effective volume and hence smaller cosmic variance and bias but may lead to larger statistical errors.

Our approach will be to weight pairs of galaxies by the factor $w = (r_1 r_2)^p$, where $r_1$ and $r_2$ are the positions of the galaxies and $p$ is a positive power. This scheme gives less weight to pairs of nearby galaxies, which are overrepresented in the sample, and greater weight to pairs of more distant galaxies, which are underrepresented. Correlation functions calculated using this weighting should thus reflect a more even sampling of the volume, and hence reflect a larger effective volume. However, in giving greater weight to galaxies that are far away, and hence have larger peculiar velocity uncertainties, our weighting scheme will necessarily increase statistical errors. We will explore several different choices for the power $p$ in order to determine which value provides the best overall statistic for the data we are working with.

When analyzing data from simulations, we have access to all three components of the peculiar velocity. In this case we can calculate $\Psi_{\|}$ and $\Psi_{\perp}$ directly by taking a weighted average of products of velocity components parallel and perpendicular to the separation vector for each pair, namely

$$\Psi_{\|}^{3D}(r) = \sum_{pairs} w\,(v_1 \cdot r)\,(v_2 \cdot r) \,/\, \sum_{pairs} w \tag{4.10}$$

and

$$\Psi_{\perp}^{3D} = \frac{1}{2} \sum_{pairs} w\,[(v_1 \cdot v_2) - (v_1 \cdot r)\,(v_2 \cdot r)] \,/\, \sum_{pairs} w \tag{4.11}$$

where $\mathbf{r} = \mathbf{r_2} - \mathbf{r_1}$.

In linear theory, $\Psi_{\|}$ and $\Psi_{\perp}$ can be related directly to the power spectrum of density fluctuations $P(k)$ (Eisenstein & Hu, 1998) through the relations

$$\Psi_{\|}(r) = \frac{(\sigma_8 f H_0)^2}{2\pi^2 \sigma^2(8)} \int P(k) \left[ j_0(kr) - 2\frac{j_1(kr)}{kr} \right] dk, \tag{4.12}$$

$$\Psi_{\perp}(r) = \frac{(\sigma_8 f H_0)^2}{2\pi^2 \sigma^2(8)} \int P(k) \frac{j_1(kr)}{kr} dk, \tag{4.13}$$

where $f = \Omega_m^{0.55}$ (Linder, 2005), $H_0$ is the Hubble constant, $j_n(x)$ are the spherical Bessel functions, $\sigma_8$ is the amplitude of density fluctuations on a scale of 8 $h^{-1}$Mpc. In the equations, $\sigma_8$ is the value from the simulation we use (see Section 4.4) and the $\sigma(8)$ is calculated following the method in Eisenstein & Hu (1998).

## 4.3 Data

The CosmicFlow-3 (CF3) peculiar velocity compilation (Tully et al., 2016) includes two catalogs: the galaxy catalog and the group catalog. The CF3-galaxy catalog contains 17,669 galaxies, including all the 8,135 CosmicFlow-2 (CF2) (Tully et al., 2013) galaxy distances, which is assembled by a compilation of Type Ia Supernovae (SNIa) (Tonry et al., 2003), Spiral Galaxy Clusters (SC) TF clusters (Giovanelli et al., 1998; Dale et al., 1999), Streaming Motions of Abell Clusters (SMAC)

FP clusters (Hudson et al., 1999, 2004), Early-type Far Galaxies (EFAR) FP clusters (Colless et al., 2001), TF clusters (Willick, 1999), the SFI++ catalog (Masters et al., 2006; Springob et al., 2007, 2009), group SFI++ catalog (Springob et al., 2009), Early-type Nearby Galaxies (ENEAR) survey (da Costa et al., 2000; Bernardi et al., 2002; Wegner et al., 2003), and a surface brightness fluctuations (SBF) survey (Tonry et al., 2001), together with 2,257 distances derived from the correlation between galaxy rotation and luminosity with photometry at $3.6\mu m$ obtained with Spitzer Space Telescope and 8,885 distances based on the Fundamental Plane sample derived from the Six Degree Field Galaxy Survey (6dFGS) (Springob et al., 2014b). The CF3-group catalog contains 11,878 groups and galaxies, where galaxies in known groups have had their distance moduli and redshifts averaged, resulting in a single velocity and position for the group as a whole. In the following analysis we use the CF3-galaxy catalog.

The peculiar velocities of the CF3 are calculated through the unbiased peculiar velocity estimator introduced by Watkins & Feldman (2015a):

$$v = cz \log\left(\frac{cz}{H_0 r}\right). \tag{4.14}$$

The redshift ($cz$) and distance ($r$) are provided by the CF3 survey, however, the choice of the value of Hubble constant will affect the peculiar velocity and therefore affect the velocity correlation result. Wang et al. (2018) discussed the effect of the Hubble constant on the Gorski (1988) correlation functions. For this study we will set the Hubble constant equal to 75 km $\mathrm{s}^{-1}$ $\mathrm{Mpc}^{-1}$ for the peculiar velocities of CF3 survey, the value that minimizes the magnitude of radial flows.

Due to the large uncertainties in the measurement of distance, previous studies of the velocity correlation functions (e.g. Gorski, 1988; Borgani et al., 2000; Wang et al., 2018) used redshift to determine positions of objects and hence the separations between them. In this chapter we will also use redshifts to determine positions of the objects in our catalog, using distance estimates only in our calculation of peculiar velocities.

## 4.4 Mock Catalogs

The mock catalogs we use in this chapter are generated from halo catalogs of the OuterRim Simulation (Habib et al., 2016; Heitmann et al., 2019a,b), which is carried out from the Mira-Titan Universe Simulations. The OuterRim simulation is a dark matter only simulation with cosmological parameters similar to the WMAP-7 (Larson et al., 2011) cosmology, which are shown in Table 4.1.

Table 4.1: The cosmological parameters of the OuterRim Simulation

| | |
|---|---|
| Matter density, $\Omega_m$ | 0.2648 |
| Cosmological constant density, $\Omega_\Lambda$ | 0.7352 |
| Baryon density, $\Omega_b$ | 0.0448 |
| Hubble parameter, $h$ (100 km s$^{-1}$ Mpc$^{-1}$) | 0.71 |
| Amplitude of matter density fluctuations, $\sigma_8$ | 0.8 |
| Primordial scalar spectral index, $n_s$ | 0.963 |
| Box size ($h^{-1}$Mpc) | 3,000 |
| Number of particles | $10,240^3$ |
| Particle mass, $m_p$ ($10^9 h^{-1} M_\odot$) | 1.85 |
| Softening, $f_c$ ($h^{-1}$kpc) | 3 |

The simulation contains halos in a very large range that covers galaxies, groups, and clusters. We use halos in mass range [$10^{11}$, $10^{13}$]$M_\odot$ as galaxies to generate mock catalogs for CF3-galaxy survey. Figure 4.1 shows the redshift distribution of the CF3-galaxy catalog and an example of one mock catalog.

We generated 100 versions each of two types of mock catalogs differing in how their halo center points are chosen. The first type, which we call “random" mock catalogs, are centered on randomly chosen halos inside the Gpc$^3$ region of the simulation. The second type, called Local Group (LG) mock catalogs, are centered on a Milky Way-like halo ($M = [13.5 \pm 6.5] \times 10^{11} h^{-1} M_\odot$]) with a Virgo-like cluster at a similar distance of the Virgo Cluster from the Milky Way. This selection criterion is based on that introduced by Hellwing et al. (2017). These catalogs are useful for exploring the consequences of the fact that we do not reside at a typical location in the Universe, but rather are in a region whose dominant characteristic is the neighboring Virgo-like cluster ($M = [1.2 \pm 0.6] \times 10^{15} h^{-1} M_\odot$) at a distance of $12 \pm 4$ $h^{-1}$Mpc.

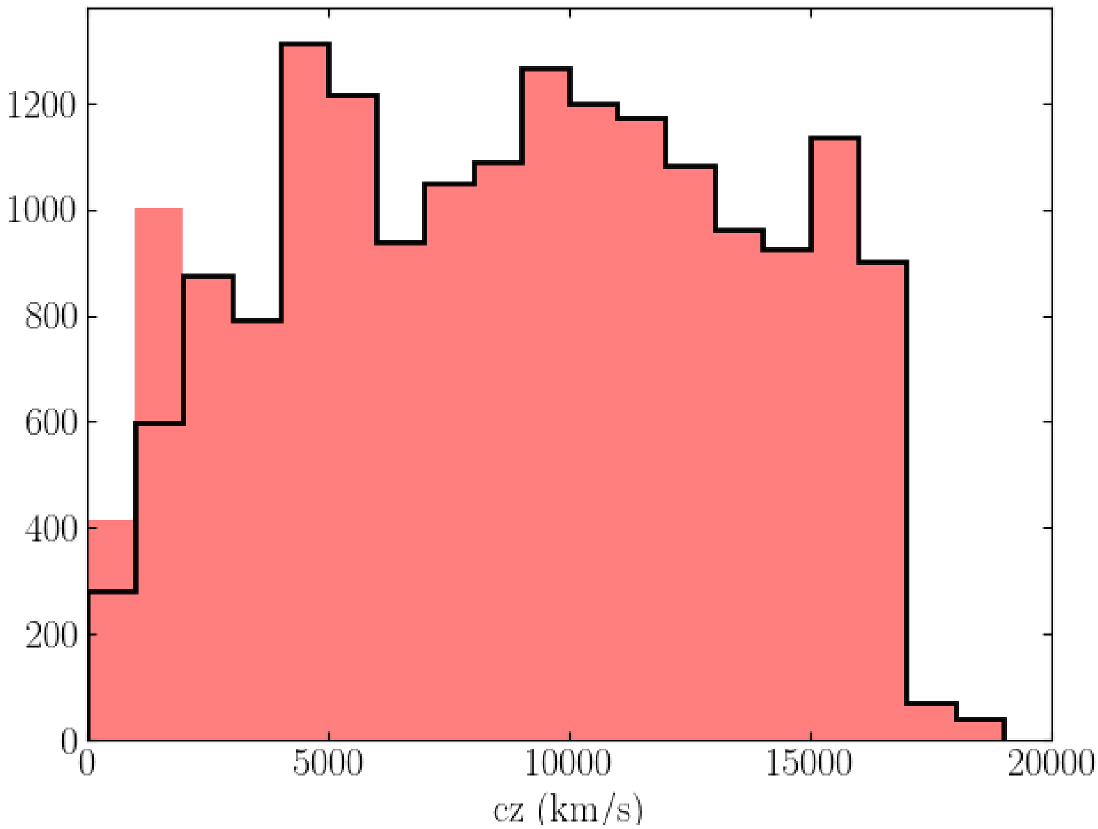

Figure 4.1: The redshift distributions of the full CF3-galaxy catalog(red histogram). The black lined histogram shows the example of the mock catalogs.

We also generated mock catalogs that mimic the angular distribution of the CF3 objects, which is significantly anisotropic. However, we found that the anisotropy of CF3 angular distribution does not have a significant effect on the correlation functions, shown in figure 4.2.

Finally, the effects of measurement (statistical) errors are explored by perturbing the distances of the objects in a mock catalog with a 20% random error, similar to the uncertainties in the CF3 distances. We estimate statistical errors by taking the standard deviations of the results over 100 versions of a perturbed mock catalog. To avoid cosmic variance we average our results over 10 randomly selected mock catalogs.

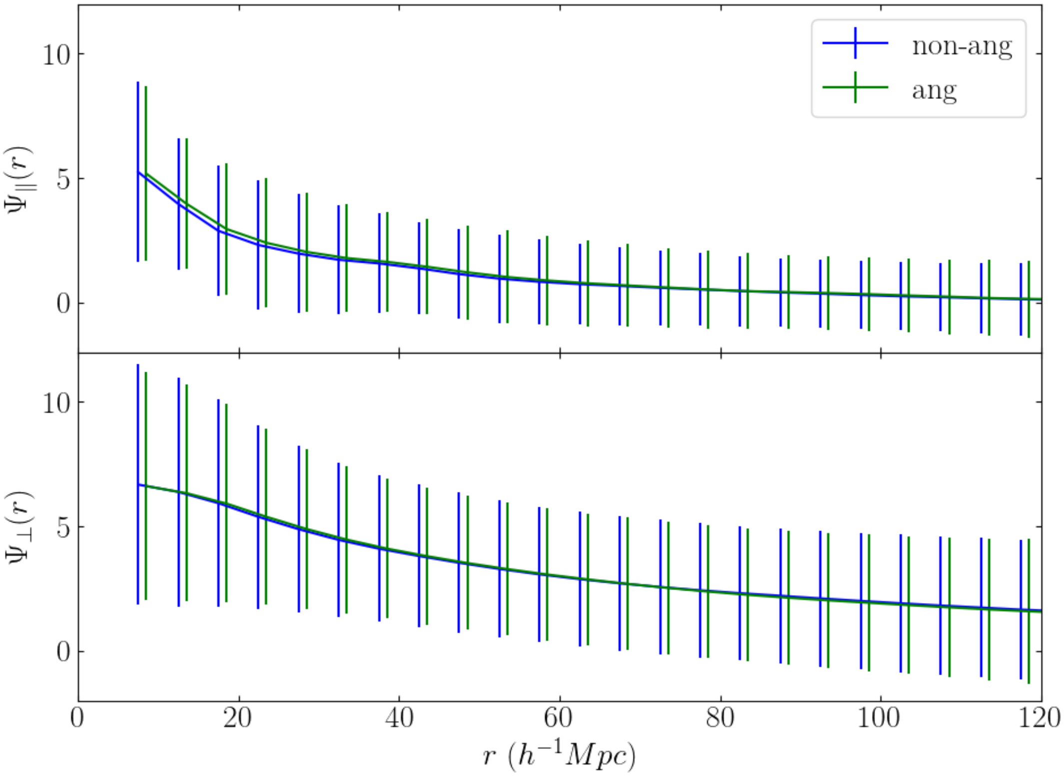

Figure 4.2: $\Psi_{\parallel}$ and $\Psi_{\perp}$ results of mock catalogs with (green) and without (blue) the anisotropy of CF3 angular distribution. The error bars show the total error of the correlations.

## 4.5 Results

Figure 4.3 shows $\Psi_{\parallel}$ and $\Psi_{\perp}$ and their cosmic variance (upper) and statistical errors (lower) using randomly centered mock catalogs with uniform weighting. In the figure, the cosmic variance which is larger than the statistical errors (especially for closer pairs), dominates the error budget. This is consistent with Wang et al. (2018) results that showed that the cosmic variance is the dominant source of error in the Gorski correlation functions, which use uniform weighting. Wang et al. (2018) also showed that the error distribution of the function $\psi_1$ was significantly non-Gaussian. Below we will examine the question of the distribution of the correlation functions in more detail.

Figure 4.4 shows the cosmic variance distribution of $\Psi_{\parallel}$ and $\Psi_{\perp}$, calculated from our estimators using uniform weighting, and $\psi_1$, and $\psi_2$ calculated using the Gorski (1988) formalism, for 100 randomly centered mock catalogs. We show the distributions for a particular bin (40-45 $h^{-1}$Mpc)

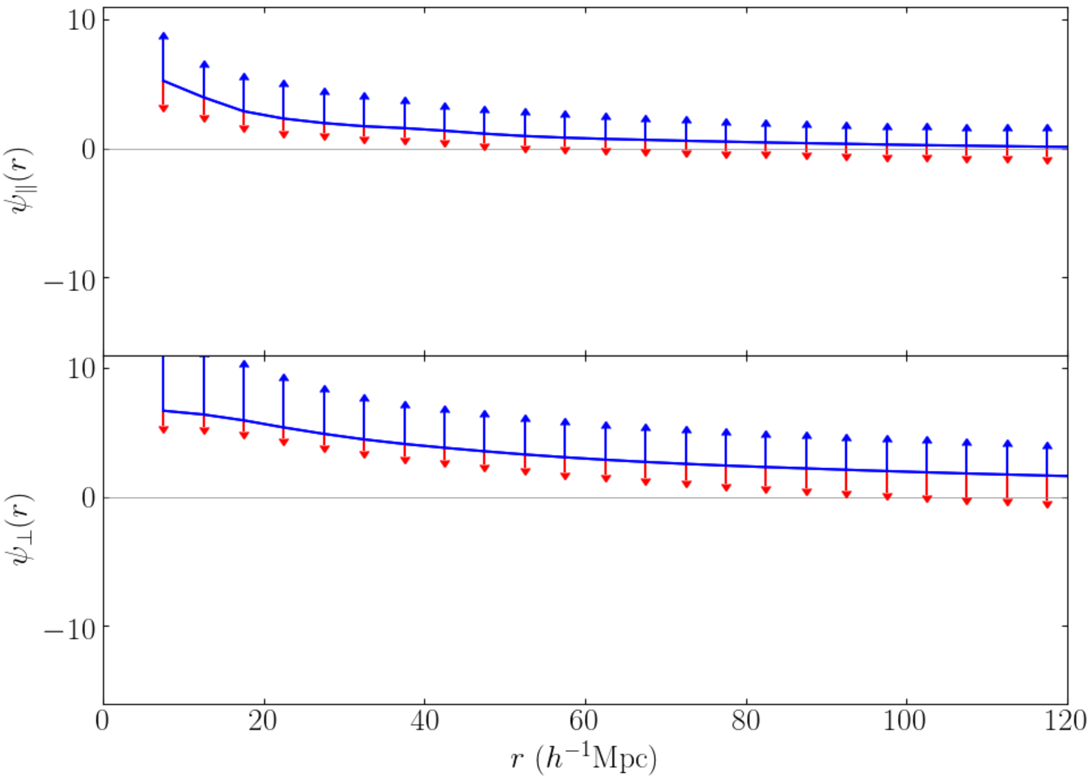

Figure 4.3: The parallel and perpendicular correlation functions of randomly centered mock catalogs with uniform weighting. $\Psi_{\parallel}$ and $\Psi_{\perp}$ are in units of (100 km s$^{-1}$)$^2$. The blue solid lines show the average values for 100 mock catalogs. The upper blue error bars show the standard deviation of the values from individual catalogs, which is the cosmic variance. The lower red error bars indicate the statistical errors calculated; these were calculated by taking the standard deviations of the results of 100 versions of a mock catalog perturbed with random measurement errors. The values given are the average standard deviation taken over 30 mock catalogs.

as an example. In the figure, we see that $\Psi_{\parallel}$ and $\psi_2$ have roughly Gaussian distributions, while the distributions of $\Psi_{\perp}$ and $\psi_1$ are noticeably skewed, with significant non-Gaussian tails. The similarity of $\Psi_{\parallel}$ and $\psi_2$ is not surprising, since $\psi_2$ is calculated from the projections of the radial velocities onto the separation vectors. The other Gorski correlation function, $\psi_1$, is estimated from the unprojected radial velocity, making it a combination of $\Psi_{\parallel}$ and $\Psi_{\perp}$. Quantities with non-Gaussian distributions are difficult to interpret, suggesting that studies of the velocity correlation function should focus on $\Psi_{\parallel}$. We will return to this issue in Section 4.7.

Figure 4.5 shows the $\Psi_{\parallel}$ and $\Psi_{\perp}$ estimators (eq. 4.8 and 4.9) and 3D velocity fields (eq. 4.10 and 4.11) using randomly centered mock catalogs. The simulation results agree well with linear

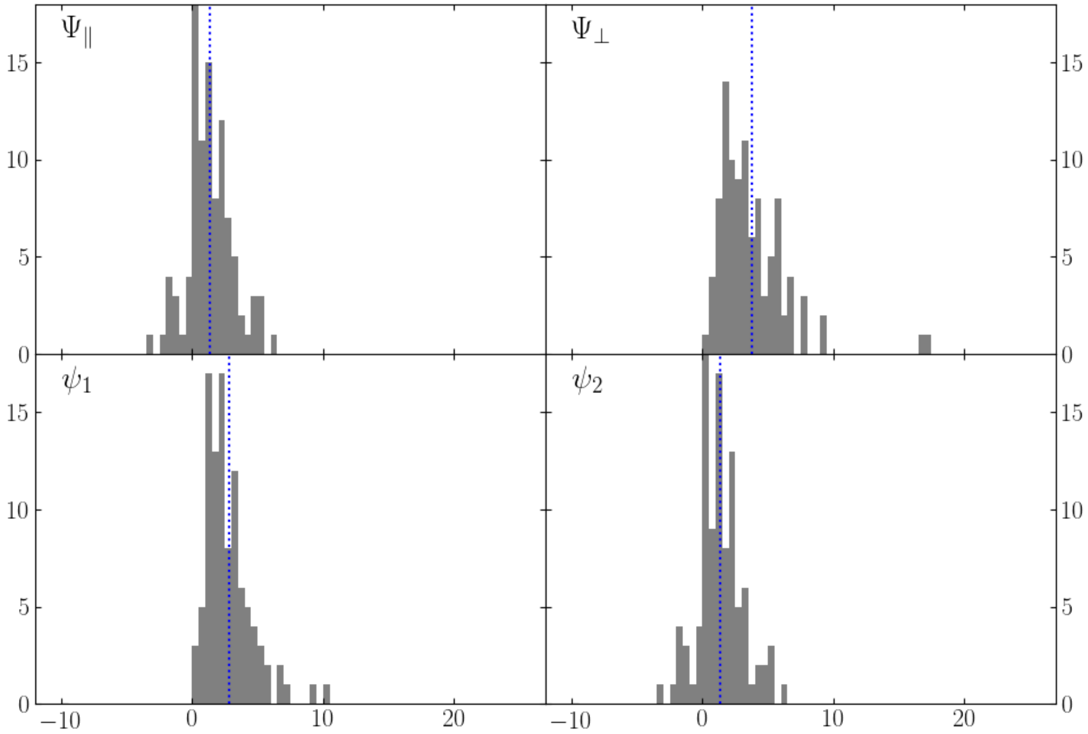

Figure 4.4: The distribution of $\Psi_{\parallel}$, $\Psi_{\perp}$, $\psi_1$, and $\psi_2$ in 40-45 $h^{-1}$Mpc bin of 100 randomly centered mock catalogs using uniform weighting, in units of (100 km s$^{-1}$)$^2$. The blue dotted vertical line is the mean of the mock catalogs.

predictions for both $\Psi_{\parallel}$ and $\Psi_{\perp}$. Although the estimators use only line of sight peculiar velocities, they also agree well with the full 3D results, lending credence to their efficacy and stability.

Hellwing et al. (2017) discussed the effect of observer location on velocity statistics. They compared both the Gorski velocity correlation function estimators and the pairwise velocity statistic calculated for mock catalogs with random halo centers and for those centered on locations that mimicked the local group (LG) and found that the correlation functions calculated from the local group-like catalogs exhibited significant bias relative to linear theory. To study the effects of the observer location on the parallel and perpendicular correlation functions, we display the results of using random and LG centered mock catalogs. We show that $\Psi_{\parallel}$ and $\Psi_{\perp}$ for the LG centered mock catalogs with uniform weighting are also biased. As we discuss below, this bias can be greatly reduced through the use of weighting.

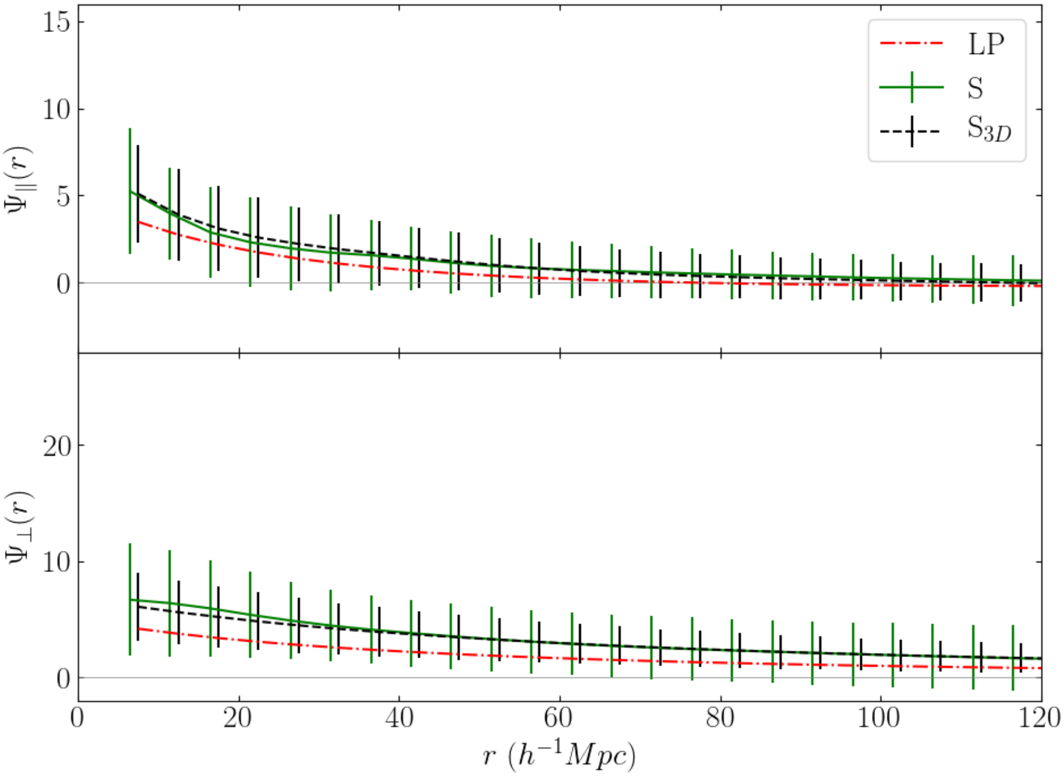

Figure 4.5: The parallel and perpendicular correlation functions of 100 randomly centered mock catalogs in units of (100 km $s^{-1}$)$^2$. The red dash-dotted lines show the linear predictions (LP). The green solid lines indicate the average of mock catalog results calculated using the estimators discussed in the text (S). The black dashed lines indicate the average of mock catalog results for the full 3D velocity fields ($S_{3D}$). The error bars show the cosmic variance over the mock catalogs.

Figure 4.6 shows the parallel and perpendicular correlation results of using LG centered mock catalogs with uniform weighting ($w = 1$). We see that the restriction to local group-like locations introduces significant systematic bias into our results relative to linear theory. This bias takes two distinct forms. First, we see that both our estimators, which use only radial velocities, do not accurately recover the 3D correlation function. Second, we see that, especially for the perpendicular correlation function, the average correlations calculated from the 3D velocities also do not accurately reflect linear theory. Both of these biases arise, most likely, because the volumes around the LG centered mock catalogs are not “typical", but rather exhibit particular flow patterns that are significantly different than the averages taken over random volumes.

Figure 4.7 shows a comparison between random and LG centered mock catalogs. The error

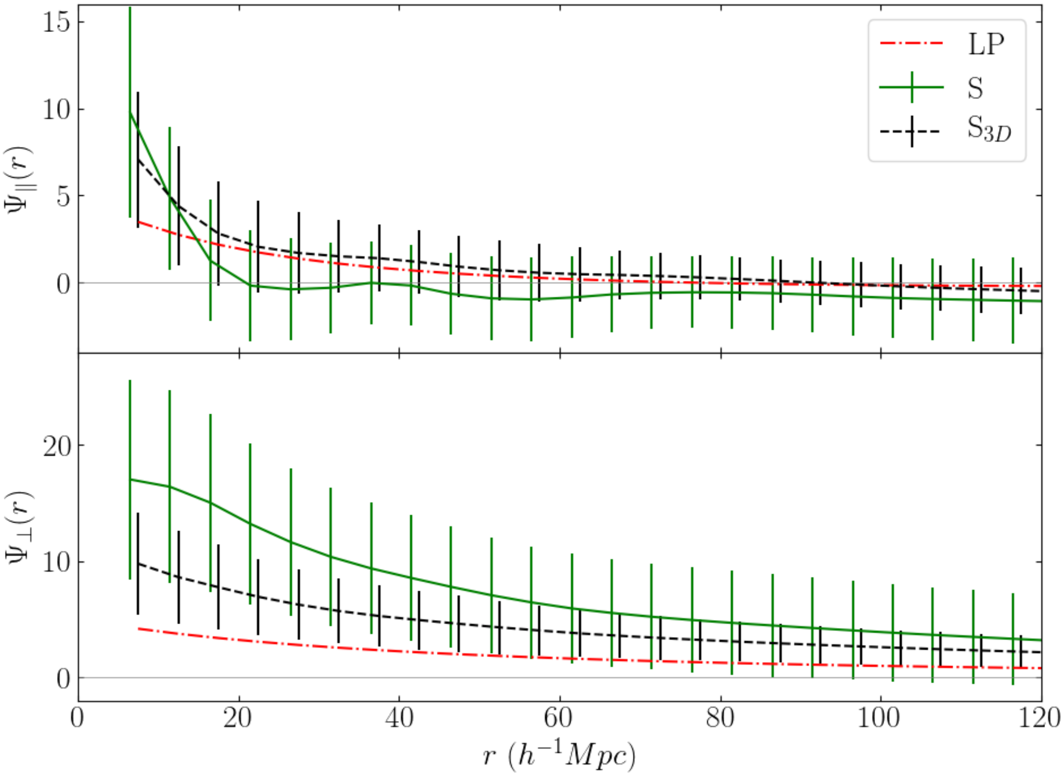

Figure 4.6: Same as Figure 4.5 but using LG centered mock catalogs.

bars of the simulation results show the total error ($\sigma_t = \sqrt{\sigma_c^2 + \sigma_s^2}$, where $\sigma_t$ is the total error, $\sigma_c$ is the cosmic variance and $\sigma_s$ is the statistical error) of the correlation functions. We see that the variance of the LG centered mock catalogs is significantly larger than that of the randomly centered mock catalogs, particularly for the perpendicular correlation function ($\Psi_\perp$).

The fact that the bias in the estimated correlation functions with uniform weights in LG centered mock catalogs has the same order of magnitude as the correlation functions themselves suggests that correlation functions calculated using the CF3 with uniform weights, which includes those calculated using the Gorski method, should not be used in comparisons with linear theory.

As discussed above, weighting can be used to increase the effective volume of the survey. Our approach will be to weight galaxy pairs by $w = (r_1 r_2)^p$, where $r_1$ and $r_2$ are the distances of the two galaxies and $p$ is a non-negative power. In the LG centered mock catalogs, this weighting reduces emphasis on the relatively small volume near the center of the survey, which for the LG centered mock catalogs is atypical. We will see that the use of weighting can effectively reduce

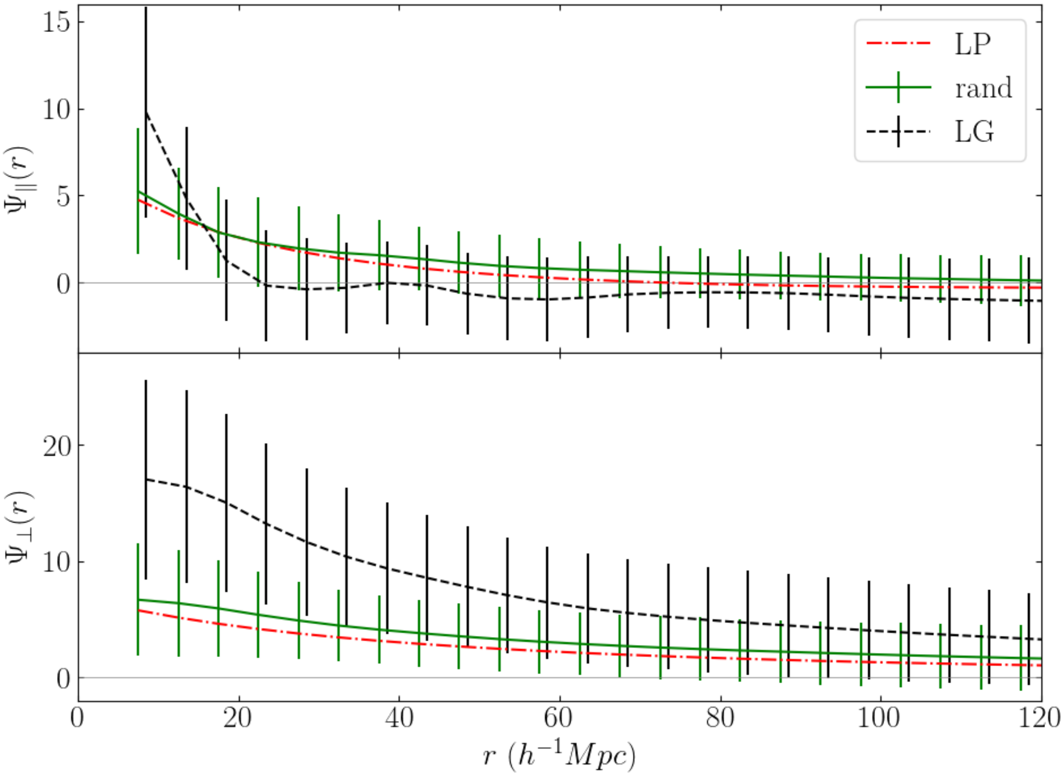

Figure 4.7: Parallel and perpendicular correlation results of 100 random centered and 100 LG centered mock catalogs in units of (100 km $s^{-1}$)$^2$ using uniform weighting ($w = 1$). All mock catalogs have had galaxy distances perturbed by random measurement errors. The red dash-dotted lines show the linear predictions. The green solid lines indicate the average results for the randomly centered mock catalogs. The black dashed lines show the average results for the LG centered mock catalogs. The error bars show the total error of the correlation function, which includes both cosmic variance and statistical error.

the bias found in the LG centered mock catalogs.

Figure 4.8 shows the results using weights $w = (r_1 r_2)^p$ with $p = 0.5, 1, 2$, respectively ($p = 0$ gives uniform weights). The use of weighting has reduced the bias to an insignificant level. However, the total error becomes larger while increasing the effective volume of the surveys.

Figure 4.9 shows the cosmic variance and the statistical errors of the weighted correlation functions with $p = \frac{1}{2}$ ($w = (r_1 r_2)^{1/2}$), $p = 1$ ($w = r_1 r_2$), and $p = 2$ ($w = (r_1 r_2)^2$), respectively. The cosmic variance generally decreases with weighting as expected; however, the statistical errors increase and dominate when using weights with larger $p$. Table 4.2 shows the cosmic variance and statistical errors of $\Psi_{\parallel}$ with different weighting volumes. Considering that tension, $p = 1$

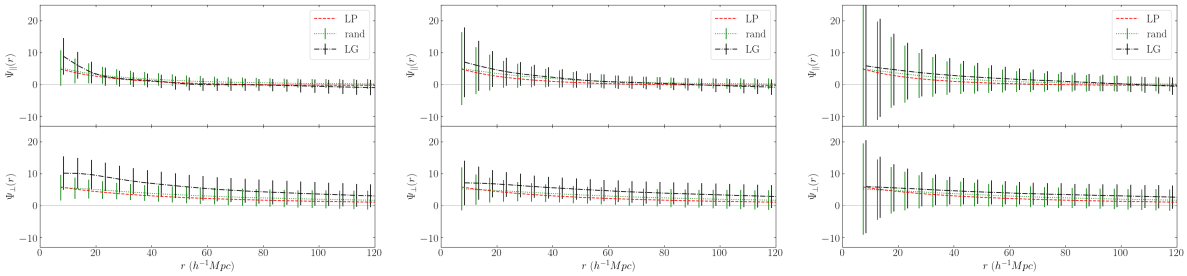

Figure 4.8: Same as Figure 4.7 but using position weighted method with weights $p = 1/2$ (left panel), $p = 1$ (middle panel), and $p = 2$ (right panel).

($w = r_1 r_2$) gives the optimal results.

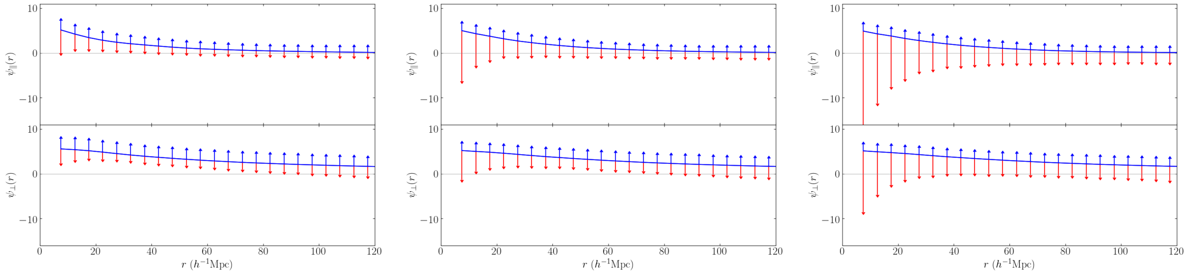

Figure 4.9: The parallel and perpendicular correlation functions with weights $p = \frac{1}{2}$ (left panel), $p = 1$ (middle panel), and $p = 2$ (right panel). $\Psi_{\parallel}$ and $\Psi_{\perp}$ are in units of (100 km s$^{-1}$)$^2$. The blue solid lines show averages over 100 mock catalogs. The upper blue error bars show the cosmic variance. The lower red error bars indicate the statistical errors; these were calculated by taking the standard deviations of the results of 100 versions of a mock catalog perturbed with 20% random measurement errors. The values given are the average of the standard deviation taken over 30 mock catalogs. It is quite clear that the statistical errors increase with weighting.

Now that we have determined that $p = 1$ provides the optimal weighting for our analysis, we apply our methods to the actual CF3-galaxy catalog. In Figure 4.10, we show the parallel and perpendicular correlation functions for the CF3-galaxy catalog, using the $p = 1$ ($w = r_1 r_2$) weighting scheme, together with the results (with estimated total uncertainties, including cosmic variance and measurement errors) of both the random and LG centered mock catalogs with the same weighting. We see that both $\Psi_{\parallel}$ and $\Psi_{\perp}$ have the expected behavior: decreasing amplitude with increasing separation. Also as expected from linear theory, $\Psi_{\perp}$ decreases more slowly and has larger amplitude than $\Psi_{\parallel}$ at large separation. Considering the magnitudes of the total uncertainties, both $\Psi_{\parallel}$ and $\Psi_{\perp}$ are consistent (within two standard deviations) with the results from the mock

Table 4.2: The errors of $\Psi_{\|}$ with random observer using different weighting schemes. The $\sigma_t$, $\sigma_c$ and $\sigma_s$ indicate the total error, cosmic variance and statistical errors of the correlation function in units of (100 km s$^{-1}$)$^2$, respectively. The bin regions are in unit of $h^{-1}$Mpc.

| Weight | $p$ | | [15-20] | [35-40] | [55-60] |
|---|---|---|---|---|---|
| 1 | 0 | $\sigma_c$ | 2.45 | 1.88 | 1.59 |
| | | $\sigma_s$ | 0.95 | 0.66 | 0.66 |
| | | $\sigma_t$ | 2.63 | 1.99 | 1.72 |
| $\sqrt{r_1 r_2}$ | $\frac{1}{2}$ | $\sigma_c$ | 1.78 | 1.48 | 1.29 |
| | | $\sigma_s$ | 2.58 | 1.45 | 1.13 |
| | | $\sigma_t$ | 3.13 | 2.07 | 1.71 |
| $r_1 r_2$ | 1 | $\sigma_c$ | 1.59 | 1.37 | 1.14 |
| | | $\sigma_s$ | 5.37 | 2.54 | 1.79 |
| | | $\sigma_t$ | 5.6 | 2.89 | 2.12 |
| $(r_1 r_2)^2$ | 2 | $\sigma_c$ | 1.59 | 1.47 | 1.27 |
| | | $\sigma_s$ | 11.39 | 5.04 | 3.36 |
| | | $\sigma_t$ | 11.5 | 5.25 | 3.59 |

catalogs, and thus consistent with the standard cosmological model.

## 4.6 Parameter Constraints

In Wang et al. (2018), we showed that the correlation function $\psi_1$ has a long, non-Gaussian tail in its cosmic variance distribution, making it unsuitable for placing constraints on cosmological parameters. As we discussed in section 4.5, the cosmic variance of $\psi_{\|}$ exhibits a better approximation of a Gaussian distribution than $\psi_1$. This suggests that $\psi_{\|}$ may be a more useful measurement of peculiar velocity correlations. In this section, we test the performance of uniformly weighted and position weighted $\psi_{\|}$ with both random and LG observers with respect to putting constraints on cosmological parameters.

As can be seen in Figure 4.9, the statistical errors increase with weighting. To test the effect of larger statistical errors and cosmic variances on the cosmological parameter constraints, we implement three fitting methods ($\chi^2_c$, $\chi^2_s$ and $\chi^2_t$) given by

$$\chi^2_c = \sum_{i,j} \left[\psi^S_{\|}(r_i) - \psi^L_{\|}(r_i)\right] C^{-1}_{ij} \left[\psi^S_{\|}(r_j) - \psi^L_{\|}(r_j)\right], \qquad (4.15)$$

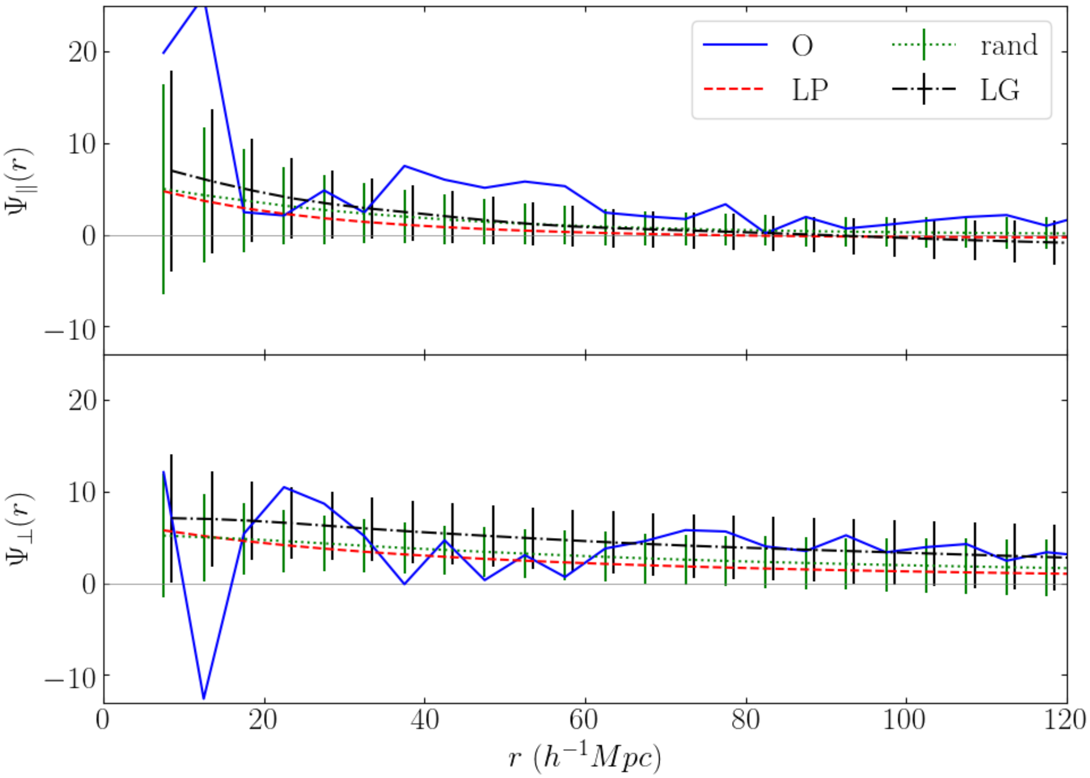

Figure 4.10: The blue dotted lines indicate the parallel and perpendicular correlation estimates in units of (100 km $\mathrm{s}^{-1})^2$ calculated from the CF3-galaxy catalog using weighting scheme $w = r_1 r_2$ ($p = 1$). The red dash-dotted lines show the linear prediction. The green solid lines indicate the average results from randomly centered mock catalogs with the same weighting. The black dashed lines show the average results from the LG centered mock catalogs, also with the same weighting. The error bars show the total uncertainty, including cosmic variance and measurement errors.

$$\chi_s^2 = \Sigma_{i,j}\left[\psi_\parallel^S(r_i) - \psi_\parallel^L(r_i)\right]\varepsilon_{ij}^{-1}\left[\psi_\parallel^S(r_j) - \psi_\parallel^L(r_j)\right], \tag{4.16}$$

$$\chi_t^2 = \Sigma_{i,j}\left[\psi_\parallel^S(r_i) - \psi_\parallel^L(r_i)\right]\left(C_{ij} + \varepsilon_{ij}\right)^{-1}\left[\psi_\parallel^S(r_j) - \psi_\parallel^L(r_j)\right], \tag{4.17}$$

where

$$C_{ij} = \frac{1}{N_{mock}} \sum_{l=1}^{N_{mock}} \left(\Psi_{\parallel,l}^i - \overline{\Psi}_\parallel^i\right)\left(\Psi_{\parallel,l}^j - \overline{\Psi}_\parallel^j\right), \tag{4.18}$$

$$\varepsilon_{ij} = \frac{1}{N_{pert}} \sum_{p=1}^{N_{pert}} \left(\Psi_{\parallel,p}^i - \Psi_{\parallel,A}^i\right)\left(\Psi_{\parallel,p}^j - \Psi_{\parallel,A}^j\right). \tag{4.19}$$

$\chi_c^2$ (equation 4.15) uses the covariance matrix that only containes the cosmic variance information, where $C$ is the covariance matrix of cosmic variance; $N_{mock}$ is the number of mock catalogs;

$\psi^i_{\parallel,l}$ is the correlation value of the $i^{th}$ separation bin of the $l^{th}$ mock catalogue; $\overline{\psi}^i_{\parallel}$ is the average value of $N_{mock}$ catalogs in the $i$th separation bin; $\psi^S_{\parallel}$ is the average value of $\psi_{\parallel}$ over $N_{mock}$ mock catalogs; $\psi^L_{\parallel}$ is the linear prediction.

$\chi^2_s$ (equation 4.16) implement the covariance matrix that contains the information of statistical errors, where $\varepsilon$ is the covariance matrix of statistical errors; $\psi^i_{\parallel,A}$ is the parallel correlation of a selected mock catalog whose value closes to the average value of the 100 mock catalogs in the $i$th separation bin; $\psi^i_{\parallel,p}$ is the correlation value of the $i^{th}$ separation bin of the $p^{th}$ perturbed catalog of the selected the mock catalog; $N_{pert}$ is the number of perturbed catalogs. The value of the selected mock catalog $\psi_{\parallel,A}$ is close to the average of 100 mock catalogs. The parameter constraints of using a selected mock catalog is similar as using a random mock catalog, but slightly tighter than using a random mock catalog. $\chi^2_t$ (equation 4.16) combines two covariance matrices that contain the information of both the cosmic variance and statistical errors.

Figure 4.11 shows the cosmological parameters constraints for $\Omega_m$ and $\sigma_8$. In our test, we find the results using $\Psi_{\parallel}$ are much stabler than using $\psi_1$ for implementing different truncations (see Wang et al., 2018).

For the $\chi^2_c$ fitting method, all of the four correlation weights, $p = 0$ ($w = 1$), $p = 0.5$ ($w = (r_1r_2)^{1/2}$), $p = 1$ ($w = r_1r_2$), $p = 2$ ($w = (r_1r_2)^2$), agree with the simulation value within $1\sigma$ for both the random and LG observers. However, the results of the uniform weighted $\Psi_{\parallel}$ with the LG observer are not as consistent as the results of random observers. The position weighted method improves the parameter constraints for LG observer significantly. It provides tighter and stabler constraints than the uniform weighted $\Psi_{\parallel}$, which is due to the smaller cosmic variance of the position weighted $\Psi_{\parallel}$. In addition, the position weighted $\Psi_{\parallel}$ provides closer constraining results to the expected value (simulation value) for both the random and LG observers. Comparing the results of the three position weighted $\Psi_{\parallel}$, $p = 1$ provides the most optimal results.

In the $\chi^2_s$ plots, all of the four correlation weights agree with the simulation value within $1\sigma$ for the random observer, while only the position weighted ($p = 0.5, 1, 2$) correlations agree with the simulation value within $1\sigma$ for the LG observer. Similar as the results of $\chi^2_c$ method, the uniform

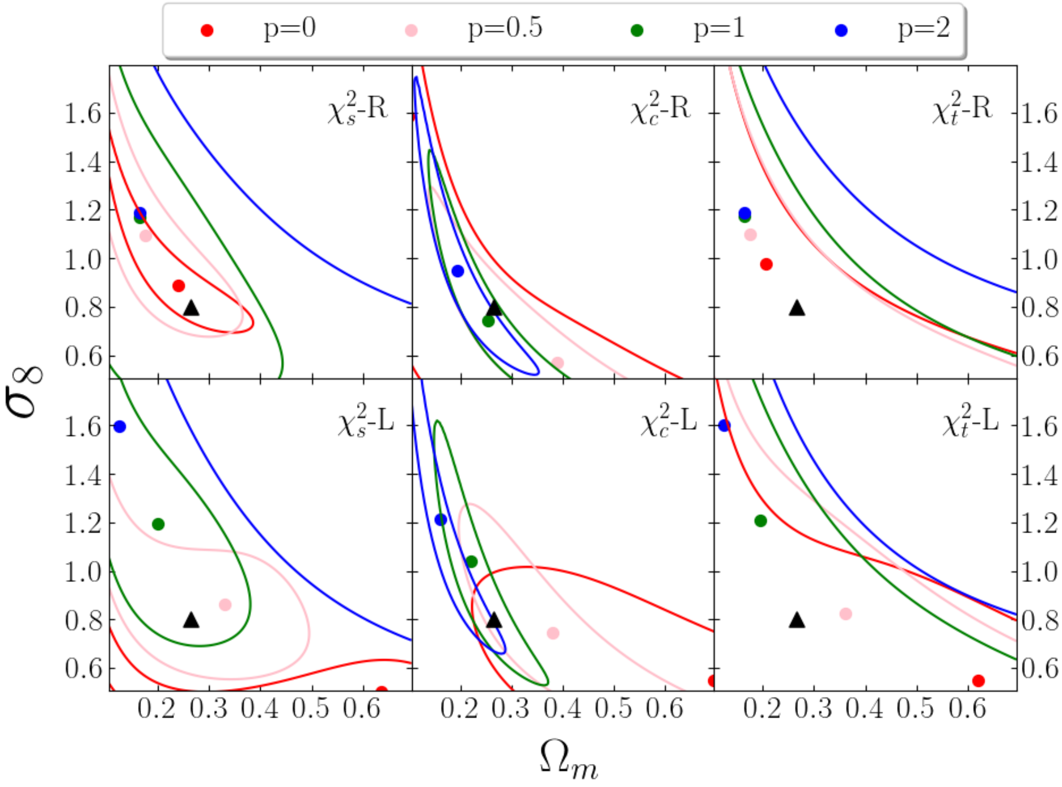

Figure 4.11: $\Omega_m$ and $\sigma_8$ constrains using simulation data with bin equals 500 km s$^{-1}$ and truncation at 6000 km s$^{-1}$. The minimum $\chi^2$ value has been subtracted from each cell. The contours indicate 68% likelihood of $\chi^2$ values. The triangle marker indicates the value from the OuterRim Simulation. $\chi^2_c$ shows the result of covariance matrix with cosmic variance, $\chi^2_s$ indicates the result of covariance matrix with statistical errors, and $\chi^2_t$ combines two covariance matrices that contain the information of both the cosmic variance and statistical errors. R and L indicate the random and LG observers, respectively.

weighted $\Psi_{\|}$ provides a biased parameter constraints for the LG observer, which is greatly improved by the position weighted method. However, the position weighted $\Psi_{\|}$ has laxer constraints than the uniform weighted $\Psi_{\|}$, which is opposite to the $\chi^2_c$ fitting method. This is due to the larger statistical errors caused by the larger position weights. The constraining results for weight $p = 0.5$ is roughly as tight as the uniform weighted $\Psi_{\|}$, which makes it the most optimal weight for the $\chi^2_s$ method. For the $\chi^2_t$ method that combines both cosmic variance and statistical error, the constraining results are even laxer, which is not reliable enough for parameter constraints. In addition, the results for all the four correlation weights show no significant difference when using the combination covariance matrix.

The position weighted scheme of $\Psi_{\parallel}$ increases the statistical uncertainty of the correlations, and the effect of the large statistical error makes the parameter constraints later. However, it improves the parameter constraining results of the LG observer. The position weighted $\Psi_{\parallel}$ improves the cosmological parameter constraining with tighter and stabler constraints for the $\chi_c^2$ method. For both of the $\chi_c^2$ and $\chi_s^2$ methods, the position weighted $\Psi_{\parallel}$ shows significant improvement in the cosmological parameter constraints of the LG observers. Considering the more Gaussian cosmic variance distribution of $\Psi_{\parallel}$ and smaller bias of the position weighted $\Psi_{\parallel}$ result for LG observers, the position weighted $\Psi_{\parallel}$ is a stabler correlation estimator for dealing with both the random and LG observers. In addition, the constraining results indicate that $p = 1$ ($w = r_1 r_2$) provides the optimal results for $\chi_c^2$ and $p = 0.5$ ($w = \sqrt{r_1 r_2}$) provides the optimal results for $\chi_s^2$.

## 4.7 Conclusion

Previous studies of velocity correlations have mostly focused on $\psi_1$, a correlation function introduced by Gorski (Gorski, 1988). This function has several disadvantages. First, it is dependent on the distribution of objects being analyzed and hence is not comparable between surveys. Second, it is a complicated mixture of the physically meaningful correlation functions that quantify correlations of the velocity components parallel and perpendicular to the separation vector between pairs of galaxies. Third, as shown by Wang et al. (2018), the distribution of cosmic variance in $\psi_1$ is significantly non-Gaussian, complicating its use as a cosmological probe. Finally, as noted by Hellwing et al. (2017), and as we have shown here, our special location near the Virgo cluster can bias correlation functions calculated using typical catalogs whose density of objects decreases rapidly with distance.

In this chapter we have presented an alternative method, an extension of a method introduced by Kaiser (1989) and Groth et al. (1989), that can stably estimate the parallel and perpendicular correlation functions directly from currently available peculiar velocity data. We have shown that the non-Gaussian distribution of the cosmic variance in $\psi_1$ is mostly due to its containing $\Psi_{\perp}$; the parallel correlation function $\Psi_{\parallel}$ has a more Gaussian distribution and therefore should be much more useful as a cosmological statistic.

We showed that the parallel and perpendicular correlation functions calculated with uniform weights are biased in LG centered mock catalogs, especially for small separations. The LG mock catalog results also showed less agreement between the results of using estimators ($\Psi_{||}$ and $\Psi_{\perp}$) and the results of using the full 3D velocity fields ($\Psi_{||}^{3D}$ and $\Psi_{\perp}^{3D}$). $\Psi_{\perp}$ shows more bias, which explains the different behaviors shown by $\psi_1$ and $\psi_2$ when LG centered mock catalogs were used in Hellwing et al. (2017).

Our results, together with those of Hellwing et al. (2017), suggest that velocity correlation functions calculated from peculiar velocity data dominated by nearby galaxies will be biased due to our location near the Virgo Cluster. We have presented a novel way to reduce this bias by including position weights into our analysis. These weights reduce the emphasis on nearby galaxies, which are overrepresented in most catalogs. The weighted correlation functions probe a larger effective volume and thus give better agreement with linear theory. Comparing the results of different weights ($w = (r_1 r_2)^p$), we find the larger power provides better agreement between the results of random and LG observers. However, the statistical errors increase with the power. Therefore, the weight needs to be within a reasonable range to balance the tension between better agreements and larger errors. We found that the optimal weighting scheme requires an intermediate power ($p = 1$) to balance these effects.We have demonstrated that weighting is particularly effective at eliminating bias in the parallel velocity correlation function, $\Psi_{||}$.

Though the weighting scheme increases the statistical errors of the correlations, the larger errors do not degrade the effectiveness of the cosmological parameter constraints estimation significantly. Instead, the position weighted $\Psi_{||}$ provides stabler and tighter constraints with the widely used covariance matrix weighted $\chi^2$ method ($\chi_c^2$). The constraining result using optimal weighting scheme ($p = 1$) show agreements with the simulation value ($\Omega_m = 0.2648$ and $\sigma_8 = 0.8$) within $1\sigma$ for both random and LG observers. Considering the more Gaussian cosmic variance of $\Psi_{||}$ than $\psi_1$ and the tighter constraints of using the position-dependent weighting scheme, we suggest that $\Psi_{||}$ with weight $p = 1$ is a more promising velocity correlation estimator. However, the constraints with the LG observer are not as stable as those using the random observer, even though the bias and the parameter constraints has been improved significantly by the position-dependent weighting scheme, requires for further studies.

## 4.8 Acknowledgements

HAF and RW were partially supported by NSF grant AST-1907404. An award of computer time was provided by the INCITE program. This research used resources of the Argonne Leadership Computing Facility, which is a DOE Office of Science User Facility supported under Contract DE-AC02-06CH11357. RW and SP acknowledge support from the Murdock Charitable Trust College Research Program.

# Chapter 5

# Conclusion

In this dissertation, I presented the work we did in studying the dynamics and statistics of large-scale structure of the Universe with peculiar velocity fields. In this chapter, I will encapsulate the significant findings of our work.

In chapter 2, we tested the feasibility of using deep learning neural networks to simplify the estimation of kSZ peculiar velocities from the conventional method that requires several steps, such as map filtering and optical depth estimates. Furthermore, the optical depth measurement makes it difficult to predict the peculiar velocity accurately with the conventional method. By comparing the results using simulation data from different redshift slices, we found our deep learning neural network model is redshift independent, which is consistent with the theory. In addition, the pairwise velocity statistic of our neural network predictions indicates that our model provides reliable peculiar velocities for cosmological studies. Our results suggest that models using kSZ and using both kSZ and tSZ show no significant difference, which means the deep learning neural network simplified kSZ velocity estimate may only need kSZ input. We tested the feasibility of applying our model to observations by perturbing the kSZ signals with three different noise representations and found a possible way of applying deep learning algorithms to observations by training the model with simulation data sets that include various noise models corresponding to observations. However, a suitable model for observations needs more observational kSZ detections of individual galaxy clusters in the future. To summarize, using deep learning neural networks to estimate peculiar velocities from the kSZ effect is both feasible and promising. It could simplify the conventional calculation of kSZ peculiar velocities significantly with only kSZ input, which avoids difficulties arising from the estimation of optical depth as well as map integral and filtering.

In chapter 3, we studied the Gorski velocity correlation function theoretically and statistically using simulations and observations. We presented the analysis of the velocity correlation function and the simplified estimator of moments of the selection function. We have shown that on average the correlation function calculated from simulated catalogues recovers the expected signal from linear theory. In the error analysis, we found the statistical errors of the correlation function are significantly smaller than the cosmic variance, which means the velocity correlation function does a reasonable job dealing with the large uncertainty of peculiar velocities. However, the cosmic variance distribution of the Gorski velocity correlation function is not Gaussian but a combination of Gaussian and Wishart distributions. We clarified the effect of the non-Gaussian skew on cosmological parameter constraints. Furthermore, since the cosmic variance is smaller at larger separations, the covariance matrix gives more weight at larger separations, where skewness is most pronounced and thus, may introduce systematic biased parameter estimations. In addition, redshift distortions give rise to the mismatch between CosmicFlows correlations and linear predictions and thus may contribute further bias to parameter constraints. To mitigate this effect, we have used a weighting scheme that combines the effects of cosmic variance and redshift distortion, which appears to be both more stable and less biased. Our parameter constraints agree with the Planck and WMAP9 results. However, the cosmological parameter constraints using Gorski velocity correlation function is very unstable due to its non-Gaussian cosmic variance distribution.

Furthermore, the Gorski velocity correlation function is dependent on the distribution of objects being analyzed and hence is not comparable between surveys. As noted by Hellwing et al. (2017), our special location near the Virgo cluster can bias correlation functions estimated using typical catalogs whose density of objects decreases rapidly with distance.

In chapter 4, we presented a feasible solution for the above problems. We have presented an alternative method, an extension of a method introduced by Kaiser (1989) and Groth et al. (1989), that can stably estimate the parallel and perpendicular correlation functions directly from currently available peculiar velocity data. We have shown that the non-Gaussian distribution of the cosmic variance in Gorski correlation function is mostly due to the perpendicular correlation function.

The parallel correlation function has a more Gaussian cosmic variance distribution and therefore should be much more useful as a cosmological statistic. Due to observational restrictions, velocity surveys have more galaxies nearby, whereas in reality the number of galaxies increase with volume and distance. To balance the overrepresented nearby galaxies relative to the more distant galaxies, we formulated a position-dependent weighting scheme in the new estimators. From simulations, we saw that galaxy distributions of velocity surveys centered at a position near a Virgo-like cluster (LG) are different from galaxy distributions of surveys centered randomly. Thus, correlation functions with LG observers are more biased than correlations with random observers. We found that using the position-dependent weighting scheme could significantly reduce the systematic bias caused by different observers. However, the statistical error increases and becomes dominant compared to the cosmic variance as the weight power increases, leading to a larger total error. Though the weighting scheme increases the statistical errors of the correlations, the larger errors do not degrade the effectiveness of the cosmological parameter constraints significantly. Instead, the position weighted parallel correlation function provides stabler and tighter constraints with the widely used covariance matrix weighted $\chi^2$ method. The constraining results using optimal weighting scheme show agreements with the simulation values within $1\sigma$ for both random and LG observers. Considering the more Gaussian distribution of cosmic variance of the parallel correlation function than the Gorski correlation function and the tighter constraints of using the position-dependent weighting scheme, we suggest that the parallel correlation function with the optimal weight is a more promising velocity correlation estimator. The results suggest that the parallel velocity correlation function is a powerful cosmological probe, given that it has a better Gaussian distribution than other velocity correlation functions and that its bias is more easily reduced by weighting.

With future kSZ detections of individual clusters, we can extend the depth of peculiar velocity catalogs to high redshift. This will bring the study of large-scale velocity fields to an new era, e.g., peculiar velocity studies for distant galaxy clusters may provide an independent method for constraining Hubble constant. In future work, I propose to further investigate the kSZ effect with observational data and further improve our deep learning neural network model. Furthermore, the application of machine learning algorithms on cosmological studies is very promising. I would hone my skills using machine learning and data analysis with velocity field studies as well as other fields, such as CMB and gravitational lensing.

# Bibliography

Abate, A. & Erdoğdu, P. (2009). Peculiar velocities into the next generation: cosmological parameters from the SFI++ survey. *MNRAS*, 400, 1541–1547.

Abate, A. & Feldman, H. A. (2012). Detected fluctuations in Sloan Digital Sky Survey luminous red galaxy magnitudes: bulk flow signature or systematic? *MNRAS*, 419, 3482–3490.

Adams, C. & Blake, C. (2020). Joint growth rate measurements from redshift-space distortions and peculiar velocities in the 6dF Galaxy Survey. *MNRAS*.

Agarwal, S., Abdalla, F. B., Feldman, H. A., Lahav, O., & Thomas, S. A. (2012a). PkANN - I. Non-linear matter power spectrum interpolation through artificial neural networks. *MNRAS*, 424, 1409–1418.

Agarwal, S., Abdalla, F. B., Feldman, H. A., Lahav, O., & Thomas, S. A. (2014). PkANN - II. A non-linear matter power spectrum interpolator developed using artificial neural networks. *MNRAS*, 439, 2102–2121.

Agarwal, S., Feldman, H. A., & Watkins, R. (2012b). Testing the minimum variance method for estimating large-scale velocity moments. *MNRAS*, 424, 2667–2675.

Atrio-Barandela, F., Kashlinsky, A., Ebeling, H., & Kocevski, D. (2012). Cosmic Microwave Background filters and the Dark-Flow measurement. *arXiv e-prints*, (pp. arXiv:1211.4345).

Battaglia, N. (2016). The tau of galaxy clusters. *JCAP*, 2016(8), 058.

Beck, A. M., Murante, G., Arth, A., Remus, R.-S., Teklu, A. F., Donnert, J. M. F., Planelles, S., Beck, M. C., Förster, P., Imgrund, M., Dolag, K., & Borgani, S. (2016). An improved SPH scheme for cosmological simulations. *MNRAS*, 455, 2110–2130.

Bel, J., Pezzotta, A., Carbone, C., Sefusatti, E., & Guzzo, L. (2018). Accurate fitting functions for peculiar velocity spectra in standard and massive-neutrino cosmologies. *ArXiv e-prints*.

Bennett, C. L., Larson, D., Weiland, J. L., Jarosik, N., Hinshaw, G., Odegard, N., Gold, B., Halpern, M., Komatsu, E., Nolta, M. R., Page, L., Spergel, D. N., Wollack, E., Dunkley, J., Kogut, A., Limon, M., Meyer, S. S., Tucker, G. S., & Wright, E. L. (2013). Nine-year Wilkinson Microwave Anisotropy Probe (WMAP) Observations: Final Maps and Results. *ApJ Supp*, 208, 20.

Benson, B. A., Church, S. E., Ade, P. A. R., Bock, J. J., Ganga, K. M., Hinderks, J. R., Mauskopf, P. D., Philhour, B., Runyan, M. C., & Thompson, K. L. (2003). Peculiar Velocity Limits from Measurements of the Spectrum of the Sunyaev-Zeldovich Effect in Six Clusters of Galaxies. *ApJ*, 592(2), 674–691.

Bernardi, M., Alonso, M. V., da Costa, L. N., Willmer, C. N. A., Wegner, G., Pellegrini, P. S., Rité, C., & Maia, M. A. G. (2002). Redshift-Distance Survey of Early-Type Galaxies. I. The ENEARc Cluster Sample. *AJ*, 123, 2990–3017.

Bertschinger, E. & Dekel, A. (1989). Recovering the full velocity and density fields from large-scale redshift-distance samples. *ApJL*, 336, L5–L8.

Bhattacharya, S. & Kosowsky, A. (2008). Systematic errors in Sunyaev Zeldovich surveys of galaxy cluster velocities. *JCAP*, 8, 030.

Bianchi, D., Percival, W. J., & Bel, J. (2016). Improving the modelling of redshift-space distortions- II. A pairwise velocity model covering large and small scales. *MNRAS*, 463, 3783–3798.

Blobel, V. (2003). Some Comments on $X^2$ Minimization Applications. In L. Lyons, R. Mount, & R. Reitmeyer (Eds.), *Statistical Problems in Particle Physics, Astrophysics, and Cosmology* (pp. 101).

Borgani, S., da Costa, L. N., Zehavi, I., Giovanelli, R., Haynes, M. P., Freudling, W., Wegner, G., & Salzer, J. J. (2000). Correlation Analysis of SFI Peculiar Velocities. *AJ*, 119, 102–110.

Burstein, D. (1990). REVIEW: Large-scale motions in the Universe: a review. *Reports on Progress in Physics*, 53(4), 421–481.

Calafut, V., Bean, R., & Yu, B. (2017). Cluster mislocation in kinematic Sunyaev-Zel'dovich effect extraction. *Phys Rev D*, 96(12), 123529.

Colless, M., Saglia, R. P., Burstein, D., Davies, R. L., McMahan, R. K., & Wegner, G. (2001). The peculiar motions of early-type galaxies in two distant regions - VII. Peculiar velocities and bulk motions. *MNRAS*, 321, 277–305.

Corey, B. E. & Wilkinson, D. T. (1976). A Measurement of the Cosmic Microwave Background Anisotropy at 19 GHz. In *Bull. Am. Astron. Soc.*, volume 8 (pp. 351).

da Costa, L. N., Bernardi, M., Alonso, M. V., Wegner, G., Willmer, C. N. A., Pellegrini, P. S., Rité, C., & Maia, M. A. G. (2000). Redshift-Distance Survey of Early-Type Galaxies. I. Sample Selection, Properties, and Completeness. *AJ*, 120, 95–109.

D'Agostini, G. (1995). Probability and Measurement Uncertainty in Physics - a Bayesian Primer. *ArXiv High Energy Physics - Phenomenology e-prints*.

Dale, D. A., Giovanelli, R., Haynes, M. P., Campusano, L. E., & Hardy, E. (1999). Seeking the Local Convergence Depth. V. Tully-Fisher Peculiar Velocities for 52 Abell Clusters. *AJ*, 118, 1489–1505.

Davis, M., Nusser, A., Masters, K. L., Springob, C., Huchra, J. P., & Lemson, G. (2011). Local gravity versus local velocity: solutions for $\beta$ and non-linear bias. *MNRAS*, 413, 2906–2922.

Davis, M., Nusser, A., & Willick, J. A. (1996). Comparison of Velocity and Gravity Fields: The Mark III Tully-Fisher Catalog versus the IRAS 1.2 Jy Survey. *ApJ*, 473, 22.

Davis, T. M. & Scrimgeour, M. I. (2014). Deriving accurate peculiar velocities (even at high redshift). *MNRAS*, 442, 1117–1122.

De Lucia, G. & Blaizot, J. (2007). The hierarchical formation of the brightest cluster galaxies. *MNRAS*, 375, 2–14.

Diaferio, A., Borgani, S., Moscardini, L., Murante, G., Dolag, K., Springel, V., Tormen, G., Tornatore, L., & Tozzi, P. (2005). Measuring cluster peculiar velocities with the Sunyaev-Zel'dovich effect: scaling relations and systematics. *MNRAS*, 356(4), 1477–1488.

Djorgovski, S. & Davis, M. (1987). Fundamental properties of elliptical galaxies. *ApJ*, 313, 59–68.

Dolag, K., Hansen, F. K., Roncarelli, M., & Moscardini, L. (2005). The imprints of local superclusters on the Sunyaev-Zel'dovich signals and their detectability with Planck. *MNRAS*, 363, 29–39.

Dolag, K., Komatsu, E., & Sunyaev, R. (2016). SZ effects in the Magneticum Pathfinder simulation: comparison with the Planck, SPT, and ACT results. *MNRAS*, 463, 1797–1811.

Dolag, K. & Sunyaev, R. (2013). Relative velocity of dark matter and baryons in clusters of galaxies and measurements of their peculiar velocities. *MNRAS*, 432(2), 1600–1615.

Dressler, A., Faber, S. M., Burstein, D., Davies, R. L., Lynden-Bell, D., Terlevich, R. J., & Wegner, G. (1987a). Spectroscopy and Photometry of Elliptical Galaxies: A Large-Scale Streaming Motion in the Local Universe. *ApJL*, 313, L37.

Dressler, A., Lynden-Bell, D., Burstein, D., Davies, R. L., Faber, S. M., Terlevich, R., & Wegner, G. (1987b). Spectroscopy and photometry of elliptical galaxies. I - A new distance estimator. *ApJ*, 313, 42–58.

Dupuy, A., Courtois, H. M., & Kubik, B. (2019). An estimation of the local growth rate from Cosmicflows peculiar velocities. *MNRAS*, 486(1), 440–448.

Eisenstein, D. J. & Hu, W. (1998). Baryonic Features in the Matter Transfer Function. *ApJ*, 496, 605–614.

Faber, S. M. & Jackson, R. E. (1976). Velocity dispersions and mass-to-light ratios for elliptical galaxies. *ApJ*, 204, 668–683.

Feldman, H., Juszkiewicz, R., Ferreira, P., Davis, M., Gaztañaga, E., Fry, J., Jaffe, A., Chambers, S., da Costa, L., Bernardi, M., Giovanelli, R., Haynes, M., & Wegner, G. (2003). An Estimate of $\Omega_m$ without Conventional Priors. *ApJL*, 596, L131–L134.

Feldman, H. A., Kaiser, N., & Peacock, J. A. (1994). Power-spectrum analysis of three-dimensional redshift surveys. *ApJ*, 426, 23–37.

Feldman, H. A. & Watkins, R. (2008). Bulk flow and shear moments of the SFI++ survey. *MNRAS*, 387, 825–829.

Feldman, H. A., Watkins, R., & Hudson, M. J. (2010). Cosmic flows on 100 $h^{-1}$ Mpc scales: standardized minimum variance bulk flow, shear and octupole moments. *MNRAS*, 407, 2328–2338.

Ferreira, P. G., Juszkiewicz, R., Feldman, H. A., Davis, M., & Jaffe, A. H. (1999). Streaming Velocities as a Dynamical Estimator of Ω. *ApJL*, 515, L1–L4.

Flender, S., Bleem, L., Finkel, H., Habib, S., Heitmann, K., & Holder, G. (2016). Simulations of the Pairwise Kinematic Sunyaev-Zel'dovich Signal. *ApJ*, 823(2), 98.

Flender, S., Nagai, D., & McDonald, M. (2017). Constraints on the Optical Depth of Galaxy Groups and Clusters. *ApJ*, 837(2), 124.

Gal, Y. & Ghahramani, Z. (2015). Dropout as a Bayesian approximation. *arXiv preprint arXiv:1506.02157*.

Gamow, G. (1946). Rotating Universe? *Nature*, 158(4016), 549.

Giovanelli, R., Haynes, M. P., Salzer, J. J., Wegner, G., da Costa, L. N., & Freudling, W. (1998). The Motions of Clusters of Galaxies and the Dipoles of the Peculiar Velocity Field. *AJ*, 116, 2632–2643.

Gorski, K. (1988). On the pattern of perturbations of the Hubble flow. *ApJL*, 332, L7–L11.

Gorski, K. M., Davis, M., Strauss, M. A., White, S. D. M., & Yahil, A. (1989). Cosmological velocity correlations - Observations and model predictions. *ApJ*, 344, 1–19.

Groth, E. J., Juszkiewicz, R., & Ostriker, J. P. (1989). An estimate of the velocity correlation tensor - Cosmological implications. *ApJ*, 346, 558–565.

Guo, Q., White, S., Angulo, R. E., Henriques, B., Lemson, G., Boylan-Kolchin, M., Thomas, P., & Short, C. (2013). Galaxy formation in WMAP1 and WMAP7 cosmologies. *MNRAS*, 428, 1351–1365.

Guzzo, L., Pierleoni, M., Meneux, B., Branchini, E., Le Fèvre, O., Marinoni, C., Garilli, B., Blaizot, J., De Lucia, G., Pollo, A., McCracken, H. J., & Bottini, D. (2008). A test of the nature of cosmic acceleration using galaxy redshift distortions. *Nature*, 451, 541–544.

Habib, S., Pope, A., Finkel, H., Frontiere, N., Heitmann, K., Daniel, D., Fasel, P., Morozov, V., Zagaris, G., & Peterka, T. (2016). HACC: Simulating sky surveys on state-of-the-art supercomputing architectures. *New Astronomy*, 42, 49–65.

Haehnelt, M. G. & Tegmark, M. (1996). Using the Kinematic Sunyaev-Zeldovich effect to determine the peculiar velocities of clusters of galaxies. *MNRAS*, 279, 545.

Hand, N., Addison, G. E., Aubourg, E., Battaglia, N., Battistelli, E. S., Bizyaev, D., Bond, J. R., Brewington, H., Brinkmann, J., Brown, B. R., Das, S., & Dawson, K. S. (2012). Evidence of Galaxy Cluster Motions with the Kinematic Sunyaev-Zel'dovich Effect. *Physical Review Letters*, 109(4), 041101.

Hand, N., Seljak, U., Beutler, F., & Vlah, Z. (2017). Extending the modeling of the anisotropic galaxy power spectrum to k = 0.4 hMpc$^{-1}$. *JCAP*, 10, 009.

He, S., Li, Y., Feng, Y., Ho, S., Ravanbakhsh, S., Chen, W., & Póczos, B. (2019). Learning to predict the cosmological structure formation. *Proceedings of the National Academy of Sciences*, (pp. 201821458).

Heitmann, K., Finkel, H., Pope, A., Morozov, V., Frontiere, N., Habib, S., Rangel, E., Uram, T., Korytov, D., & Child, H. (2019a). The Outer Rim Simulation: A Path to Many-Core Supercomputers. *arXiv e-prints*, (pp. arXiv:1904.11970).

Heitmann, K., Lawrence, E., Kwan, J., Habib, S., & Higdon, D. (2014). The Coyote Universe Extended: Precision Emulation of the Matter Power Spectrum. *ApJ*, 780, 111.

Heitmann, K., Uram, T. D., Finkel, H., Frontiere, N., Habib, S., Pope, A., Rangel, E., Hollowed, J., Korytov, D., & Larsen, P. (2019b). HACC Cosmological Simulations: First Data Release. *arXiv e-prints*, (pp. arXiv:1904.11966).

Heitmann, K., White, M., Wagner, C., Habib, S., & Higdon, D. (2010). The Coyote Universe. I. Precision Determination of the Nonlinear Matter Power Spectrum. *ApJ*, 715, 104–121.

Hellwing, W. A. (2014). Dynamics of pairwise motions in the Cosmic Web. *ArXiv e-prints*.

Hellwing, W. A., Barreira, A., Frenk, C. S., Li, B., & Cole, S. (2014). Clear and Measurable Signature of Modified Gravity in the Galaxy Velocity Field. *Physical Review Letters*, 112(22), 221102.

Hellwing, W. A., Nusser, A., Feix, M., & Bilicki, M. (2017). Not a Copernican observer: biased peculiar velocity statistics in the local Universe. *MNRAS*, 467, 2787–2796.

Hezaveh, Y. D., Perreault Levasseur, L., & Marshall, P. J. (2017). Fast automated analysis of strong gravitational lenses with convolutional neural networks. *Nature*, 548(7669), 555–557.

Hill, J. C., Ferraro, S., Battaglia, N., Liu, J., & Spergel, D. N. (2016). Kinematic Sunyaev-Zel'dovich Effect with Projected Fields: A Novel Probe of the Baryon Distribution with Planck, WMAP, and WISE Data. *Physical Review Letters*, 117(5), 051301.

Hoffman, Y., Nusser, A., Courtois, H. M., & Tully, R. B. (2016). Goodness-of-fit analysis of the Cosmicflows-2 database of velocities. *ArXiv e-prints*.

Holzapfel, W. L., Ade, P. A. R., Church, S. E., Mauskopf, P. D., Rephaeli, Y., Wilbanks, T. M., & Lange, A. E. (1997). Limits on the Peculiar Velocities of Two Distant Clusters Using the Kinematic Sunyaev-Zeldovich Effect. *ApJ*, 481(1), 35–48.

Howlett, C., Staveley-Smith, L., & Blake, C. (2017). Cosmological forecasts for combined and next-generation peculiar velocity surveys. *MNRAS*, 464, 2517–2544.

Hubble, E. (1929). A Relation between Distance and Radial Velocity among Extra-Galactic Nebulae. *Proceedings of the National Academy of Science*, 15(3), 168–173.

Hudson, M. J., Smith, R. J., Lucey, J. R., & Branchini, E. (2004). Streaming motions of galaxy clusters within 12 000 km s$^{-1}$- V. The peculiar velocity field. *MNRAS*, 352, 61–75.

Hudson, M. J., Smith, R. J., Lucey, J. R., Schlegel, D. J., & Davies, R. L. (1999). A Large-scale Bulk Flow of Galaxy Clusters. *ApJL*, 512, L79–L82.

Hurier, G. (2017). Constraining galaxy cluster velocity field with the tSZ-kSZ-kSZ bispectrum. *arXiv e-prints*.

Jaffe, A. H. & Kaiser, N. (1995). Likelihood Analysis of Large-Scale Flows. *ApJ*, 455, 26–+.

Johnson, A., Blake, C., Koda, J., Ma, Y.-Z., Colless, M., Crocce, M., Davis, T. M., Jones, H., Magoulas, C., Lucey, J. R., Mould, J., Scrimgeour, M. I., & Springob, C. M. (2014). The 6dF Galaxy Survey: cosmological constraints from the velocity power spectrum. *MNRAS*, 444, 3926–3947.

Juszkiewicz, R., Feldman, H. A., Fry, J. N., & Jaffe, A. H. (2010). Weakly nonlinear dynamics and the $\sigma_8$ parameter. *JCAP*, 2, 021.

Juszkiewicz, R., Ferreira, P. G., Feldman, H. A., Jaffe, A. H., & Davis, M. (2000). Evidence for a Low-Density Universe from the Relative Velocities of Galaxies. *Science*, 287, 109–112.

Juszkiewicz, R., Springel, V., & Durrer, R. (1999). Dynamics of Pairwise Motions. *ApJL*, 518(1), L25–L28.

Kaiser, N. (1987). Clustering in real space and in redshift space. *MNRAS*, 227, 1–21.

Kaiser, N. (1988). Theoretical implications of deviations from Hubble flow. *MNRAS*, 231, 149–167.

Kaiser, N. (1989). Local large scale structure VS cold dark matter. In M. Mezzetti, G. Giuricin, F. Mardirossian, & M. Ramella (Eds.), *Large Scale Structure and Motions in the Universe*, volume 151 of *Astrophysics and Space Science Library* (pp. 197–212).

Kashlinsky, A. & Atrio-Barandela, F. (2000). Measuring Cosmological Bulk Flows via the Kinematic Sunyaev-Zeldovich Effect in the Upcoming Cosmic Microwave Background Maps. *ApJL*, 536(2), L67–L71.

Kashlinsky, A., Atrio-Barandela, F., Kocevski, D., & Ebeling, H. (2008). A Measurement of Large-Scale Peculiar Velocities of Clusters of Galaxies: Results and Cosmological Implications. *ApJL*, 686(2), L49.

Kashlinsky, A., Atrio-Barandela, F., Kocevski, D., & Ebeling, H. (2009). A Measurement of Large-Scale Peculiar Velocities of Clusters of Galaxies: Technical Details. *ApJ*, 691, 1479–1493.

Kendall, A. & Gal, Y. (2017). What uncertainties do we need in Bayesian deep learning for computer vision? In *Advances in neural information processing systems* (pp. 5574–5584).

Kirillov, A. A. & Savelova, E. P. (2019). On distortion of the background radiation spectrum by wormholes: kinematic Sunyaev-Zel'dovich effect. *Ap& SS*, 364, 1.

Komatsu, E., Smith, K. M., Dunkley, J., Bennett, C. L., Gold, B., Hinshaw, G., Jarosik, N., Larson, D., Nolta, M. R., & Page, L. (2011). Seven-year Wilkinson Microwave Anisotropy Probe (WMAP) Observations: Cosmological Interpretation. *ApJ Supp*, 192, 18.

Kumar, A., Wang, Y., Feldman, H. A., & Watkins, R. (2015). Gravitational potential wells and the cosmic bulk flow. *ArXiv e-prints*.

Larson, D., Dunkley, J., Hinshaw, G., Komatsu, E., Nolta, M. R., Bennett, C. L., Gold, B., Halpern, M., Hill, R. S., & Jarosik (2011). Seven-year Wilkinson Microwave Anisotropy Probe (WMAP) Observations: Power Spectra and WMAP-derived Parameters. *ApJ Supp*, 192, 16.

Lauer, T. R. & Postman, M. (1994). The Motion of the Local Group with Respect to the 15,000 Kilometer per Second Abell Cluster Inertial Frame. *ApJ*, 425, 418.

Leavitt, H. S. (1908). 1777 variables in the Magellanic Clouds. *Annals of Harvard College Observatory*, 60, 87–108.3.

Leavitt, H. S. & Pickering, E. C. (1912). Periods of 25 Variable Stars in the Small Magellanic Cloud. *Harvard College Observatory Circular*, 173, 1–3.

Levasseur, L. P., Hezaveh, Y. D., & Wechsler, R. H. (2017). Uncertainties in parameters estimated with neural networks: Application to strong gravitational lensing. *arXiv preprint arXiv:1708.08843*.

Li, Y.-C., Ma, Y.-Z., Remazeilles, M., & Moodley, K. (2018). Measurement of the pairwise kinematic Sunyaev-Zeldovich effect with Planck and BOSS data. *Phys Rev D*, 97(2), 023514.

Linder, E. V. (2005). Cosmic growth history and expansion history. *Phys Rev D*, 72(4), 043529.

Lindner, R. R., Aguirre, P., Baker, A. J., Bond, J. R., Crichton, D., Devlin, M. J., & Essinger-Hileman (2015). The Atacama Cosmology Telescope: The LABOCA/ACT Survey of Clusters at All Redshifts. *ApJ*, 803(2), 79.

Macaulay, E., Feldman, H., Ferreira, P. G., Hudson, M. J., & Watkins, R. (2011). A slight excess of large-scale power from moments of the peculiar velocity field. *MNRAS*, 414, 621–626.

Macaulay, E., Feldman, H. A., Ferreira, P. G., Jaffe, A. H., Agarwal, S., Hudson, M. J., & Watkins, R. (2012). Power spectrum estimation from peculiar velocity catalogues. *MNRAS*, 425, 1709–1717.

Masters, K. L., Springob, C. M., Haynes, M. P., & Giovanelli, R. (2006). SFI++ I: A New I-Band Tully-Fisher Template, the Cluster Peculiar Velocity Dispersion, and $H_0$. *ApJ*, 653, 861–880.

Metcalf, R. B., Meneghetti, M., Avestruz, C., Bellagamba, F., Bom, C. R., Bertin, E., Cabanac, R., Courbin, F., & Davies, A. (2019). The strong gravitational lens finding challenge. *A&A*, 625, A119.

Mittal, A., de Bernardis, F., & Niemack, M. D. (2018). Optimizing measurements of cluster velocities and temperatures for CCAT-prime and future surveys. *JCAP*, 2, 032.

Morningstar, W. R., Hezaveh, Y. D., Levasseur, L. P., Blandford, R. D., Marshall, P. J., Putzky, P., & Wechsler, R. H. (2018). Analyzing interferometric observations of strong gravitational lenses with recurrent and convolutional neural networks. *arXiv preprint arXiv:1808.00011*.

Nusser, A. (2014). An Inconsistency in the Standard Maximum Likelihood Estimation of Bulk Flows. *ApJ*, 795, 3.

Nusser, A. (2016). On methods of estimating cosmological bulk flows. *MNRAS*, 455, 178–184.

Nusser, A., Branchini, E., & Davis, M. (2011). Bulk Flows from Galaxy Luminosities: Application to 2Mass Redshift Survey and Forecast for Next-generation Data Sets. *ApJ*, 735, 77–+.

Nusser, A. & Davis, M. (2011). The Cosmological Bulk Flow: Consistency with ΛCDM and z $\approx$ 0 Constraints on $\sigma_8$ and $\gamma$. *ApJ*, 736, 93.

Okumura, T., Hand, N., Seljak, U., Vlah, Z., & Desjacques, V. (2015). Galaxy power spectrum in redshift space: Combining perturbation theory with the halo model. *Phys Rev D*, 92(10), 103516.

Okumura, T., Seljak, U., Vlah, Z., & Desjacques, V. (2014). Peculiar velocities in redshift space: formalism, N-body simulations and perturbation theory. *JCAP*, 5, 003.

Peebles, P. J. E. (1980). *The large-scale structure of the universe*.

Petrillo, C. E., Tortora, C., Chatterjee, S., Vernardos, G., Koopmans, L. V. E., & Verdoes Kleijn, G. (2017). Finding strong gravitational lenses in the Kilo Degree Survey with Convolutional Neural Networks. *MNRAS*, 472(1), 1129–1150.

Planck Collaboration, Ade, P. A. R., Aghanim, N., Armitage-Caplan, C., Arnaud, M., Ashdown, M., Atrio-Barandela, F., Aumont, J., Baccigalupi, C., Banday, A. J., & et al. (2014a). Planck 2013 results. XVI. Cosmological parameters. *A&A*, 571, A16.

Planck Collaboration, Ade, P. A. R., Aghanim, N., Arnaud, M., Ashdown, M., Aubourg, E., Aumont, J., Baccigalupi, C., & Banday, A. J. (2016a). Planck intermediate results. XXXVII. Evidence of unbound gas from the kinetic Sunyaev-Zeldovich effect. *A&A*, 586, A140.

Planck Collaboration, Ade, P. A. R., Aghanim, N., Arnaud, M., Ashdown, M., Aubourg, E., Aumont, J., Baccigalupi, C., Banday, A. J., Barreiro, R. B., Bartolo, N., & Battaner, E. (2016b). Planck intermediate results. XXXVII. Evidence of unbound gas from the kinetic Sunyaev-Zeldovich effect. *A&A*, 586, A140.

Planck Collaboration, Ade, P. A. R., Aghanim, N., Arnaud, M., Ashdown, M., & Aumont, J. (2014b). Planck intermediate results. XIII. Constraints on peculiar velocities. *A&A*, 561, A97.

Planck Collaboration, Ade, P. A. R., Aghanim, N., Arnaud, M., Ashdown, M., Aumont, J., Baccigalupi, C., Balbi, A., & Banday, A. J. (2014c). Planck intermediate results. XIII. Constraints on peculiar velocities. *A&A*, 561, A97.

Planck Collaboration, Aghanim, N., Akrami, Y., Ashdown, M., Aumont, J., Baccigalupi, C., Ballardini, M., Banday, A. J., & Barreiro, R. B. (2018a). Planck intermediate results. LIII. Detection of velocity dispersion from the kinetic Sunyaev-Zeldovich effect. *A&A*, 617, A48.

Planck Collaboration, Aghanim, N., Akrami, Y., Ashdown, M., Aumont, J., Baccigalupi, C., Ballardini, M., Banday, A. J., & Barreiro, R. B. (2018b). Planck intermediate results. LIII. Detection of velocity dispersion from the kinetic Sunyaev-Zeldovich effect. *A&A*, 617, A48.

Planck Collaboration, Aghanim, N., Akrami, Y., Ashdown, M., Aumont, J., Baccigalupi, C., Ballardini, M., Banday, A. J., Barreiro, R. B., & Bartolo, N. (2018c). Planck 2018 results. VI. Cosmological parameters. *arXiv e-prints*, (pp. arXiv:1807.06209).

Ravanbakhsh, S., Lanusse, F., Mandelbaum, R., Schneider, J., & Poczos, B. (2016). Enabling Dark Energy Science with Deep Generative Models of Galaxy Images. *arXiv e-prints*, (pp. arXiv:1609.05796).

Reid, B. A. & White, M. (2011). Towards an accurate model of the redshift-space clustering of haloes in the quasi-linear regime. *MNRAS*, 417, 1913–1927.

Rephaeli, Y. & Lahav, O. (1991). Peculiar cluster velocities from measurements of the kinematic Sunyaev-Zeldovich effect. *ApJ*, 372, 21–24.

Rest, A., Scolnic, D., Foley, R. J., Huber, M. E., Chornock, R., Narayan, G., Tonry, J. L., Berger, E., Soderberg, A. M., & Stubbs, C. W. (2014). Cosmological Constraints from Measurements of Type Ia Supernovae Discovered during the First 1.5 yr of the Pan-STARRS1 Survey. *ApJ*, 795(1), 44.

Riess, A. G., Macri, L. M., Hoffmann, S. L., Scolnic, D., Casertano, S., Filippenko, A. V., Tucker, B. E., Reid, M. J., Jones, D. O., Silverman, J. M., Chornock, R., Challis, P., Yuan, W., Brown, P. J., & Foley, R. J. (2016). A 2.4% Determination of the Local Value of the Hubble Constant. *ApJ*, 826, 56.

Rubin, V. C. (1951). Differential rotation of the inner metagalaxy. *AJ*, 56, 47.

Rubin, V. C., Ford, W. K., J., Thonnard, N., Roberts, M. S., & Graham, J. A. (1976a). Motion of the Galaxy and the Local Group determined from the velocity anisotropy of distant Sc I galaxies. I. The data. *AJ*, 81, 687–718.

Rubin, V. C., Thonnard, N., Ford, W. K., J., & Roberts, M. S. (1976b). Motion of the Galaxy and the Local Group determined from the velocity anisotropy of distant Sc I galaxies. II. The analysis for the motion. *AJ*, 81, 719–737.

Sayers, J., Montaña, A., Mroczkowski, T., Wilson, G. W., Zemcov, M., & Zitrin, A. (2019). Imaging the Thermal and Kinematic Sunyaev-Zel'dovich Effect Signals in a Sample of 10 Massive Galaxy Clusters: Constraints on Internal Velocity Structures and Bulk Velocities. *ApJ*, 880(1), 45.

Sayers, J., Zemcov, M., Glenn, J., Golwala, S. R., Maloney, P. R., Siegel, S. R., Wheeler, J., Bockstiegel, C., Brugger, S., & Czakon, N. G. (2016). Peculiar Velocity Constraints from Five-band SZ Effect Measurements toward RX J1347.5-1145 with MUSIC and Bolocam from the CSO. *ApJ*, 820, 101.

Schaan, E., Ferraro, S., Vargas-Magaña, M., Smith, K. M., Ho, S., Aiola, S., Battaglia, N., Bond, J. R., & De Bernardis, F. (2016). Evidence for the kinematic Sunyaev-Zel'dovich effect with the Atacama Cosmology Telescope and velocity reconstruction from the Baryon Oscillation Spectroscopic Survey. *Phys Rev D*, 93(8), 082002.

Schechter, P. L. (1980). Mass-to-light ratios for elliptical galaxies. *AJ*, 85, 801–811.

Scoccimarro, R. (2004). Redshift-space distortions, pairwise velocities, and nonlinearities. *Phys Rev D*, 70(8), 083007.

Scrimgeour, M. I., Davis, T. M., Blake, C., Staveley-Smith, L., Magoulas, C., Springob, C. M., Beutler, F., Colless, M., Johnson, A., Jones, D. H., Koda, J., Lucey, J. R., Ma, Y.-Z., Mould, J., & Poole, G. B. (2016a). The 6dF Galaxy Survey: bulk flows on 50-70 $h^{-1}$ Mpc scales. *MNRAS*, 455, 386–401.

Scrimgeour, M. I., Davis, T. M., Blake, C., Staveley-Smith, L., Magoulas, C., Springob, C. M., Beutler, F., Colless, M., Johnson, A., Jones, D. H., Koda, J., Lucey, J. R., Ma, Y.-Z., Mould, J., & Poole, G. B. (2016b). The 6dF Galaxy Survey: bulk flows on 50-70 $h^{-1}$ Mpc scales. *MNRAS*, 455, 386–401.

Seiler, J. & Parkinson, D. (2016). Using measurements of the cosmic bulk flow to constrain f(R) Gravity. *MNRAS*, 462, 75–80.

Seljak, U. & McDonald, P. (2011). Distribution function approach to redshift space distortions. *JCAP*, 11, 039.

Senatore, L. & Zaldarriaga, M. (2014). Redshift Space Distortions in the Effective Field Theory of Large Scale Structures. *ArXiv e-prints*.

Smoot, G. F., Gorenstein, M. V., & Muller, R. A. (1977). Detection of Anisotropy in the Cosmic Blackbody Radiation. *Phys Rev Lett*, 39(14), 898–901.

Soergel, B., Flender, S., Story, K. T., Bleem, L., Giannantonio, T., Efstathiou, G., Rykoff, E., Benson, B. A., Crawford, T., Dodelson, S., Habib, S., Heitmann, K., & Holder, G. (2016). Detection of the kinematic Sunyaev-Zel'dovich effect with DES Year 1 and SPT. *MNRAS*, 461, 3172–3193.

Soergel, B., Saro, A., Giannantonio, T., Efstathiou, G., & Dolag, K. (2017). Cosmology with the pairwise kinematic SZ effect: Calibration and validation using hydrodynamical simulations. *ArXiv e-prints*.

Song, Y.-S., Nishimichi, T., Taruya, A., & Kayo, I. (2013). Chasing unbiased spectra of the Universe. *Phys Rev D*, 87(12), 123510.

Springel, V. (2005). The cosmological simulation code GADGET-2. *MNRAS*, 364, 1105–1134.

Springel, V., White, S. D. M., Jenkins, A., Frenk, C. S., Yoshida, N., Gao, L., Navarro, J., Thacker, R., Croton, D., Helly, J., Peacock, J. A., Cole, S., Thomas, P., Couchman, H., Evrard, A., Colberg, J., & Pearce, F. (2005). Simulations of the formation, evolution and clustering of galaxies and quasars. *Nature*, 435, 629–636.

Springel, V., Yoshida, N., & White, S. D. M. (2001). GADGET: a code for collisionless and gasdynamical cosmological simulations. *New Astronomy*, 6, 79–117.

Springob, C. M., Magoulas, C., Colless, M., Mould, J., Erdoğdu, P., Jones, D. H., Lucey, J. R., Campbell, L., & Fluke, C. J. (2014a). The 6dF Galaxy Survey: peculiar velocity field and cosmography. *MNRAS*, 445, 2677–2697.

Springob, C. M., Magoulas, C., Colless, M., Mould, J., Erdoğdu, P., Jones, D. H., Lucey, J. R., Campbell, L., & Fluke, C. J. (2014b). The 6dF Galaxy Survey: peculiar velocity field and cosmography. *MNRAS*, 445, 2677–2697.

Springob, C. M., Masters, K. L., Haynes, M. P., Giovanelli, R., & Marinoni, C. (2007). SFI++. II. A New I-Band Tully-Fisher Catalog, Derivation of Peculiar Velocities, and Data Set Properties. *ApJ Supp*, 172, 599–614.

Springob, C. M., Masters, K. L., Haynes, M. P., Giovanelli, R., & Marinoni, C. (2009). Erratum: ”SFI++ II: A New I-Band Tully-Fisher Catalog, Derivation of Peculiar Velocities and Data Set Properties” <A href=”bib_query?2007ApJS..172..599S”> (2007, ApJS, 172, 599)</A>. *ApJ Supp*, 182, 474–475.

Sugiyama, N. S., Okumura, T., & Spergel, D. N. (2018). A direct measure of free electron gas via the kinematic Sunyaev-Zel'dovich effect in Fourier-space analysis. *MNRAS*, 475, 3764–3785.

Sunyaev, R. A. & Zeldovich, I. B. (1980). The velocity of clusters of galaxies relative to the microwave background - The possibility of its measurement. *MNRAS*, 190, 413–420.

Sunyaev, R. A. & Zeldovich, Y. B. (1970). Small-Scale Fluctuations of Relic Radiation. *Ap& SS*, 7, 3–19.

Sunyaev, R. A. & Zeldovich, Y. B. (1972). The Observations of Relic Radiation as a Test of the Nature of X-Ray Radiation from the Clusters of Galaxies. *Comments on Astrophysics and Space Physics*, 4, 173.

Taruya, A., Nishimichi, T., & Bernardeau, F. (2013). Precision modeling of redshift-space distortions from a multipoint propagator expansion. *Phys Rev D*, 87(8), 083509.

Taruya, A., Nishimichi, T., & Saito, S. (2010). Baryon acoustic oscillations in 2D: Modeling redshift-space power spectrum from perturbation theory. *Phys Rev D*, 82(6), 063522.

Thomas, B. C., Melott, A. L., Feldman, H. A., & Shandarin, S. F. (2004). Quantifying the bull's-eye effect. *The Astrophysical Journal*, 601(1), 28–36.

Tonry, J. & Schneider, D. P. (1988). A New Technique for Measuring Extragalactic Distances. *AJ*, 96, 807.

Tonry, J. L. & Davis, M. (1981). Velocity dispersions of elliptical and S0 galaxies. I - Data and mass-to-light ratios. II - Infall of the local group to Virgo. *ApJ*, 246, 666–695.

Tonry, J. L., Dressler, A., Blakeslee, J. P., Ajhar, E. A., Fletcher, A. B., Luppino, G. A., Metzger, M. R., & Moore, C. B. (2001). The SBF Survey of Galaxy Distances. IV. SBF Magnitudes, Colors, and Distances. *ApJ*, 546, 681–693.

Tonry, J. L., Schmidt, B. P., Barris, B., Candia, P., Challis, P., Clocchiatti, A., Coil, A. L., Filippenko, A. V., Garnavich, P., Hogan, C., Holland, S. T., Jha, S., Kirshner, R. P., Krisciunas, K., Leibundgut, B., Li, W., & Matheson, T. (2003). Cosmological Results from High-z Supernovae. *ApJ*, 594, 1–24.

Tully, R. B., Courtois, H. M., Dolphin, A. E., Fisher, J. R., Héraudeau, P., Jacobs, B. A., Karachentsev, I. D., Makarov, D., Makarova, L., Mitronova, S., Rizzi, L., Shaya, E. J., Sorce, J. G., & Wu, P.-F. (2013). Cosmicflows-2: The Data. *AJ*, 146, 86.

Tully, R. B., Courtois, H. M., & Sorce, J. G. (2016). Cosmicflows-3. *AJ*, 152, 50.

Tully, R. B. & Fisher, J. R. (1977). A new method of determining distances to galaxies. *A&A*, 54, 661–673.

Turnbull, S. J., Hudson, M. J., Feldman, H. A., Hicken, M., Kirshner, R. P., & Watkins, R. (2012). Cosmic flows in the nearby universe from Type Ia supernovae. *MNRAS*, 420, 447–454.

Uhlemann, C. & Kopp, M. (2015). Coarse-grained cosmological perturbation theory: Stirring up the dust model. *Phys Rev D*, 91(8), 084010.

Vlah, Z., Castorina, E., & White, M. (2016). The Gaussian streaming model and convolution Lagrangian effective field theory. *JCAP*, 12, 007.

Wang, Y., Rooney, C., Feldman, H. A., & Watkins, R. (2018). The peculiar velocity correlation function. *MNRAS*, 480, 5332–5341.

Watkins, R. & Feldman, H. A. (2007). Power spectrum shape from peculiar velocity data. *MNRAS*, 379, 343–348.

Watkins, R. & Feldman, H. A. (2015a). An unbiased estimator of peculiar velocity with Gaussian distributed errors for precision cosmology. *MNRAS*, 450, 1868–1873.

Watkins, R. & Feldman, H. A. (2015b). Large-scale bulk flows from the Cosmicflows-2 catalogue. *MNRAS*, 447, 132–139.

Watkins, R., Feldman, H. A., & Hudson, M. J. (2009). Consistently large cosmic flows on scales of $100\mathrm{h}^{-1}$Mpc: a challenge for the standard ΛCDM cosmology. *MNRAS*, 392, 743–756.

Wegner, G., Bernardi, M., Willmer, C. N. A., da Costa, L. N., Alonso, M. V., Pellegrini, P. S., Maia, M. A. G., Chaves, O. L., & Rité, C. (2003). Redshift-Distance Survey of Early-Type Galaxies: Spectroscopic Data. *AJ*, 126, 2268–2280.

Willick, J. A. (1999). The Las Campanas/Palomar 10,000 Kilometer Per Second Cluster Survey. I. Properties of the Tully-Fisher Relation. *ApJ*, 516, 47–61.

Willick, J. A., Strauss, M. A., Dekel, A., & Kolatt, T. (1997). Maximum Likelihood Comparisons of Tully-Fisher and Redshift Data: Constraints on Ω and Biasing. *ApJ*, 486, 629–664.

Wishart, J. (1928). The generalised product moment distribution in samples from a normal multivariate population. *Biometrika*, 20A(1/2), 32–52.

Zaroubi, S., Zehavi, I., Dekel, A., Hoffman, Y., & Kolatt, T. (1997). Large-Scale Power Spectrum from Peculiar Velocities via Likelihood Analysis. *ApJ*, 486, 21–31.

Zhang, P., Feldman, H. A., Juszkiewicz, R., & Stebbins, A. (2008). A new method of measuring the cluster peculiar velocity power spectrum. *MNRAS*, 388, 884–888.

Zhang, P., Pan, J., & Zheng, Y. (2013). Peculiar velocity decomposition, redshift space distortion, and velocity reconstruction in redshift surveys: The methodology. *Phys Rev D*, 87(6), 063526.

Zheng, Y., Zhang, P., Jing, Y., Lin, W., & Pan, J. (2013). Peculiar velocity decomposition, redshift space distortion, and velocity reconstruction in redshift surveys. II. Dark matter velocity statistics. *Phys Rev D*, 88(10), 103510.